Incorporating space charge in the transverse phase-space matching and tomography at PITZ

Dissertation
zur Erlangung des Doktorgrades
des Fachbereichs Physik
der Universität Hamburg

vorgelegt von
Georgios Kourkafas

Hamburg
2015

Gutachter der Dissertation:	Prof. Dr. Jörg Roßbach Dr. Winfried Decking
Datum der Disputation:	13.10.2015
Vorsitzende der Prüfungskommission:	Prof. Dr. Daniela Pfannkuche
Vorsitzender des Fach-Promotionsausschusses Physik:	Prof. Dr. Jan Louis
Leiter des Fachbereichs Physik:	Prof. Dr. Peter Hauschildt
Dekan der Fakultät für Mathematik, Informatik und Naturwissenschaften:	Prof. Dr. Heinrich Graener

Abstract

The ever-expanding achievements in the field of particle accelerators push their specifications to very demanding levels. The performance of many modern applications depends on their ability to be operated with high bunch charges confined in small volumes. However, the consequence of increased intensity is strong space-charge forces, which perplex the beam manipulation and undermine the beam quality. As a result, reliable methods are needed to control and measure the accelerated particles under these extraordinary conditions.

The phase space tomography is a diagnostic technique which can reveal details of the transverse beam parameters for a wide range of intensities and energies, with minimal influence from the machine instabilities, in a quasi non-destructive way. The accuracy of this method relies on the precise knowledge and control of the particle dynamics under the influence of space charge in the different stages of the measurement.

On the one hand, the matching of the beam to the measurement's design transverse parameters requires a procedure which efficiently compensates the effects of space charge. Depending on the structure of the magnetic lattice, different aspects of these effects prevail, therefore different strategies have to be developed. On the other hand, the impact of the space-charge forces on the phase-space transformations during the data acquisition has to be included in the model which is used for the tomographic reconstruction.

The aim of this thesis is to provide and test time-efficient solutions for the incorporation of space charge in the transverse beam matching and phase space tomography.

Zusammenfassung

Die ständigen Weiterentwicklungen in der Beschleunigerphysik verlangen Leistungsfähigkeit auf höchstem Niveau. Die Performance vieler moderner Beschleuniger hängt von ihrer Fähigkeit ab, möglichst viele Teilchen in einem möglichst kleinen Volumen zu binden. Große Stromdichten rufen jedoch starke Raumladungskräfte hervor, welche sowohl Strahlqualität als auch Strahlführung negativ beeinflussen. Aufgrund dessen benötigt man verlässliche Methoden um beschleunigte Teilchen unter diesen extremen Bedingungen kontrollieren und messen zu können.

Die Phasenraum Tomographie ist eine Diagnosetechnik, die Details der transversalen Strahlparameter für einen großen Intensitäts- und Energiebereich, mit minimalem Einfluss der Maschineninstabilitäten und in quasi nicht-destruktiver Weise messbar macht. Die Genauigkeit dieser Messmethode hängt von einer guten Kenntnis und Kontrolle der zugrunde liegenden Strahldynamik, inklusive der Einflüsse von Raumladung, in den verschiedenen Abschnitten des Messaufbaus ab.

Einerseits benötigt das Angleichen des Strahls an die transversalen Designparameter eine Prozedur, welche effizient Raumladungseffekte kompensiert. Hierbei dominieren, abhängig von der magnetischen Struktur, unterschiedliche Aspekte von Raumladungseffekten, für die entsprechende Strategien entwickelt werden müssen. Andererseits muss der Einfluss der Raumladungskräfte auf die Phasenraumtransformationen während der Datennahme im Modell für die tomographische Rekonstruktion berücksichtigt werden.

Ziel dieser Arbeit ist es effiziente Lösungen für die Implementierung von Raumladung in das transversale Angleichen der Strahlparameter und die Phasenraum Tomographie zu entwickeln und zu testen.

OXI

Contents

Chapter 1

Introduction

In the last 100 years particle accelerators have evolved into powerful tools with increasing significance for a wide range of applications: scientific research, medical diagnosis and treatment, industrial production and monitoring, sterilization and food processing, future nuclear energy and military. In order to meet the desired specifications for each case (properties of the accelerated particles, machine performance, cost, etc.), diverse designs have been conceived and implemented, mainly divided between circular (rings) and linear machines (linacs). When focusing on the quality of the produced particles, linacs are especially effective in delivering high intensity beams of precise energy in small volumes in space. A leading application of this type is the Free-Electron Laser (FEL), which is able to generate very intense, energetic and coherent radiation of tunable wavelengths, ranging from the Terahertz to the X-ray scale, and pulse duration down to the femtosecond regime [1,2]. The Photo Injector Test facility at DESY, Zeuthen site (PITZ), carries out a research and development program which concentrates on testing, characterizing and optimizing particle sources for FELs, in particular for the FLASH [1] and European XFEL [3] facilities in Hamburg, Germany.

In order to maximise their peak performance, many of the modern accelerators operate with high bunch charges confined in short pulses, reaching very high peak currents. Moreover, the particle bunches in linacs can be further compressed, increasing their peak current to the range of few kA (Fig. 1.1 presents the expected values for the European XFEL). The downside of this high intensity, especially at lower energies and compressed beam dimensions, is the increased Coulomb repulsion among the particles of the beam, which is known as the *space-charge* force. This side effect creates two

major difficulties:

1. transporting the particle beam in a controlled way while preserving its quality at the same time and

2. measuring important beam parameters with reliable accuracy.

This thesis aims to address the effect of space charge in both of the above points, focusing on the Phase Space Tomography (PST) as a measurement method.

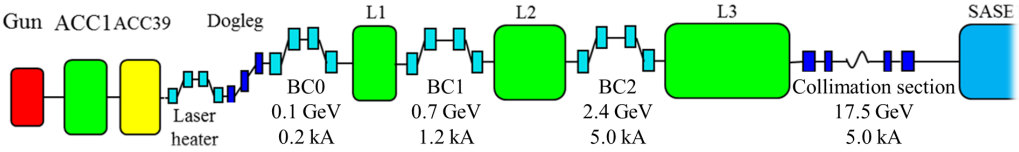

Figure 1.1: Schematic layout of the European XFEL electron beamline up to the first undulator entrance (SASE) with an indication of the expected beam energy and peak current after each bunch compressor (BC). The rounded rectangles represent the accelerating modules, starting from the photo-injector (Gun) with a peak current of 50 A at the energy of 6 MeV. More information in [4].

Concerning the beam transport, the operation of most linear and circular machines requires specific parameters to be delivered at certain locations of the beamline. Furthermore, various applications, diagnostics and experiments impose additional constrains on the beam specifications. In order to achieve these requirements, focusing elements with adjustable strengths are employed along the beamline in a procedure called *beam matching*. An accurate prediction of the necessary focusing strengths by simulation packages is possible only when the effect of space charge is properly considered in the used beam dynamics models, especially for high beam currents and relatively low energies.

While the matching of space-charge influenced beams in many facilities is progressively achieved by iterative trials during operation, a more effective strategy is desired. PITZ, being a test facility, has no standard operation mode; on the contrary, it constantly changes its parameters in order to optimize and characterize the produced beams. Moreover, different matching constraints are imposed along the beamline, depending on

the components which are needed at each moment: beside the tomography module, the forthcoming Transverse Deflecting Cavity (TDS) [5], the Plasma Wakefield Acceleration (PWA) experiment [6] and the potential infrared/terahertz (IR/THz) source [7], all have their own beam requirements. Similarly, FLASH and the European XFEL are also foreseen to benefit from such a development when changing their mode of operation.

This study suggests that the strategy on how to achieve a space-charge matching in the most time-effective way depends on the structure of the focusing elements:

- periodic and dense lattices, where a controlled periodic transport can be achieved
- aperiodic and/or sparse lattices, where the beam transport will undergo significant deviations

At PITZ as well as at FLASH and the European XFEL, both lattice types are met: the sections for transverse beam diagnostics using multiple profile monitors belong to the first category and the matching sections of various beamline components belong to the second one. For the first type, easier and faster solutions can be implemented, while for the second, more complex techniques are necessary.

Following the beam transport and matching, the measurement of the beam quality is vital for the machine operation and performance. For many types of accelerators, a figure of merit for the quality of the beam is its *emittance* value or, even more completely, its *phase space* portrait. These properties represent the spatial coherence of the beam or else its ability to be focused. This aspect is of particular interest for the FELs, since it affects the gain of the lasing process, the brightness or brilliance of the produced radiation, its minimum achievable wavelength and transverse coherence [8,9].

One of the known techniques to measure the transverse phase space of a particle beam is by means of tomographic reconstruction. In addition to PITZ [10], FLASH [11] and potentially the European XFEL, this approach has been used in a number of machines and facilities, including ALICE [12], Jefferson Lab FEL [13], UMER [14], Cornel ERL [15], TRIUMF [16], SNS and PSI [17] and BNL [18]. Comparing to the measurement methods which use intercepting apertures, tomography is able to tolerate much higher beam energies without facing mechanical limitations. Furthermore, tomography is less prone to the short-term machine instabilities, allowing single bunch

measurements even at low bunch charges due to its high signal-to-noise ratio, the fast data acquisition and the simultaneous measurement of the two transverse planes. When combined with additional kicker magnets (as foreseen at PITZ), its functionality can be extended to a permanent, quasi non-destructive, monitoring tool not only for the beam quality, but also for the long-term stability and reliability of the machine, factors that are currently among the top priorities for the operation of FELs and other applications. However, the above capabilities would be restricted only to beams with negligible space-charge influence, when the beam dynamics model used in the tomographic reconstruction does not take into account the self fields. Especially for compressed beams of lower energies, the neglect of the space-charge forces will result in significant measurement errors.

In summary, the main points of this thesis concern the incorporation of space charge in the beam matching and the phase space tomography. At first, the effect of space charge is incorporated in the tomographic reconstruction with an analysis which can be extended, under conditions, to the multi-screen measurement and the quadrupole-scan method. Afterwards, a fast matching solution is suggested for regular focusing lattices along which the beam emittance stays fairly constant, by including the effect of the linear self fields into non-space-charge matching codes. Finally, a different approach is followed for long and irregular sections where the emittance fluctuates, using a software which quickly simulates the linear space-charge forces along the bunch.

The thesis is structured in seven chapters. Following this introduction, the second chapter presents the fundamental physics of non-space-charge beam dynamics, which are involved in the beam matching and the measurement of the transverse emittance, together with the principles of phase space tomography. The third chapter describes the layout of the PITZ facility, with a focus on the matching- and tomography-related components, and explains the process of the tomographic reconstruction. In the fourth chapter, the effect of space charge along the PST section is evaluated with simulations and incorporated in the tomographic reconstruction of experimental data. In the fifth chapter, a method is presented for a fast space-charge matching of the PST lattice. The sixth chapter extends the space-charge analysis for the matching section, presenting measurements of the emittance variations and simulations of a more analytic matching approach. In the seventh chapter the achievements, difficulties and conclusions of the thesis are listed, together with an outlook for the future.

Chapter 2

Transverse dynamics and phase space tomography without space charge

This chapter summarizes the fundamental physics background of the transverse beam dynamics under external magnetic fields. The concepts of the transverse phase space and emittance are explained and basic aspects of the beam transport and matching are presented together with the relevant magnetic elements. Finally, the principles, implementations and features of the phase space tomography are introduced.

2.1 Transverse beam dynamics

2.1.1 Single-particle dynamics

The fundamental function of a particle accelerator is to transfer energy to the particles through electric fields. Due to their low rest mass m_0, the particles quickly approach velocities close to the speed of light in vacuum (c) and become relativistic. The total energy of a relativistic particle E_T is given by

$$E_T = mc^2 = T + m_0c^2 = \sqrt{p^2c^2 + m_0^2c^4}\,, \tag{2.1}$$

where m is the relativistic mass of the particle, T its kinetic energy and p its momentum. The ratio of the total to the rest energy is expressed by the

Lorentz factor γ_{rel}, while the ratio of the particle's velocity to the speed of light by β_{rel}:

$$\gamma_{rel} = \frac{E_T}{m_0 c^2}\,, \tag{2.2}$$

$$\beta_{rel} = \frac{v}{c}\,. \tag{2.3}$$

The two relativistic factors are connected with the following relation:

$$\gamma_{rel} = \frac{1}{\sqrt{1-\beta_{rel}^2}} \tag{2.4}$$

and their product equals to the normalized momentum:

$$\beta_{rel}\gamma_{rel} = \frac{p}{m_0 c}\,. \tag{2.5}$$

In beam dynamics, the state of a particle is usually described in the *phase space* $(x, p_x, y, p_y, z, \delta p_z)$, where the particle's displacement from the reference trajectory is shown with respect to its respective momentum value in the three dimensional (3-D) space, with δp_z expressing the deviation of the longitudinal momentum from the reference value. The phase-space plot or portrait indicates all the possible states a particle can obtain. Alternatively the *trace space* $(x, x', y, y', z, \delta p_z/p_z)$ can be used, by normalizing each momentum contribution with the longitudinal momentum:

$$q' = \frac{p_q}{p_z}\,, \tag{2.6}$$

for q=$\{x, y\}$. Quite often in literature — in this thesis as well — the term phase space is used for both cases. From now on, the prime symbol ($'$) shall indicate the first derivative over z, which is going to be considered the axis of the beam propagation.

A particle with charge Q propagating in an accelerator with a velocity vector $\mathbf{v}$ is subject to electric ($\mathbf{E}$) and magnetic ($\mathbf{B}$) fields, which together cause the Lorentz force $\mathbf{F}$:

$$\mathbf{F} = Q\left(\mathbf{E} + \mathbf{v} \times \mathbf{B}\right)\,, \tag{2.7}$$

where bold letters indicate vectors instead of scalar values. The electric fields are usually used to accelerate the beam, while the magnetic ones to guide and focus the beam. This study focuses on straight transport lines where

no acceleration takes places ($\gamma'_{rel} = 0$) and the reference particle trajectory does not bend (no dipole fields are used). Therefore, when referring to external fields, only transverse focusing and defocusing fields are going to be considered, with their strength being, in addition, linear with respect to the particle's displacement from the axis of propagation. The forces driven from such fields have the form of $F_q = Qv_zGq = \kappa_0 p(\beta_{rel}c)q$ in the direction of q=$\{x, y\}$, where G and κ_0 represent the external *focusing gradient* and *focusing strength* respectively. When such forces act on a particle, its equation of motion in the transverse plane is given by:

$$q'' + \kappa_0 q = 0\,, \tag{2.8}$$

which is a reduced version of the *paraxial ray equation*, the basic first-order equation which describes the motion of charged particles when their trajectories remain close to the axis of propagation without showing big gradients and the transverse momentum is considerably small compared to the longitudinal one [19].

For a constant focusing strength κ_0, Eq. 2.8 represent a simple harmonic oscillator of the form $q(z) = A_q sin\left(\sqrt{\kappa_0}z + \phi_{q0}\right)$ for q=$\{x, y\}$, where A_q and ϕ_{q0} depend only on the initial state of the particle. In the trace space (q, q'), the particle revolves around an ellipse of fixed dimensions and orientation at a constant frequency $\sqrt{\kappa_0}$. In the general case where the focusing force is not constant ($\kappa_0(z)$), Eq. 2.8 constitutes a Mathieu-Hill equation which can be solved using the Floquet functions [19]. The result is a quasi-harmonic oscillation, which is known as *betatron oscillation* and has the form:

$$q(z) = \sqrt{J_q\beta_q(z)}sin\left(\phi_q(z) + \phi_{q0}\right)\,, \tag{2.9}$$

where J_q and ϕ_{q0} depend only on the initial state of the particle and β_q and ϕ_q depend on z. J_q is referred to as the *action variable* or *single particle emittance*, β_q as the *betatron function* and ϕ_{q0} as the *(betatron) phase advance* of the particle, which is given by:

$$\phi_q = \int_{z_i}^{z_f} \frac{\mathrm{d}z}{\beta_q(z)}\,, \tag{2.10}$$

between two points z_i, z_f in the beamline. The plot of Eq. 2.9 in the trace space forms an ellipse as well, with the difference that its dimensions and orientation change along z, as schematically plotted in Fig 2.1. The phase advance determines the position of the particle on its trace-space ellipse.

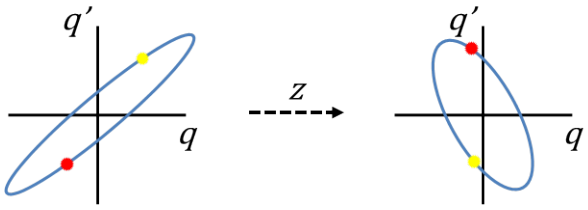

Figure 2.1: A particle is shown on its trace-space ellipse (q=$\{x, y\}$) for different initial ϕ_{0q} phases (red and yellow colour) at different locations along the beam line (left and right plot).

In order to express the properties of this ellipse at a given position, the *Courant-Snyder* (C-S) or *Twiss* parameters, denoted as β_q, α_q and γ_q, are used [20]. The C-S parameters are connected with each other through the following relations:

$$\alpha_q = -\frac{\beta_q'}{2}\,, \tag{2.11}$$

$$\gamma_q = \frac{1+\alpha_q^2}{\beta_q}\,, \tag{2.12}$$

for q=$\{x, y\}$. The orientation of the trace-space ellipse with respect to the spatial axis is then given by the angle θ_q:

$$\theta_q = \frac{\arctan\left(\dfrac{2\alpha_q}{\gamma_q - \beta_q}\right)}{2} \tag{2.13}$$

and the dimensions of the ellipse by the C-S parameters as shown in Fig. 2.2.

A very important property of the trace-space ellipse is that its area stays constant as the particle propagates, despite the transformations it undergoes. The area of the ellipse is equal to $J_q\pi$, which makes J_q an invariant of the particle's motion, which at every position along z is equal to:

$$\gamma_q q^2 + 2\alpha_q q q' + \beta_q q'^2 = J_q\,. \tag{2.14}$$

This property is closely connected with the Liouville's theorem which concerns the multi-particle dynamics and is going to be introduced later in this chapter.

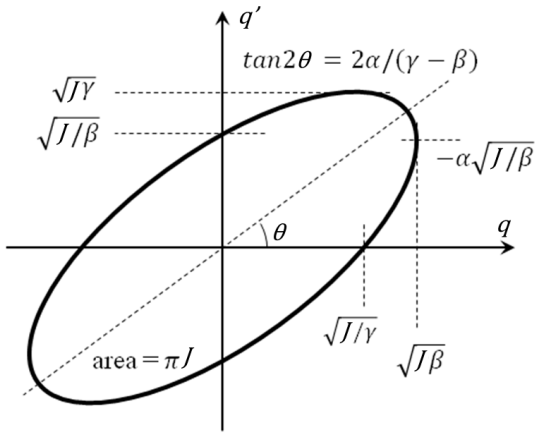

Figure 2.2: The trace-space ellipse characterized by the C-S parameters (q=$\{x, y\}$).

The propagation of the trace-space coordinates between two positions along a beamline can be expressed using a *transfer matrix* M [19]:

$$\begin{pmatrix} q \\ q' \end{pmatrix}_z = M \begin{pmatrix} q \\ q' \end{pmatrix}_0 = \begin{pmatrix} M_{11} & M_{12} \\ M_{21} & M_{22} \end{pmatrix} \begin{pmatrix} q \\ q' \end{pmatrix}_0 , \tag{2.15}$$

where the subscript 0 represents the initial point and z the final point and the dimensions of M is 2×2 when referring to a single transverse plane. More generally, both transverse phase planes can be included by using a 4×4 M matrix, or even the full 6-D trace space coordinates with a 6×6 matrix. Since the external focusing is usually not constant but varies along the beam propagation ($\kappa_0(z)$), it is convenient to split the beamline in parts of constant focusing. The form of M along these parts is well-documented for the common beamline elements [21] and more specifically:

- for a drift space (lattice of no transverse focusing) of length L

$$M = \begin{pmatrix} 1 & L \\ 0 & 1 \end{pmatrix} , \tag{2.16}$$

- for a constant focusing channel of length l

$$M = \begin{pmatrix} cos\left(\sqrt{\kappa_0} l\right) & \frac{1}{\sqrt{\kappa_0}} sin\left(\sqrt{\kappa_0} l\right) \\ -\sqrt{\kappa_0} sin\left(\sqrt{\kappa_0} l\right) & cos\left(\sqrt{\kappa_0} l\right) \end{pmatrix} \tag{2.17}$$

- and for a constant defocusing channel of length l

$$M = \begin{pmatrix} cosh\left(\sqrt{|\kappa_0|}l\right) & \frac{1}{\sqrt{|\kappa_0|}} sinh\left(\sqrt{|\kappa_0|}l\right) \\ \sqrt{|\kappa_0|} sinh\left(\sqrt{|\kappa_0|}l\right) & cosh\left(\sqrt{|\kappa_0|}l\right) \end{pmatrix} . \tag{2.18}$$

When the transfer matrices of neighbouring beamline parts are known (from M_i downstream to M_f), a single transfer matrix can be derived which represents the response of the overall lattice. The total matrix M_T is calculated by multiplying the transfer matrices of the consecutive segments in reverse order:

$$M_T = M_f M_{f-1} \dots M_{i+1} M_i \, . \tag{2.19}$$

As seen in Eq. 2.15, the effect of a transfer matrix corresponds to a linear transformation of the particle's trace-space coordinates, which leads to a shearing of the trace-space ellipse, as for example in Fig. 2.1. In other words, the transformation of the particle's trace-space plot after propagating along a lattice is mathematically described by its transfer matrix. This geometrical transformation can be decomposed to a rotation and a scaling [12], with the area of the ellipse staying nevertheless constant.

Sometimes it is useful to present the trace-space coordinates normalized by the corresponding C-S parameters, forming the *normalized trace space* (q_N, q'_N):

$$\begin{pmatrix} q_N \\ q'_N \end{pmatrix} = \begin{pmatrix} \frac{1}{\sqrt{\beta_q}} & 0 \\ \frac{\alpha_q}{\sqrt{\beta_q}} & \sqrt{\beta_q} \end{pmatrix} \begin{pmatrix} q \\ q' \end{pmatrix} , \tag{2.20}$$

In this alternative representation of the trace space, the particle trajectories form circles instead of ellipses. The geometrical transformations in this case are simple rotations of angle equal to the phase advance ϕ_q [12].

2.1.2 Multi-particle dynamics

The analysis so far treated only single particles. However, accelerators normally use continuous or bunched particle beams of millions or billions of particles. Each of these particles occupies its own state in the trace space, as a part of the total trace-space volume of the beam, which is described by a density distribution function $f(x, x', y, y', z, \delta p_z/p_z)$. In order to quantify

the trace-space dimensions of the whole beam, the statistical moments of this distribution are used and more specifically the second-order or rms (root mean square) moments:

$$\sigma_q = \sqrt{\langle q^2 \rangle} = \sqrt{\frac{1}{N}\int q^2 f \, \mathrm{d}q - \left(\frac{1}{N}\int q f \, \mathrm{d}q\right)^2}, \tag{2.21}$$

$$\sigma_{q'} = \sqrt{\langle q'^2 \rangle} = \sqrt{\frac{1}{N}\int q'^2 f \, \mathrm{d}q' - \left(\frac{1}{N}\int q' f \, \mathrm{d}q'\right)^2}, \tag{2.22}$$

where N is the number of particles in the beam, given by the integral of f over the whole 6-D space, and q=$\{x, y\}$ for the transverse plane. Eq. 2.21 represents the *rms beam size*, while Eq. 2.22 the *rms beam divergence*. The transverse *beam covariance* is given by:

$$\sigma_{qq'} = \langle qq' \rangle = \frac{1}{N}\iint qq' f \, \mathrm{d}q \, \mathrm{d}q' - \frac{1}{N^2}\int q f \, \mathrm{d}q \int q' f \, \mathrm{d}q' \, . \tag{2.23}$$

The moments above are summarized in a matrix known as the *covariance* or *sigma matrix*:

$$\Sigma_{qq} = \begin{pmatrix} \langle q^2 \rangle & \langle qq' \rangle \\ \langle qq' \rangle & \langle q'^2 \rangle \end{pmatrix}, \tag{2.24}$$

which can refer to a single plane (q, q') or to both transverse planes (x, x', y, y') (4×4 matrix) and even all trace planes $(x, x', y, y', z, \delta p_z/p_z)$ (6×6 matrix) when adding the correlation or coupling terms between the different planes. The sigma matrix at a given point of the beamline z_i can be transported to another point z_f, when the transfer matrix between the two points M_q is known [22]:

$$\Sigma_{qq,f} = M_q \Sigma_{qq,i} M_q^T \, , \tag{2.25}$$

where $\Sigma_{qq,f}$ stands for the sigma matrix at z_f, $\Sigma_{qq,i}$ for the initial sigma matrix and M_q^T for the transposed matrix of M_q.

The particles of an ideal beam have trajectories that never intersect each other, keeping a *laminar flow*. In this case, external fields can be employed to transversely focus the beam to a single point and impose a propagation with no transverse divergence (parallel particle trajectories) [23]. In reality however, the particles are born with a random distribution of transverse momenta at each position. This *thermal* contribution reduces the laminarity of the beam, making the ideal focusing and propagation impossible. The

most common way to quantify this property of the beam, which is basically a widening of its trace-space portrait, is the *trace-space rms emittance* ε_q, usually mentioned as just emittance [22]:

$$\varepsilon_q = \sqrt{\langle q^2 \rangle \langle q'^2 \rangle - \langle qq' \rangle^2} \,. \tag{2.26}$$

In order to use a quantity which is independent of the acceleration the beam has received, the *normalized emittance* ε_n can be used instead [22]:

$$\varepsilon_{qn} = \beta_{rel}\gamma_{rel}\varepsilon_q \,, \tag{2.27}$$

where the emittance is multiplied with $\beta_{rel}\gamma_{rel}$ so as to avoid the dependence of the q' terms on the beam's momentum (see Eqs. 2.5 and 2.6). The normalized emittance is often used to indicate the quality of a particle beam, as it represents its coherence and its ability to be focused.

The evolution of the distribution function of the phase-space density f is governed by the Vlasov equation, which combines Liouvilles theorem, Maxwell's equations and the equations of motion [22]. Liouville's theorem states that the volume occupied by the beam in the 6-D phase space remains constant, when conservative forces act on the beam and no binary collisions take place between particles. When additionally there is no coupling between the horizontal, vertical and longitudinal planes, the same applies to each 2-D phase space.

Despite its practicality, the emittance cannot fully characterize the phase-space density: the conservation of the phase-space volume corresponds to a constant normalized emittance only when the net applied force is linear with respect to the particle position. Otherwise, non-linear forces bend the beam in the trace-space configuration, increasing thus its emittance (example in Fig. 2.3), without nevertheless affecting its phase-space area [23].

The quantities mentioned above can be combined with the paraxial ray equation in order to derive an equation which describes the behaviour of the envelope of the beam [19]. As it is going to be discussed in Section 4.2, it is common to define the envelope of the beam (R in case of transverse symmetry or X and Y otherwise) as a radius with two times the length of the rms beam size, which has four times the rms emittance ($\epsilon_q = 4\varepsilon_q$). The result is the *beam envelope equation*, which for the 1-D case is given by [19]:

$$R'' + \kappa_0 R - \frac{\epsilon_r^2}{R^3} = 0 \tag{2.28}$$

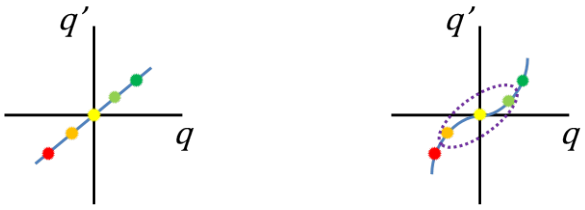

Figure 2.3: Trace-space plot (q=$\{x, y\}$) of a five-particle beam (represented by coloured dots) with zero trace-space area under the effect of linear (left) and non-linear (right) forces. The beam emittance is zero only in the left plot; the rms ellipse is schematically drawn with purple colour in the right plot.

and for the 2-D case by:

$$X'' + \kappa_{x0} X - \frac{\epsilon_x^2}{X^3} = 0\,, \tag{2.29}$$

$$Y'' + \kappa_{y0} Y - \frac{\epsilon_y^2}{Y^3} = 0\,. \tag{2.30}$$

The negative term in the above equations represents the *emittance pressure*, or else the defocusing opposed to the beam by the stochasticity of the particles' transverse momenta.

A convenient way to summarize the rms properties of a beam's trace space is through an ellipse of corresponding orientation, in an analogy to the single-particle dynamics. The boundaries of this ellipse extend up to the rms beam size and divergence of the beam in the respective axes and its area is equal to the emittance value multiplied by π. The C-S or Twiss parameters of the beam are defined as [19]:

$$\beta_q = \frac{\langle q^2 \rangle}{\varepsilon_q}\,, \tag{2.31}$$

$$\gamma_q = \frac{\langle q'^2 \rangle}{\varepsilon_q}\,, \tag{2.32}$$

$$\alpha_q = -\frac{\langle q q' \rangle}{\varepsilon_q}\,, \tag{2.33}$$

for q=$\{x, y\}$. The emittance of the beam can be expressed via:

$$\gamma_q \langle q^2 \rangle + 2\alpha_q \langle q q' \rangle + \beta_q \langle q'^2 \rangle = \varepsilon_q \tag{2.34}$$

and Eqs. 2.11 and 2.12 are still valid.

The C-S parameters of two points in a beamline and the corresponding transfer matrix in between reciprocally determine one another. When the initial and final C-S parameters are known together with the phase advance in between, the transfer matrix between z_i and z_f can be calculated by [24]:

$$M_q = \begin{pmatrix} \sqrt{\frac{\beta_{qf}}{\beta_{qi}}}\,(cos\phi_q + \alpha_{qi} sin\phi_q) & \sqrt{\beta_{qf}\beta_{qi}}\, sin\phi_q \\ -\frac{1+\alpha_{qf}\alpha_{qi}}{\sqrt{\beta_{qf}\beta_{qi}}}\sin\phi_q + \frac{\alpha_{qi}-\alpha_{qf}}{\sqrt{\beta_{qf}\beta_{qi}}}\cos\phi_q & \sqrt{\frac{\beta_{qi}}{\beta_{qf}}}\,(cos\phi_q - \alpha_{qf} sin\phi_q) \end{pmatrix} \tag{2.35}$$

As in the single-particle dynamics, the whole beam will undergo linear geometrical transformations in the trace space while propagating along linear fields. These transformations will be reflected in the beam's trace-space portrait (without changing its area or volume) and are again mathematically described by the transfer matrices.

2.1.3 Focusing elements

There are two types of elements that are commonly used to provide transverse focusing forces: the solenoid and the quadrupole magnets. The solenoids are cylindrical magnets, positioned along the axis of propagation, which provide radial magnetic fields at their edges and axial magnetic fields at their main part (sketch in Fig. 2.4). As a particle passes through them, it initially gains an azimuthal momentum from the radial fields, as Eq. 2.7 suggests. The obtained azimuthal momentum is then transformed from the axial fields to a radial momentum, yielding a linear focusing effect. The strength of the induced radial focusing of a solenoid is given by:

$$\kappa_0 = \left(\frac{QB_z}{2p}\right)^2, \tag{2.36}$$

where Q is the particle charge, B_z the constant axial magnetic field of a long solenoid and p the particle momentum. The radial fields at the exit of the magnet, opposite to the ones at the entrance, cancel the initially gained azimuthal momentum. The advantage of these lenses is that they provide symmetric transverse focusing, but the magnitude of the produced field is

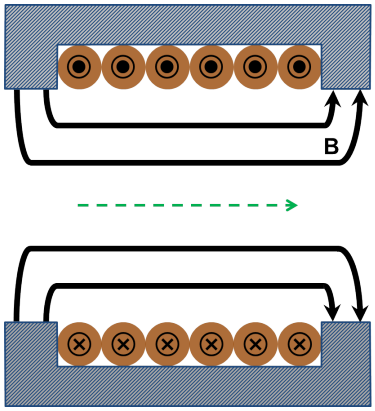

Figure 2.4: Sketch of a radial cross-section from a solenoid magnet with its magnetic field (black lines), windings (brown circles) and core (gray polygon). The green line in the center shows the direction of the beam propagation.

usually limited, making them suitable only for low particle energies. More details can be found in [19, 21].

On the contrary, the magnetic quadrupoles can provide much stronger focusing compared to the solenoids, in the expense though of transverse symmetry. These elements are comprised of four magnetic poles diagonally distributed around the axis of propagation, as shown in Fig. 2.5. The magnitude of the created fields is linear with respect to the distance from the magnetic center and equal for the two transverse directions. The resulting force has an opposite effect on each transverse plane of the beam, focusing it in one direction while defocusing on the other. The focusing strength of an ideal quadrupole lens is given by:

$$\kappa_{x0} = \frac{Q}{p}\frac{\partial B_y}{\partial x} = \frac{Q}{p}\frac{\partial B_x}{\partial y} = \kappa_{y0}\,, \tag{2.37}$$

where the partial derivatives of the transverse magnetic field components represent the magnetic gradients at each transverse direction. In order to highlight the opposite transverse focusing it is often denoted $\kappa_{x0} = -\kappa_{y0}$.

Since quadrupoles have the property of focusing the beam in one transverse plane while defocusing in the other, they are usually combined in periodic structures to achieve a controlled transport for both planes. One of the most commonly used structures is the so-called FODO lattice, which is a sequence of a quadrupole (F), a drift space (O), an identical quadrupole of

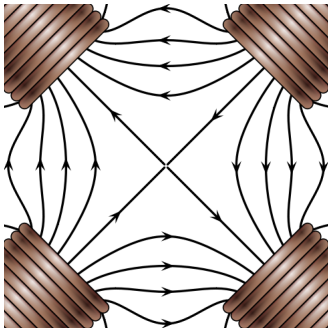

Figure 2.5: Transverse magnetic fields (black lines) created by the poles of a quadrupole magnet (bronze coils); the beam propagation is perpendicular to the page plane. Image courtesy of Wikimedia Commons.

opposite polarity (D) and another drift space of the same length as before (O), as depicted in Fig. 2.6. The length of the drift space is denoted with L and the length of the magnetic fields with l.

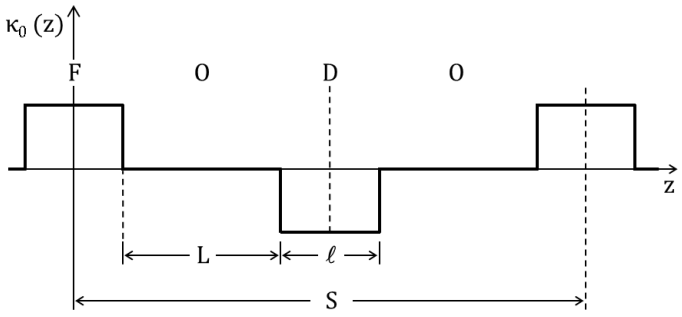

Figure 2.6: Schematic representation of the focusing strength κ_0 along a FODO lattice of total length S, drift length L and magnetic field length l.

Due to their mechanical design, magnets normally create a fairly constant magnetic field along z towards their center, while towards their edges the magnetic field drops gradually. The magnetic fields in the extremes are called *fringe fields* and for certain applications it is necessary that they are taken into consideration. When this is not necessary, the magnets are usually modelled having a longitudinally uniform magnetic profile that provides the same integrated field as the magnet. This *hard-edge* magnet is characterized

by its length, known as the *effective length* l_e, usually calculated as [19]:

$$l_e = \kappa_{0,max}^{-1} \int_0^{l_m} \kappa_0(z)\,\mathrm{d}z\,, \tag{2.38}$$

where $\kappa_{0,max}$ is the strength which corresponds to the peak of the magnetic field, l_m is the span of the magnetic field including the fringe fields and $\kappa_0(z)$ the longitudinal profile of the magnet's strength.

When, in addition, the focal length f of a focusing magnet is much bigger than its length ($f = \kappa_0^{-1} l^{-1} \gg l$), it can be modelled as a thin lens and its transfer matrix can be simplified [19]. This approach is known as the *thin lens approximation* and is especially useful for modelling the FODO lattice. An important result is the calculation of the required focusing strength for a desired phase advance at the end of the lattice ψ. Two versions are available, one from [25]:

$$\kappa_0 \approx \frac{4}{Ll} \sin\frac{\psi}{2} \tag{2.39}$$

and one from [26] (with the condition of $\psi \ll \pi/2$):

$$\kappa_0 \approx \frac{\psi\sqrt{3}}{l^2} \left[1 + 4\frac{L}{l} + 3\left(\frac{L}{l}\right)^2\right]^{-1/2} \tag{2.40}$$

For $\psi{=}\pi/4\,\mathrm{rad}$, $L{=}0.337\,\mathrm{m}$ and $l{=}0.043\,\mathrm{m}$, which is a typical case for PITZ [1], the first one gives a value of $\kappa_0{=}46.8\,\mathrm{m}^{-2}$, the second one $\kappa_0{=}50.0\,\mathrm{m}^{-2}$ while simulation codes calculate $\kappa_0{=}48.7\,\mathrm{m}^{-2}$, proving that the approximation formulas are quite accurate.

In the general case, the procedure of adjusting the parameters of the magnetic elements in order to achieve specific beam parameters at certain locations along the beamline shall be referred as *beam matching*. This adjustment of the optics of the lattice by influencing the transfer matrices M usually through κ_0, changes the propagation of the C-S parameters and the beam in the phase space, until the target features are achieved [27].

A known property of the ferromagnetic materials used in the electromagnets is the *hysteresis* of the magnetic field, or in other words the dependence of the induced magnetic field on the magnetisation process [21]. The result of this phenomenon is that there is not a one-to-one correspondence between

[1] more details can be found in the following chapters

the applied current and the magnetic field, unless a certain procedure has been followed. The usual way to address this issue is to apply maximum current to the magnet and then reduce it to the desired value, assuming that the correlation between the current and the field is known for this path. When the current drops afterwards to zero, a magnetic field still remains and only goes to zero after a procedure known as *degaussing* has been applied, which involves alternating the magnet's current while reducing its magnitude [28].

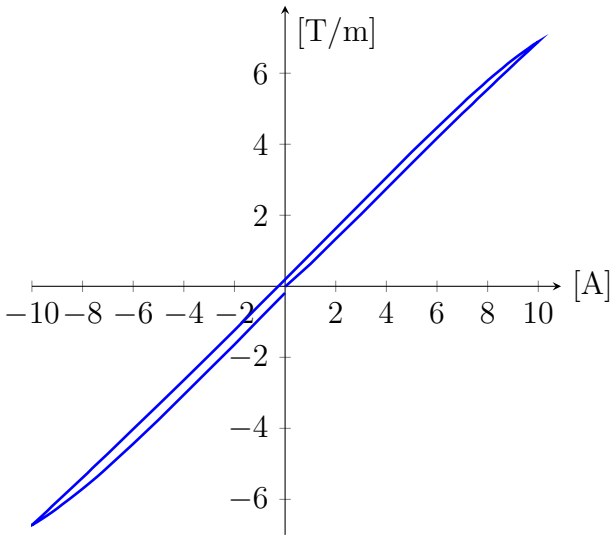

Figure 2.7: Current to gradient excitation curve of a PITZ quadrupole with initially zero remnant field. The magnet current is ramped up from 0 to 10 A, then down to -10 A and finally back to 0 A.

Besides the hysteresis, the precise positioning of the focusing elements has to be taken into consideration. Potential misalignments of a magnet with respect to the axis of propagation (offsets and rotations in all directions) will oppose an altered magnetic field to the beam, which will influence mostly applications that employ dense optics, such as the phase space tomography [10]. Finally, manufacturing imperfections which may introduce non-linear transverse magnetic fields and eventually increase the beam emittance are typically insignificant, especially for linacs.

Except from the focusing magnets, transversely deflecting magnets are needed in order to bring the beam in the expected trajectory. This task is carried out by the dipole magnets, which create a uniform field perpendicular to the beam's motion and the direction of deflection, according to Eq. 2.7.

Such a field is experienced by the particles also when passing through a quadrupole off-axis. In that case, apart from the induced focusing, the particles also receive a deflection towards a direction which depends on the transverse position they propagate inside the quadrupole.

2.2 Phase space tomography

One of the established methods to measure the phase space of a particle beam is to utilize *phase space tomography* (PST). This measurement technique integrates the principles of tomography into the beam dynamics of the longitudinal [5] and the transverse phase space [10]. The subject of this thesis focuses only on the transverse PST.

2.2.1 Basics of tomography

In the recent years, tomography is being employed in a wide range of diverse fields as an imaging technique. Its roots lay in the medical sector, which still holds as its most common application. In the general case, tomography is a way of imaging a 2-D sample or cross-section by capturing its 1-D projections from different positions around it. These projections are then algorithmically superimposed in order to create a 2-D representation of the examined object.

The mathematical model of the underlying mechanism was first introduced by J. Radon [29] and can be analytically solved with the aid of the Fourier Slice theorem [30]. The original sample shall be represented by a density distribution function $f(x, y)$. Its 1-D projections can be imaged either at a projection screen which moves around the stationary sample or at a fixed projection screen while rotating[2] the sample itself. With the two alternatives being equivalent, the second one is more representative for the studied case. As an example, the projection screen can be considered to be parallel to the horizontal plane. The projection of $f(x, y)$ on this plane $p(x)$ is equal to:

$$p(x) = \int f(x, y)\, \mathrm{d}y\,. \tag{2.41}$$

In order to obtain the next projection, a linear geometrical transformation described by a 2×2 matrix T_m is going to be applied to the sample, changing

[2]or, more generally, applying linear geometrical transformations to

the coordinate system to (x_m, y_m) as:

$$\begin{pmatrix} x_m \\ y_m \end{pmatrix} = T_m \begin{pmatrix} x \\ y \end{pmatrix} . \tag{2.42}$$

The density distribution will then be described by $f(x_m, y_m)$ in the new coordinate system. The horizontal projection $p_m(x)$ of the transformed distribution is then given by:

$$p_m(x) = \int f(x_m, y_m)\, \mathrm{d}y \,, \tag{2.43}$$

which is equivalent to the projection of $f(x, y)$ in the direction of y_m along x_m or, in other words, to the *Radon transform* of the density distribution function parametrized by T_m.

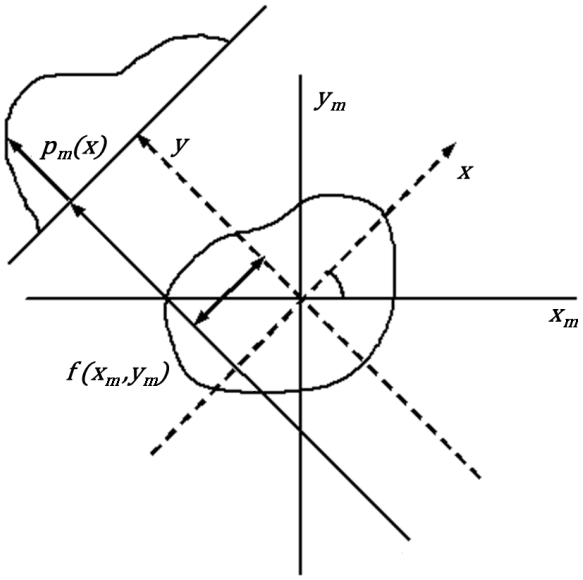

Figure 2.8: Projection of a sample with distribution function $f(x_m, y_m)$ in the direction of y along the x axis. The coordinate system (x_m, y_m) is rotated with respect to (x, y). Image courtesy of Wikimedia Commons.

According to the Radon theorem, the values of a 2-D function are uniquely determined by its Radon transform in all directions. In other words, it is possible to obtain a distribution function $f(x, y)$ using its 1-D projections

from all directions. This backward transformation is mathematically possible through the 2-D inverse Fourier transform of the complete set of $p_m(x)$ projections, after they have been transformed in the Fourier space [31].

In practical applications, only a limited number of projections of the sample can be obtained. In this case, the inverse Fourier transform introduces artefacts that deteriorate the quality of the reconstructed distribution. In order to tackle this problem, other approximative methods have been conceived that are suitable for different ranges of available projections. The most straightforward methods are the *simple backprojection* or the *filtered backprojection* [32], which perform well for a big number of captured projections. When this is not the case, iterative reconstruction algorithms can be used, like the *algebraic reconstruction technique* [33] or the *Maximum ENtropy algorithm* (MENT) [31, 34].

All of the above reconstruction techniques are available at PITZ, with MENT being the standard option due to its good performance for a small number of projections [10, 35]. The main principle of this method is that the most probable distribution to be observed — out of all the possible solutions from the limited projection data — is the one which can be produced by nature in the greatest number of ways [36]. This property in statistical thermodynamics is quantized by the entropy, which represents the "smoothness" or "simplicity" of a distribution. Therefore, the solution which maximizes the entropy, i.e. the distribution with the least frequent large fluctuations or the lowest information content consistent with the available data, has the largest probability to be observed. Using this criterion, the reconstructed distribution is obtained by an iterative optimization algorithm [31].

Every reconstruction procedure, regardless the exact implementation, takes as input the captured 1-D projections and their corresponding transformation matrices and outputs the resulting 2-D density distribution. Intuitively, in order to optimize the reconstruction result, the projections should:

- be as many as possible,
- cover a range of directions which is as wide as possible,
- be distributed around the sample as equally as possible.

2.2.2 Tomography in the transverse trace space

The idea of tomography can be extended from the real space to the trace space when dealing with particle beams. In this case, the beam's density distribution function is sampled and reconstructed in (q, q') for $q=\{x, y\}$.

According to the beam dynamics analysis earlier in this chapter, the beam is geometrically transformed in the transverse trace space as it propagates along the beamline. These transformations are simple rotations of angle equal to the phase advance in the normalized trace space, or shearings described by the transfer matrices in the non-normalized trace space. In order to achieve an optimal tomographic sampling of the beam, these transformations can be controlled by the applied focusing fields (or alternatively by the adjustment of the drift lengths).

The required 1-D projections for the reconstruction in the trace space are the spatial projections $p_m(q)$ for each transverse plane, which are common both in the real space and the trace space (example shown in Fig. 2.9 for the horizontal plane). Taking advantage of this property, the spatial projections at each transverse plane can be captured using intensity profile monitors, such as wire-scanners, fluorescent or optical transition radiation screens. The geometrical transformations of each projection in the trace space is then given by the transfer matrix M_{mq}, which can be calculated either directly from the involved lattice elements or indirectly through Eq. 2.35 when the C-S parameters are known. The algorithmic reconstruction of the projections using the corresponding transfer matrices for each transverse plane reveals in the end the trace-space distribution in that plane.

There are two ways of implementing phase space tomography, according to how the projections are being obtained:

- using a single magnet[3] with varying focusing strength for the trace space transformations and a single screen for the projections,

- using a series of magnets (commonly a FODO lattice) of fixed focusing strength with a series of projection screens placed in between.

The first approach is much easier to be realized, as the hardware is already available in most machines, and can extract a big number of projections. The second one offers as many projections as the number of screens in the

[3]or a single set of magnets

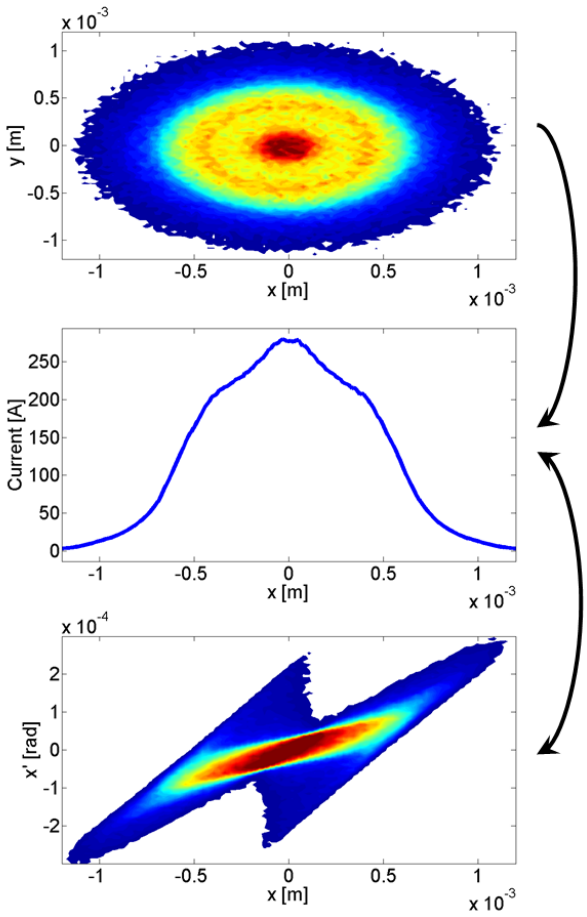

Figure 2.9: A beam in the real space (x, y) (top) and the horizontal trace space (x, x') (bottom), with their common horizontal projection (middle).

dedicated lattice and requires a specific beam matching before the data acquisition. Nevertheless, once the matching is successful and when iterative methods are used for the reconstruction, the second implementation has more advantages, maximizing the benefits of the tomographic measurement which are mentioned in the following paragraph.

Initiating from the Duke University Mark III electron linac [37], the phase space tomography was initially proposed as a tool for direct measurements of the beam's trace space at energy regimes where the methods with intercepting apertures cannot cope with the energy deposited by the beam. Even at lower energies, tomography offers a high signal-to-noise ratio which

allows measurements using single bunches simultaneously for both transverse planes, reducing thus the statistical errors and the measurement time. Phase space tomography even has the potential to provide on-line, quasi-non-destructive measurements, when beams of many identical bunches can be generated. The required setup for this operation is going to be explained in the next chapter, as part of the phase tomography module at PITZ.

While the application of the method is straightforward for beams of low charges and high beam energies, it is not the same when the repulsive self forces of the beam become intensive. In that case, the effect of space charge has to be included in the transfer matrices so that the correct description of the phase-space transformations is provided as input for the reconstruction (see Chapter 4). Except from the description of the transfer matrices, space charge creates difficulties in the beam matching, an issue which is addressed in the Chapters 5 and 6 for different types of lattices. What is not treated in the analysis of this thesis, is the coupling between the two transverse planes, which in optimized operating conditions should be minor.

Chapter 3

PITZ layout

The general components and diagnostics at PITZ are presented in this chapter with a focus on the parts related to the measurement of the transverse emittance. More details are given for the Phase Space Tomography (PST) module, explaining the components involved in the data acquisition and the beam matching, as well as the design beam dynamics and performance in the absence of space charge.

3.1 General PITZ layout

PITZ is mainly operated as a facility which tests, characterizes and optimizes photo-injectors, which are used as electron sources at FLASH [1] and the European XFEL [3] facilities in Hamburg, Germany. Except from the performance of the system itself, the properties of the generated beam are measured by a complex of diverse diagnostic devices. Lately PITZ is being upgraded in order to facilitate additional experiments, such as the PWA experiment [6].

A schematic overview of the PITZ facility with its main components is given in Fig. 3.1. The components related to the electron beam generation, i.e. the photo-cathode laser system and the RF photo-gun surrounded by solenoids, are labelled as GUN on the upper left part of the figure. Following are a number of dipole steerers for the beam transport and a series of diagnostics for the electron beam, among which is the Low Energy Dispersive Arm (LEDA) for momentum measurements. Further downstream a second accelerating cavity, the CDS booster, separates the preceding *low en-*

ergy section from the succeeding *high energy section*. The latter is equipped with a magnetic quadrupole lattice for the beam transport and matching and various electron beam diagnostics. These diagnostics include, among others, two High Energy Dispersive Arms (HEDA 1 and 2) and a Transverse Deflecting Structure (TDS) for longitudinal measurements, three Emittance Measurement SYstems (EMSY 1, 2 and 3) for transverse measurements and the Phase Space Tomography module (PST). Details of the aforementioned components are going to be presented below.

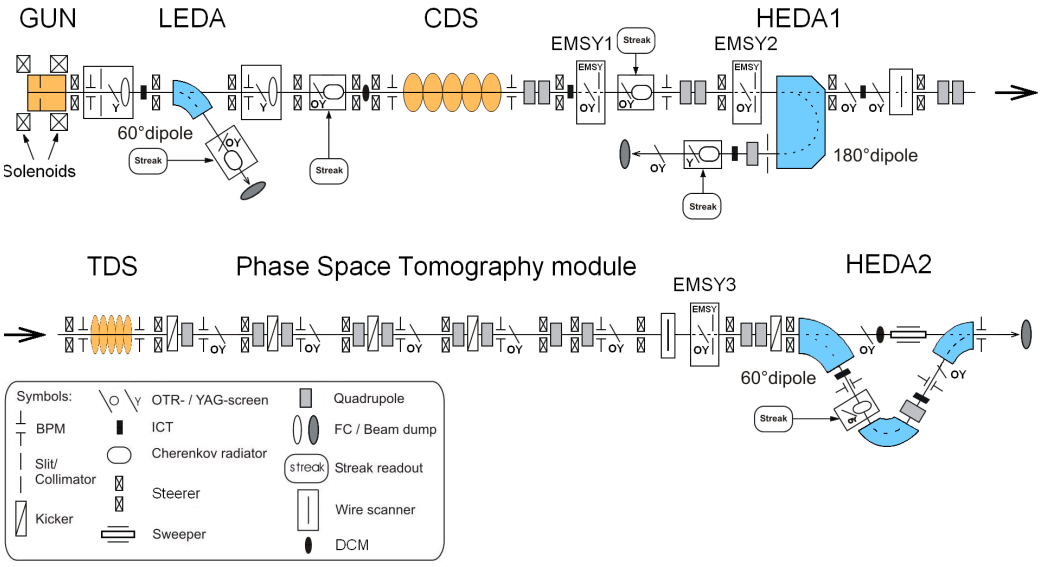

Figure 3.1: Schematic layout of the PITZ facility with its main components, as described in the body of the text. The beam propagates from left to right.

3.1.1 Photo-cathode laser system

Photo-injectors are laser-driven electron sources. At PITZ, the electrons are generated when an ultra-violet laser pulse hits the surface of a cathode with an active layer of Cs_2Te [38] in conditions of ultrahigh vacuum and strong electric RF fields. Due to the high quantum efficiency of Cs_2Te, electron bunches of up to several nC charge can be extracted with the available laser power [39]. The laser system [40, 41] can produce pulse trains of up to 800 micro-pulses with 1 μs temporal spacing at a repetition rate of up to 10 Hz.

The laser energy is remotely adjustable up to $\sim 10\,\mu$J per micro-pulse.

The transverse and longitudinal distribution of the laser beam has a significant influence on the properties of the electron beam, determining its space-charge forces. The transverse rms radius of the laser beam can be controlled by a Beam Shaping Aperture (BSA) in a typical range between 0.05–0.44 mm at the cathode surface. The position of the laser beam with respect to the BSA can be controlled via a set of mirrors, in order to achieve optimum homogeneity of the laser transverse profile at the cathode. The longitudinal shape of the laser pulse can also be adjusted, with the two most common options being a ~ 2 ps full width at half maximum (FWHM) short Gaussian profile and a 20–25 ps FWHM long flat-top profile with 2–3 ps rise and fall time [5, 38] (Fig. 3.2). Several diagnostics for the laser beam are available at PITZ [42].

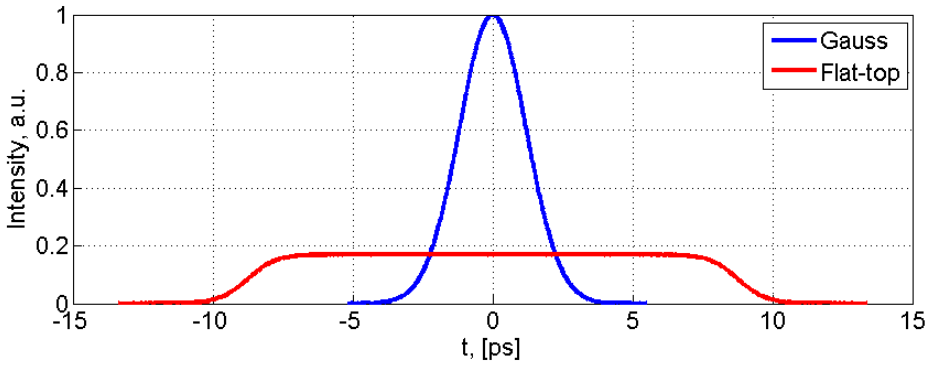

Figure 3.2: Simulated temporal profiles of the long flat-top and the short Gaussian laser pulses used at PITZ. Image courtesy [5].

3.1.2 Accelerating cavities

The most vital part of a photo-injector is the accelerating cavity, also referred as the *electron gun* or *RF photo-gun*. Operated at pulsed mode in the *L*-band range, the radio-frequency (RF) cavity at PITZ is a normal-conducting, 1.6-cell structure with a resonance frequency of 1.3 GHz. It has been shown to withstand a maximum average power of 50 kW [43] and is powered by a 10 MW klystron with RF pulses up to 900 μs duration and 10 Hz repetition rate. The highest gradients achieved are in the order of 60 MV/m which accelerate the photo-electrons up to 7 MeV/c [39] in momentum. Inseparable

from the gun are the two solenoid magnets around it, which are responsible for the beam focusing (further details in Subsection 3.1.3). A 3-D model of the electron gun and the solenoid magnets is shown in Fig. 3.3.

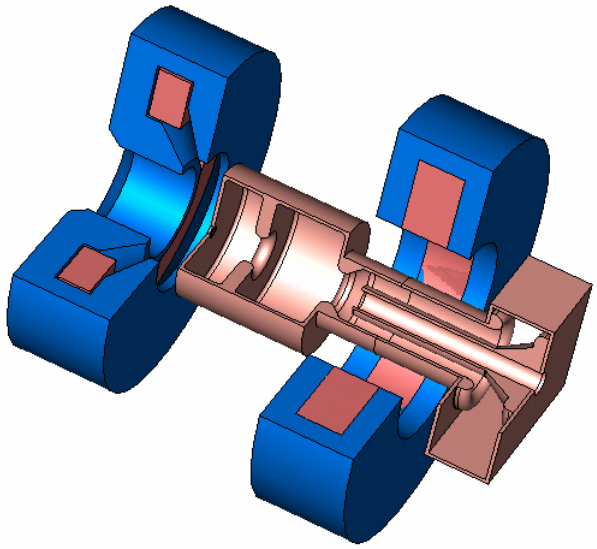

Figure 3.3: 3-D model of the electron-gun (bronze) at PITZ surrounded by two solenoid magnets (blue). The bucking solenoid (left) is located behind the cathode (black dot at the left edge of the gun) and the main solenoid (right) at the exit of the cavity. The laser beam enters from right to left, hits the cathode and produces electrons, which are accelerated towards the right direction.

The electron beam quality is mainly determined in the gun region, but it is more convenient to measure it at higher energies. Therefore, a second accelerating cavity is located about 4 m downstream and is referred as the *booster*. The booster is a 14-cell normal-conducting RF cavity based on a cut disk structure and can provide an accelerating gradient of up to 14 MV/m [44]. Currently its peak power is restricted to 4 MW, which gives a final momentum gain of about 15 MeV/c. The section upstream the booster is referred as the *low energy section* and downstream as the *high energy section*.

The phase of the RF wave which the beam experiences at each cavity can be remotely adjusted in order to obtain the desired beam parameters for each application. This phase is usually defined with respect to the *maximum mean momentum gain* (MMMG) or *on-crest* phase, where the beam gains its

maximum longitudinal momentum. Close to this value lies the phase where the momentum spread is minimized [39].

3.1.3 Magnetic elements

As already mentioned, an essential part of the photo-injector are the solenoid magnets which are placed around the gun cavity. The main solenoid magnet, placed 0.276 m downstream the cathode surface, is responsible for providing transverse focusing to the generated electrons with a maximum peak longitudinal magnetic field of 0.29 T [42]. The bucking solenoid is placed behind the cathode (Fig. 3.3) and is set such, that it cancels the residual magnetic field of the main solenoid at the cathode plane, so that no angular momentum is induced to the generated electrons. The adjustment of the magnetic field of the solenoids is crucial for the emittance compensation, as it is going to be explained in Chapter 6.

For the beam transport as well as the measurement of the longitudinal properties of the beam at PITZ, dipole magnetic fields are used. 21 corrector dipole magnets are installed along the machine serving as horizontal and vertical steerers in order to correctly guide the electrons to the optimum path along the beamline. Moreover, three stronger dipole magnets [5], one upstream (named Low Energy Dispersive Arm – LEDA) and two downstream the booster (named High Energy Dispersive Arm – HEDA 1 and 2), are used as energy spectrometers in order to measure the beam momentum and momentum spread, as explained in Subsection 3.1.4.

The high energy section of PITZ is equipped with 17 quadrupoles[1] which can be used for transporting and matching the beam. All of these magnets are of the same type and they are powered independently from 10 A power supplies, with their magnetic field reaching a maximum gradient of ~ 7 T/m. Due to space constrains in the beamline, their dimensions are unusually small: the bore radius (distance between the pole tips and the magnetic axis) is 0.02 m and the pole length is just 0.021 m, creating a longitudinal magnetic profile which mainly consists of long fringe fields with an effective length of 0.043 m on average (Fig. 3.4). Therefore, the hard-edge approximation shall be avoided when increased accuracy is needed, such as in the phase space tomography. A 3-D model of a PITZ quadrupole can be seen in Fig. 3.5 and more technical details can be found in [10].

[1] excluding the ones at the bending sections

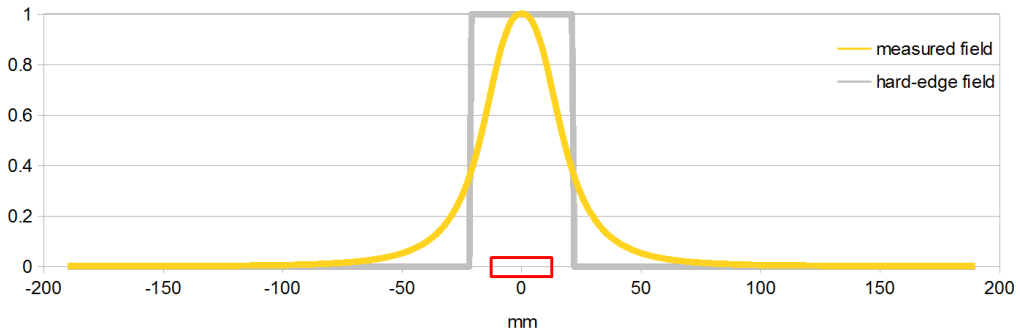

Figure 3.4: Measured and hard-edge longitudinal magnetic profile of a quadrupole at PITZ (the vertical axis in arbitrary values). The length of the magnetic poles is indicated by the red rectangle.

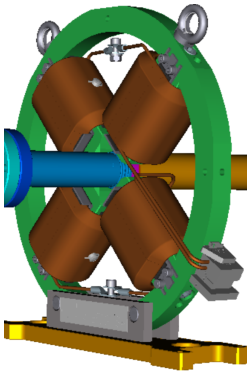

Figure 3.5: 3-D model of the PITZ quadrupoles placed around the beam pipe. The coils of the poles are drawn in bronze colour.

In order to set the desired magnetic gradient to a quadrupole, its excitation curve is needed. This curve, which is individual for each magnet, correlates the measured field gradient with respect to the applied current (example already presented in Fig. 2.7). The nominal calibration procedure for a quadrupole is to firstly degauss it, then increase the current to the maximum positive value and then reduce it down to the value which corresponds to the desired gradient. In order to avoid any dipole component from the quadrupoles, the beam has to be guided into the center of the magnet, a procedure known as *quadrupole beam-based alignment*. The exact position of the quadrupoles as well as their functionality in the tomographic measurement are described in Section 3.3.

3.1.4 Electron beam diagnostics

PITZ is equipped with a wide range of electron beam diagnostics. The ones directly or indirectly involved in the tomographic measurements are presented below.

Once the electrons have been extracted, the property which is firstly measured is usually the bunch charge. There are two alternatives for this measurement at PITZ, using Faraday cups (FCs) or integrating current transformers (ICTs). The FCs are more sensitive for lower charges but do not allow the beam to propagate further, while the ICTs perform better with higher charges and offer a non-destructive measurement. Both options are available at the low as well as the high energy section. The transverse position of the beam can be monitored by beam position monitors (BPMs) which are distributed along the beamline [42].

The transverse beam distribution can be obtained by intercepting observation screens which produce light of intensity proportional to the incident charge density. Two types of screens are available, Optical Transition Radiation (OTR) screens and Yttrium-Aluminum-Garnet (YAG) powder fluorescent screens, doped with Ce atoms on a Si substrate. The first type is used for higher and the second for lower beam energies and charge densities [45]. The emitted light is guided and collected by an optical readout system, which includes mirrors, focusing lenses and 12-bit CCD cameras managed by a video system [46]. The captured data undergoes image treatment in order to remove the background and stochastic noise.

From the longitudinal properties, the most important is the momentum of the beam. This measurement is available in both the low and high energy sections using dispersive arms with strong dipole magnets. These energy spectrometers oppose a deflection to the particles which is inversely proportional to their momentum, resolving the beam's mean momentum and momentum spread with an accuracy of a few keV/c [5], a well acceptable resolution for the requirements of the applications at PITZ. The bunch length can also be estimated using the high energy spectrometers, either through a technique which combines data from the on- and off-crest booster phases [47], or through a tomographic reconstruction of the complete longitudinal phase space, with a temporal resolution of up to 0.3 ps [5]. The upcoming operation of the TDS cavity is expected to further improve the precision of the longitudinal diagnostics [5].

Above all, PITZ specializes in measuring the transverse phase space and

more specifically the transverse emittance. All of the existing alternatives for this measurement are listed below.

3.2 Transverse phase-space measurements at PITZ

PITZ is a dedicated facility for achieving and measuring high-brightness beams of low transverse emittance [48]. Different diagnostic tools and methods are available in different locations along the beamline, some of which are able to measure the rms moments (quadrupole scan, multiscreen method) while others the full phase-space portrait of the beam (slit-scan measurement, phase space tomography).

3.2.1 Slit-scan technique

The most established method for measuring the transverse phase space at PITZ is the slit-scan technique which takes place at the Emittance Measurement Stations (EMSYs) in three locations along the beamline (5.7, 6.3 and 16.3 m downstream the cathode or 1.0, 1.5 and 11.5 m downstream the booster exit respectively). This technique utilizes thin mechanical apertures, also referred as slit masks, to measure the local divergence and covariance of the beam. Each of these slits, orthogonal to the plane they are measuring, intercepts the beam, allowing a small part of the total charge to propagate further without experiencing considerable space-charge forces. The remaining beamlet is then measured by a screen downstream, allowing the calculation of its divergence from the spread of its size in the direction which is orthogonal to the slit opening. This procedure is repeated while the slit moves along the transverse profile of the beam and the data from all the beamlets is combined to reveal the overall phase-space portrait of each transverse plane. A schematic layout can be seen in Fig 3.6 and more details are available in [48, 49].

It can happen that the low-intensity edges of the beamlets cannot be detected by the optical readout system, resulting in an underestimation of the beam size in the derived phase-space plot. In order to compensate this effect, the emittance is multiplied by the ratio of the beam size measured at the location of the slits over the respective value from the measured phase-space distribution [39, 50]. However, this scaling should not be considered

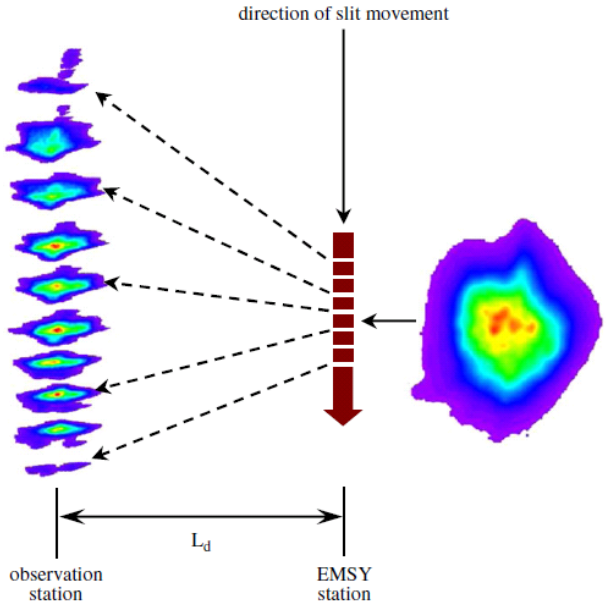

Figure 3.6: Schematic representation of the slit-scan measurement: the beam propagating from right to left is intercepted by a moving slit mask which allows only a part of the beam to continue without considerable space-charge influence. The beamlets are then measured on a screen downstream and combined to derive the beam's transverse phase-space portrait.

during the calculation of the C-S parameters without scaling accordingly the beam size, divergence and covariance from the measurement, since a shearing will be introduced to the phase-space ellipse (more information in Appendix A).

Despite having the advantage of being a direct measurement method which is not susceptible to space charge, the slit-scan technique suffers from some systematic limitations. The lower the beam charge, the more bunches are required in order to get sufficient signal-to-noise ratio from the beamlets, increasing thus the dependence of the measurement on the short-term stability of the machine. Moreover, the time difference between the measurement of the horizontal and the vertical plane increases the dependence on the machine's long-term stability as well. Another disadvantage for beam energies much higher than the ones used at PITZ, is that the materials of the slit masks cannot withstand the deposited energy. The systematic error of the measured emittance using this technique is estimated to be around 10% [48].

3.2.2 Alternative methods

Alternative methods for measuring the transverse emittance without resolving the complete phase-space plot, include the quadrupole scan technique and the multi-screen method. Both approaches are used to derive the rms moments at a specific beamline location by measuring further downstream the rms beam size for different quadrupole strengths (quadrupole-scan) or at different locations (multi-screen) [24]. Using the transfer matrix formalism, at least three ($n = 1, 2, ...$) measurements of the beam size ($\sigma_{q,n}$) at one transverse plane (q=$\{x, y\}$) together with their respective transfer matrices from the measurement location to the point of interest (M_n) can determine the rms moments at that point ($\sigma^2_{q,0}, \sigma_{qq',0}, \sigma^2_{q',0}$) through:

$$\begin{pmatrix} \sigma^2_{q,1} \\ \sigma^2_{q,2} \\ \vdots \\ \sigma^2_{q,n} \end{pmatrix} = \begin{pmatrix} (M_{11,1})^2 & 2M_{11,1}M_{12,1} & (M_{12,1})^2 \\ (M_{11,2})^2 & 2M_{11,2}M_{12,2} & (M_{12,2})^2 \\ & \vdots & \\ (M_{11,n})^2 & 2M_{11,n}M_{12,n} & (M_{12,n})^2 \end{pmatrix} \begin{pmatrix} \sigma^2_{q,0} \\ \sigma_{qq',0} \\ \sigma^2_{q',0} \end{pmatrix} = U \begin{pmatrix} \sigma^2_{q,0} \\ \sigma_{qq',0} \\ \sigma^2_{q',0} \end{pmatrix} . \tag{3.1}$$

As long as the matrix U is invertible, the system can be solved using matrix algebra. In practice, more than three beam size measurements are taken and the system is then solved using a least-squares method. The weak point of these methods is the inclusion of the space-charge effect in the transfer matrices. However, the space-charge approach developed in Section 4.4 can be applied here as well (under the described conditions) and diminish this limitation.

Finally, the phase space tomography can combine advantages of the aforementioned methods and plot the phase-space portrait of the beam without neglecting the space-charge forces, for broader ranges of beam charge and energy, in a quasi-non-intercepting measurement with fast data acquisition. Details of the implementation of the PST at PITZ are presented below.

3.3 Phase space tomography at PITZ

A dedicated module for tomographic measurements of the transverse phase space has been assembled and operated at PITZ since November 2010, with its first experimental results presented in 2011 [10]. The PST module at PITZ consists of two sections: the *tomography* or *PST section*, where the

data acquisition takes place, and the preceding *matching section*, which delivers the required beam parameters to the PST section (schematic layout in Fig. 3.7). An intermediate lattice is shared by the two sections and can be exchanged between them, depending on the wanted number of projections. The functionality, structure and components of each section are going to be described below.

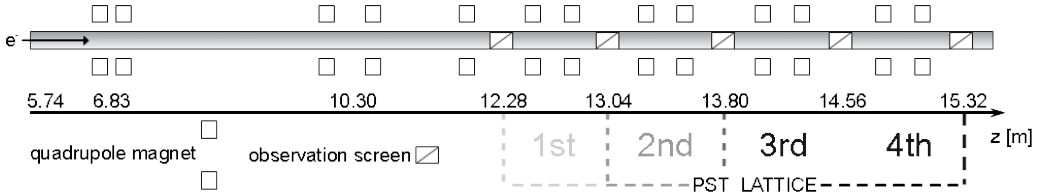

Figure 3.7: Rough schematic layout of the matching section (starting from EMSY 1 at $z = 5.74\,\mathrm{m}$) and the PST section at PITZ, with an indication of the longitudinal beamline coordinate. Depending on the number of wanted projections, the first cells of the PST lattice may be used as part of the matching section. The beam propagates from left to right.

3.3.1 PST section: components and design beam dynamics

The projections for the tomographic reconstruction are controlled and captured in the PST section, which is comprised of consecutive FODO cells bordered by observation screens [51]. The FODO cells have a drift space of L=0.337 m and a total length of S=0.76 m. In addition, each cell is equipped with a BPM and a steerer magnet in order to monitor and control the beam position (Fig. 3.8). Starting from the location of z=12.28 m downstream the cathode, a total of four FODO cells exist in the PST section, bordered by five screen stations (named PST.Scr 1-PST.Scr 5). With three projections needed as minimum for a tomographic reconstruction, standard PST measurements at PITZ have been using four projections. During the last measurement period, the tomographic measurement with five projections was firstly commissioned.

In order to achieve optimum reconstruction results, the projections need to be captured in steps of equivalent phase-space transformations[2] around the

[2]or equidistant rotations, in the normalized phase space

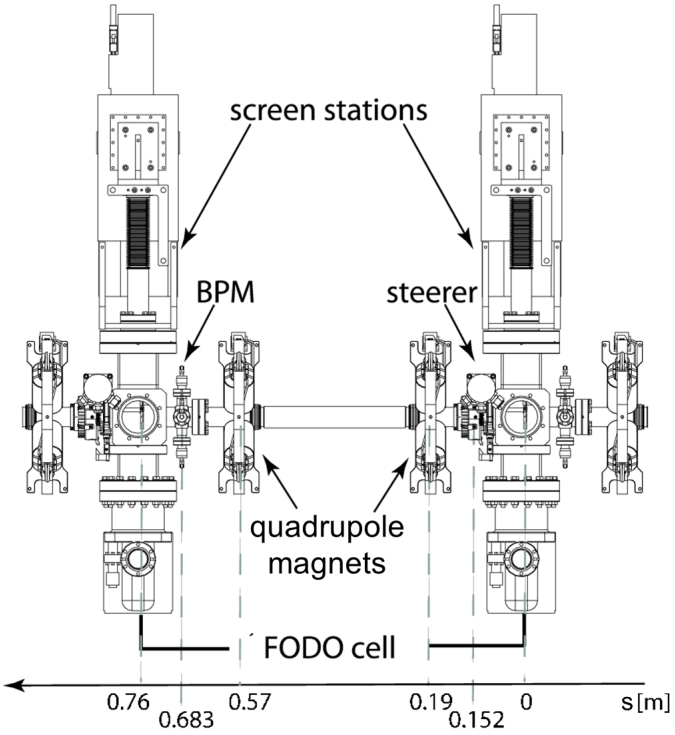

Figure 3.8: Top view of a FODO cell and its components in the PST section.

beam distribution, as proven both theoretically [12] and statistically [10, 52]. This is translated to a phase advance per cell (ψ) of 60° for the case of three projections, 45° for four projections or 36° for five projections. Therefore, the purpose of the FODO lattice is to increase the phase advance between consecutive screens by the respective value for both transverse planes, through the adjustment of the quadrupoles. The required focusing strength can be calculated from matching codes or from the approximative Eqs. 2.39, 2.40.

The Methodical Accelerator Design (MAD) software [53] is currently used as the standard matching tool for the various applications at PITZ. It is able to match the machine parameters, e.g. the quadrupole strengths, to the target beam parameters, e.g. the values of phase advance, β- and α-function. Its matching capabilities are very powerful but its major drawback is that it neglects the space-charge forces. The results from MAD for the tomography requirements using three, four and five projections are summarized in Table 3.1 and Fig. 3.9.

Projections	ψ [°]	k_0 [m^{-2}]	$\beta_{x,y}$ [m]	$\alpha_{x,y}$
three	60	63.7	0.772	$\pm$1.200
four	45	48.7	0.999	$\pm$1.125
five	36	39.3	1.233	$\pm$1.093

Table 3.1: Phase advance per cell, focusing strength and entering C-S parameters for a matched PST lattice of three, four and five projection screens, neglecting space charge.

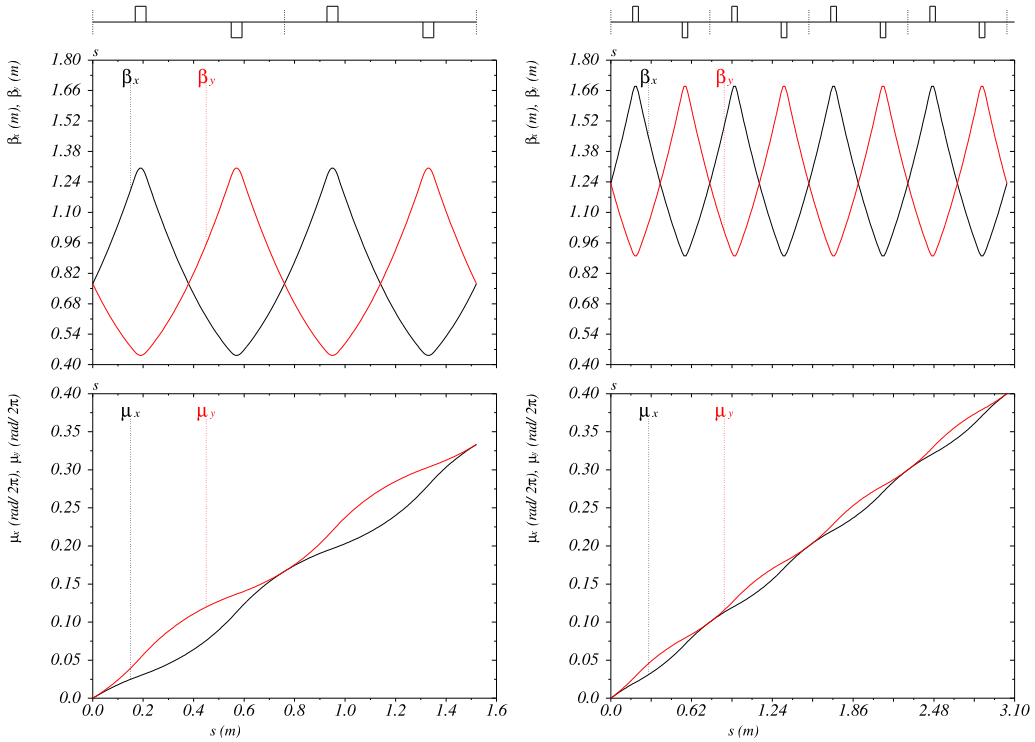

Figure 3.9: Plots of the horizontal (black line) and vertical (red line) β-function (top) and phase advance (bottom, indicated as μ in units of rad/2π) along the PST section for three projection screens (left) and five projection screens (right). The matching quadrupoles are indicated as white rectangles and the screens as dotted black lines on the top.

The periodicity and transverse symmetry of both the PST lattice and the matching constrains along it characterize the matched beam solution as well. As the number of projections increases, or else, as the desired phase

advance per cell decreases, more relaxed beam optics are required - weaker focusing strengths, bigger β- and smaller α-values. A disadvantage of using more projections on the other hand, is the fluctuations which the emittance undergoes along the longer PST lattice, as explained in Chapter 6.

The screens are inserted across the beamline with movable actuators that allow precise horizontal positioning. Each screen station hosts a YAG and an OTR screen, separated by a gap wide enough to allow the beam to propagate further [51]. The YAG screens have a 0.1 mm thick Si layer and are placed orthogonally to the beam direction with a 45° inclined mirror behind them, which guides the light output to the optical readout system. The OTR screens are placed at an incidence angle of 45° guiding the forward radiation cone to the readout system, except from the first one which is mounted orthogonally followed by a 45° mirror for the extraction of the backward radiation (for test purposes). Microbunching effects are not present in the beams produced at PITZ, therefore no signal enhancement from coherent OTR is observed. Nevertheless, the YAG screens are more suitable for the range of beam parameters typically measured, with their resolution reaching 0.06 mm rms beam sizes at 22 MeV/c beam momentum [10]. Such a resolution allows tomographic measurements of beams with $\sim$0.2 mm·mrad transverse normalized emittance, given the matching constrains.

Once the light is produced, a complex of mirrors guides it through a magnifying lens to the camera. The focal length can be selected between 140 mm and 200 mm and an adjustable aperture controls the amount of the incoming light. The digital cameras have a 12-bit CCD chip with a full resolution of 1360×1024 and square pixels of 8.3 μm size. Neighbouring pixels can be combined in sets of two when the intensity is not sufficient, in the expense of a reduced resolution of 680×512. The data acquisition using the full resolution of the cameras was firstly commissioned during the last measurement period. Finally, the captured signal undergoes image processing in order to filter the background noise and align the centroids of the projected distributions to a common coordinate system [10].

The reconstruction point is chosen to be the entering PST screen respectively for each case. This location is considered as the point with zero phase advance and is used as the reference for the calculation of the transfer matrices at each projection screen. This calculation is done either by combining the known matrices of the involved elements using Eq. 2.19, or instead using Eq. 2.35 when an estimation of the C-S parameters is available. The first option cannot take the space-charge forces into account, contrary to the

second, as it is going to be explained in Chapter 4. As already mentioned in Subsection 2.2.1, the reconstruction algorithm typically used at PITZ is MENT.

In the near future, fast kicker magnets are going to be included in the first four FODO cells (Fig. 3.10). Each kicker will be able to extract a single bunch out of the bunch train and bring it to the off-axis screen of the next cell, as the rest of the beam propagates through the gap between the YAG and OTR screen. Using the kicker magnets it will be possible to selectively measure the transverse phase space of just a single bunch, by deflecting it at each PST screen downstream PST.Scr 1. Likewise, the measurement can be repeated for all of the consecutive bunches, providing an evaluation of the stability along the pulse. When this stability is acceptable, i.e. all of the bunches in the train are almost identical, the kicker magnets can measure the transverse phase space of the beam without even destroying it, but just extracting three or four of its bunches for the PST measurement, while allowing the remaining bunches of the train to propagate further. This functionality can serve as an on-line measurement tool for monitoring the beam quality and the long-term stability of the machine.

3.3.2 Matching section: structure and features

The tomographic requirement of specific phase advance values at the projection screens is connected with the evolution of the β-function along the PST lattice, which depends not only on the applied focusing, but on the incoming β and α values as well, as Eqs. 2.10 and 2.11 suggest. The design entering C-S parameters for each type of PST measurement are summarized in Table 3.1[3].

The quadrupole lattice responsible for delivering the necessary beam parameters in front of the entering projection screen is referred as the matching section. Since the matching procedure requires the knowledge of the initial transverse beam parameters, this section practically begins at the first EMSY station and extends up to the entrance of the PST section. The available quadrupole magnets and their location along z are schematically presented in Fig. 3.7. Depending on the number of projection screens used by the tomographic measurement, the matching section may include the first unused FODO cells in order to assist the beam matching. The typical setup which

[3] a correction is necessary in the presence of space charge, described in Section 5.1

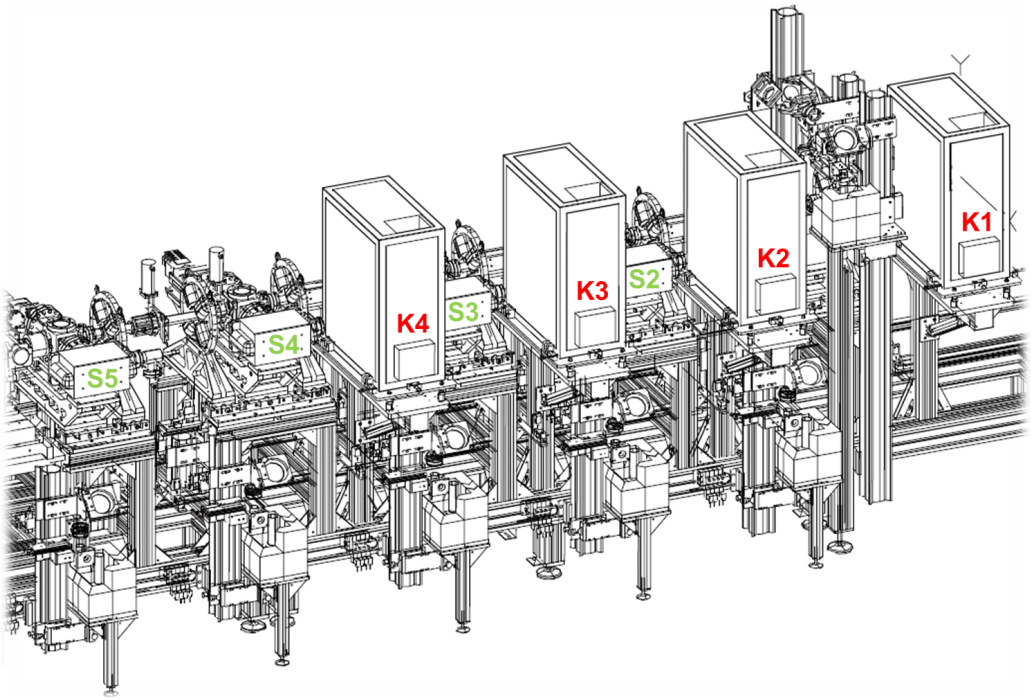

Figure 3.10: Future layout of the PST section at PITZ with an indication of the longitudinal position of the fast kicker magnets (K1–K4) and their corresponding screen stations (PST.Scr 2–PST.Scr 5 tagged as S2–S5). The direction of the beam propagation is from right to left.

has been used for measurements up to now is a PST section with four projection screens, which leaves practically 7 available quadrupoles in the matching section. In the last measurement period, measurements with five projection screens have been made as well, using 5 quadrupoles in the matching section. The case of three projections has not yet been tried at PITZ, but the 9 quadrupoles involved in the matching section are foreseen to be sufficient for the demanding requirements of this measurement.

For a number of reasons, the beam matching along the matching section is much more demanding compared to the PST section: on the one hand, the irregularity and smaller density of the focusing elements along the matching lattice, together with the transverse asymmetry of the incoming beam which is usually observed at PITZ, result in a transport with big asymmetries between the transverse planes. On the other hand, the length of the match-

ing section in combination with the demanding matching constraints lead to considerable emittance fluctuations, as explained in Chapter 6. An example of a matching scheme for a tomographic measurement with four projection screens, using the hard-edge approximation for the quadrupoles, is shown in Fig. 3.11.

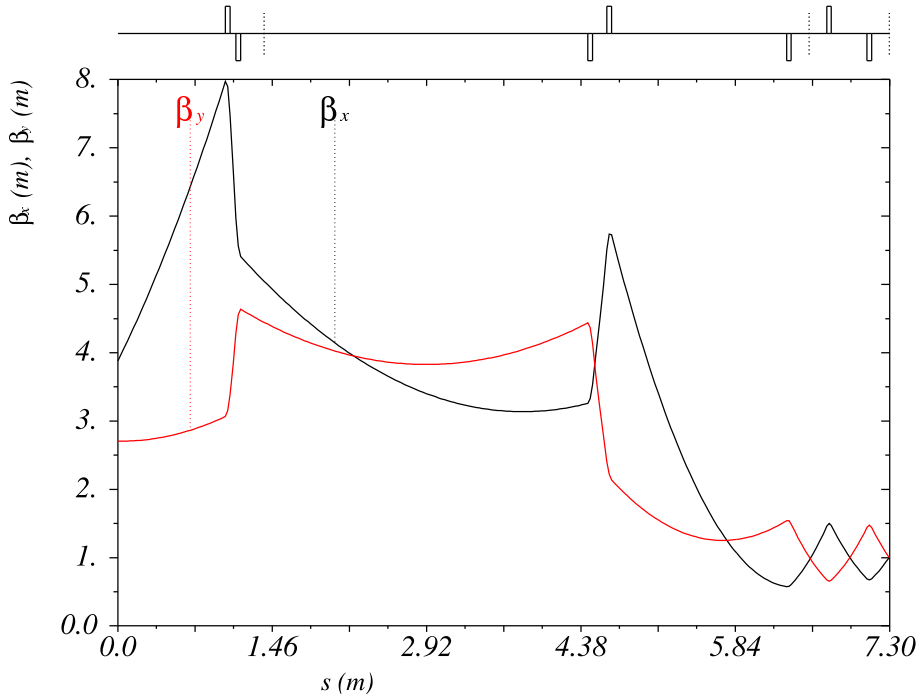

Figure 3.11: Example of a matching solution for a tomographic measurement with four projection screens, using the hard-edge approximation: β_x and β_y are plotted along the matching section (from EMSY 1 to PST.Scr 2) and the matching quadrupoles are indicated on the top as white rectangles.

The weak point of the PST measurement at machines like photo-injectors is that the initial C-S parameters required for the beam matching are not known in advance and an additional measurement is needed in order to obtain them. However, once this is done, the PST measurement can provide on-line results for beams with long bunch trains, even when the transverse properties of the beam change with time and the matching becomes less effective, using the implementation described in Section 4.5.

3.3.3 Sources of systematic errors

The systematic errors of the PST measurement at PITZ have been studied in [10] and the main results are summarized in this section. In the absence of space charge, the factors that affect the accuracy of the measurement are mostly related to the quadrupole magnets and the optical read-out system.

The specification of PITZ for 10% maximum uncertainty in the measured emittance is fulfilled at PST when the error of the measured beam size stays below 10% [10]. The uncertainty in the calibration of the optical system has been evaluated to be 2%, while the error of the quadrupole calibration to the desired gradient around 1%, including the stability of the power supplies [10]. The error in the measurement of the beam momentum, which affects the value of the quadrupole strengths, has been estimated to be below 5% at HEDA 1 [54], creating a mismatch of less than 1% at the PST section [10]. Furthermore, the fringe fields of the quadrupoles introduce additional mismatches, as shown in Subsection 4.4.2, but the treatment which is proposed in the same subsection eliminates this error.

Due to the stringent beam optics along the PST section, potential misalignments of the involved components will introduce significant errors. For the quadrupoles, the mounting tolerances at a single dimension have been calculated in rms values to be up to 0.1 mm in offset or 20 mrad in rotation, while for the projection screens a maximum longitudinal misplacement of 0.1 mm or a transverse tilt by 10 mrad in rms can be tolerated [10]. The accuracy of the measurement tools at PITZ is currently below 50 μm [55].

At last, the error which the MENT algorithm itself introduces to the reconstructed phase space, when the correct beam projections and transfer matrices are provided as input, cannot be analytically calculated and depends on the specific distribution[4]; nevertheless, simulations have shown minimal errors ($< 0.1\%$) in the reconstructed rms moments of a typical PITZ beam using four projection screens [10]. Even in the case of significant deviations from the design phase advance values, the reconstruction with MENT shows only small errors, as shown in Subsection 4.4.2.

Consequently, sufficient accuracy is expected from the PST measurement in the absence of space charge. However, the high charge density and moderate kinetic energy of the beams produced at PITZ introduce significant mismatches, which influence various aspects of the tomographic measurement and therefore have to be treated accordingly: on the one hand, the

[4] some examples are demonstrated in [31, 35]

description of the transfer matrices along the PST lattice has to be modified in order to include the repulsive self forces, otherwise the captured projections will be wrongly reconstructed. On the other hand, the beam defocusing and emittance fluctuations which are induced by space charge (as explained in Chapter 6) will have to be compensated in order to achieve the design entering C-S parameters at the PST section and the optimal phase advance values at the projection screens afterwards. As a result, the effect of space charge proves to be a dominant source of systematic error in the PST measurement and it is the aim of this thesis to quantify and eliminate it.

Chapter 4

Space charge along the PST section

In this chapter the concept of space charge is introduced and its effect along the Phase Space Tomography (PST) section is studied, simulated and incorporated. Initially the basic physics of space charge is formulated and software packages used for its simulation are presented. Afterwards, a method to include the space-charge effect in the tomographic reconstruction is introduced, followed by simulations along the PST lattice and the analysis of measured data from PITZ and ALICE (Daresbury Laboratory, UK) [56].

4.1 Basic theory of space charge

The term *space charge* is used to describe the electromagnetic (EM) fields which an individual particle experiences from the particle beam it belongs to. These fields, also mentioned as the *self fields*, are divided into two categories [57]:

- *direct*, when the EM fields originate directly from the particles of the beam
- *image*, when the source of the EM fields is a surface in the vicinity of the beam, e.g. the vacuum chamber, magnet poles etc.

The image fields appear when a beam of charged particles travels in the proximity of a conducting or dielectric plane. In order to satisfy the condition

of constant potential along that screen, a virtual "mirror" current [1] has to be assumed, opposing a transverse force onto the beam [25, 58]. The beamline at PITZ is equipped with a vacuum chamber of circular cross section (35 mm diameter along the high energy section) in order to suppress the image currents [59]. From the rest of the beamline elements, a potential source of considerable image fields is the laser vacuum mirror [60]. The effects of such fields are not included in this thesis and from this point on only the direct self fields are going to be studied.

The direct self fields appear as a result of the EM interactions inside the particle beam. When external EM fields act additionally on the beam, the overall beam behaviour resembles that of a single-component, charged plasma: each particle with charge q creates an electric potential V in a distance r around it, which in the rest frame is equal to [23, 61]

$$V = \frac{q}{4\pi\varepsilon_0 r} \exp\left(-\frac{r}{\lambda_D}\right) , \tag{4.1}$$

where ε_0 is the permittivity of free space and λ_D is defined as the *Debye length*, given by

$$\lambda_D = \sqrt{\frac{\varepsilon_0 k_B T}{q^2 n}} , \tag{4.2}$$

with k_B being the Boltzmann constant, T the (thermodynamic) temperature of the beam in the rest frame and n the particle density. In the laboratory frame, the Debye length is expressed as

$$\tilde{\lambda_D} = \sqrt{\frac{\varepsilon_0 \gamma_{rel}^2 k_B T}{q^2 n}} = \sqrt{\frac{\varepsilon_0 m_0 \gamma_{rel}^3 v_r^2}{q^2 n}} \tag{4.3}$$

where m_0 is the rest mass of the particles and v_r their transverse thermal rms velocity, which is assumed to be nonrelativistic [19].

It can be seen that V effectively affects only the particles inside a volume confined by the Debye length. Outside this sphere this potential is essentially screened off by the rest of the particles. In most usual cases, when no intrabeam scattering or emission from a cathode occurs, the Debye length is much larger than the interparticle distance, preventing particle collisions. As long as this length remains considerably smaller than the beam's dimensions,

[1] for bunched beams, otherwise charge

each local particle distribution contributes to a net electric field which shows a smooth dependence along the bunch. The particles are then subject to *collective effects* as a result of their self fields, which act on the beam in a way similar to the external applied fields. This condition is referred as the *space-charge regime* and is usually met at low particle energies for cold beams, as suggested by Eq. 4.3. On the other hand, when the Debye length is much bigger than the beam's dimensions, the Debye screening practically vanishes and *single-particle effects* prevail. This condition is usually valid at higher particle energies, where the self fields become weakened and the external fields dominate the beam dynamics, as shown in the following paragraphs.

Depending on the particle distribution, the self fields can be decomposed into components that show a linear and a non-linear dependence on the position inside the beam. The linear part of these fields has been shown to primarily influence the rms envelope equation and thus the second-order moments of beams with ellipsoidal symmetry [62]. The forces driven by these fields not only preserve the volume of the beam in the phase space, but also the beam emittance, as explained in Subsection 2.1.2. However, in Chapter 6 it will be explained how the force from such fields, in spite of being linear, can induce a correlated growth of the projected emittance that can nevertheless be eliminated. The non-linear components of the field can curve the beam in the phase space and thus increase the emittance in a practically irreversible way.

The linear component of the electric longitudinal (E_z) and transverse (E_r) space charge fields for a cylindrical bunched beam of uniform charge distribution and no energy spread are given in the lab frame by [23]:

$$E_z\left(\zeta\right) = \frac{IZ}{2\pi\epsilon_0 R^2 \beta_{rel} c} h\left(\zeta\right) , \tag{4.4}$$

$$E_r\left(r,\zeta\right) = \frac{Ir}{2\pi\epsilon_0 R^2 \beta_{rel} c} g\left(\zeta\right) , \tag{4.5}$$

where I is the bunch current, R the transverse radius, $\zeta = z/Z$ the longitudinal coordinate along the bunch (starting from the edge) normalized by the bunch length Z and $h(\zeta)$ and $g(\zeta)$ the form factors given by

$$h(\zeta) = \sqrt{A + (1-\zeta)^2} - \sqrt{A + \zeta^2} + (2\zeta - 1) , \tag{4.6}$$

$$g(\zeta) = \frac{1-\zeta}{2\sqrt{A^2 + (1-\zeta)^2}} + \frac{\zeta}{2\sqrt{A^2 + \zeta^2}} , \tag{4.7}$$

with $A = R/(\gamma_{rel} Z)$. From Eqs. 4.4 and 4.5 it is evident that both E_z and E_r are proportional to the beam current and inversely proportional to the square of the beam radius. At the longitudinal center of the bunch E_z is zero (hence it affects mainly the tails of the bunch), while E_r reaches its maximum value, which is proportional to the distance from the beam axis (see Fig. 4.1). The longer and the more relativistic a bunch becomes (as Z and γ_{rel} increase), $h(\zeta) \to 0$ and $g(\zeta) \to 1$, therefore $E_z \to 0$ and E_r becomes independent of ζ.

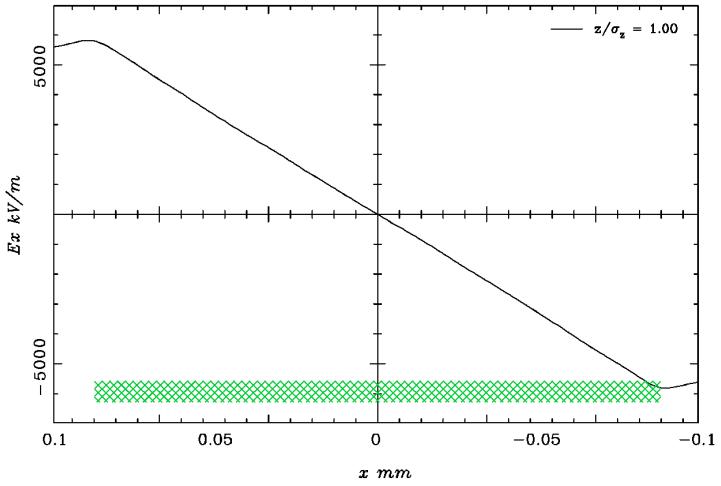

Figure 4.1: The horizontal electric component of the self fields in the lab frame with respect to the horizontal distance from the bunch axis from a mono-energetic bunch of 25 MeV with uniform charge distribution of 1 nC and longitudinal rms bunch length of 2 mm. The transverse bunch length is indicated with the green grid.

Except from the electric field, the beam current creates an azimuthal magnetic field around the axis of propagation which can be calculated using Maxwell's equations under cylindrical symmetry equal to $B_\theta = E_r \beta_{rel}/c$, where β_{rel} is the relativistic beta. This field creates a transverse focusing force, contrary to the defocusing force from the transverse electric field. The net transverse Lorentz force is then given by

$$F_r = q\left(E_r - \beta_{rel} c B_\theta\right) = qE_r\left(1 - \beta_{rel}^2\right) = qE_r/\gamma_{rel}^2\,, \tag{4.8}$$

where q is the charge of the particles. The last equation shows that as γ_{rel} increases, the induced magnetic field tends to cancel the effect of the electric

field, diminishing the net transverse force at higher energies. Overall, the strength of the transverse space-charge force is mainly determined by the energy and transverse size of the beam and to a less extent by its peak current. More details on this topic can be found in [19, 23].

A quantitative way to evaluate the significance of space charge over the emittance pressure in the beam dynamics is to calculate the *laminarity parameter* ρ [23]

$$\rho = \frac{I\sigma^2}{2I_0\beta_{rel}\gamma_{rel}\varepsilon_n^2}\,, \tag{4.9}$$

where I is the peak current of the beam, σ is the transverse rms size, I_0 the Alfven current of the particles ($I_0 \approx 17\,\text{kA}$ for electrons), $\beta_{rel}\gamma_{rel}$ the product of the relativistic factors and ε_n the transverse normalized rms emittance. When $\rho > 1$, the beam is considered as space-charge dominated, approaching a laminar flow mainly affected by the self fields as the ratio increases. When $\rho < 1$, the beam lies in an emittance-dominated, thermal regime, where the emittance pressure primarily determine the beam's motion. Table 4.1 shows the value of ρ for the optimized PITZ parameters at EMSY 1 for beams of 20 pC and 1 nC [48], an optimized 1 nC PST measurement using four projections, and the design European XFEL parameters at the exit of the first (BC 0) and the last (BC 2) compression stage [63].

	I [A]	σ [μm]	p_z [MeV/c]	ε_n [mm·mrad]	ρ
PITZ					
20 pC at EMSY 1	1	248	24	0.06	9.9
1 nC at EMSY 1	43	526	23	0.61	20.7
1 nC at PST.Scr2	43	162	23	0.61	2.0
European XFEL					
1 nC after BC 0	150	150	130	0.86	0.5
1 nC after BC 2	5000	37	2400	0.99	0.1

Table 4.1: Calculation of the laminarity parameter (ρ) for different beam parameters (description in the body of the text) and locations at PITZ and the European XFEL.

What might seem confusing is that, according to ρ, for a beam of given peak current, momentum and emittance, the smaller the transverse beam size, the smaller the significance of space charge — despite the stronger self-fields, as suggested by Eq. 4.5; however, this behaviour is explained by the

bigger dependence of the emittance term on the beam size in the envelope equation, as shown later in Section 5.1. As a result, ρ is not a suitable index for the absolute strength of the space-charge forces, but only relatively to the emittance pressure. Regarding the PST lattice at PITZ, its condensed beam optics push on the one hand towards an emittance-dominated transport, reducing ρ down to low values, on the other hand increase the space-charge forces and their impact on the accuracy of the measurement.

4.2 Linear self fields and equivalent rms behaviour

A straightforward way to include the effect of space charge in the beam dynamics would be to add the Lorentz force of the self fields in the equation of motion. However, this is extremely complicated to be calculated even by a computer, given the amount of particles found in typical beams. Alternatively, instead of trying to fully analyse these sophisticated interactions, there is a way to describe the average behaviour of a beam of certain conditions under space charge.

An equation which determines the space-charge dynamics of a stationary beam[2] is the *Vlasov* equation [64]. Kapchinsky and Vladimirsky (K-V) have derived a distribution that satisfies the Vlasov equation, the so-called *K-V distribution*, which consists of an elliptical cross section of uniform charge density and produces only linear self fields [65]. All the particles of this distribution are inside the trace-space area of $\epsilon = 4\varepsilon$, where ε is the geometrical rms emittance.

The K-V distribution proves to be very useful as it can be used to calculate the evolution of the rms quantities of any *equivalent* beam with elliptical symmetry. Two beams are considered to be equivalent, when they share the same (first- and) second-order statistical moments, i.e. the same 6-D rms values. In other words, the rms behaviour of a K-V beam can be generalized to the particles of any elliptical equivalent distribution within the K-V ellipse. This important property originates from the almost exclusive mutual dependence between the linear forces and the second moments of a beam, as described in [62, 66]. The major drawback of this approach is that it as-

[2] a beam that has reached an equilibrium state, with its particle distribution remaining unchanged along the propagation

sumes constant beam emittance or an a priori knowledge of the emittance evolution. As a matter of fact, it will be shown later that the assumption of constant emittance is met to a big extent along the PST section when the beam enters the lattice correctly matched.

A convenient way to correlate a particle distribution to its K-V equivalent is through the *effective emittance* ϵ and the *effective beam radius* R, defined as [66]

$$\epsilon_q = 4\varepsilon_q \,, \tag{4.10}$$

$$R_q = 2\sqrt{\langle q^2 \rangle} \,, \tag{4.11}$$

where q stands for x, y or z and ε is the rms emittance. Following the notation used in the beam envelope equations (Eqs. 2.29 and 2.30), $R_x = X$ and $R_y = Y$.

4.3 Simulation tools for linear and non-linear space-charge dynamics

As already mentioned, the exact effect of the space-charge force in its general form is practically impossible to be calculated with contemporary computers. As a result, the simulation codes used for the space charge analysis use a number of approximations and simplifications in order to perform in a reasonable time range using a reasonable amount of computing resources.

Currently the most realistic representation of space-charge dynamics is offered by the macroparticle-based codes. In this approach, the beam's particles are grouped in a much smaller number of macroparticles, each one of which carries the total charge of its components and is the source of the self fields. *A Space Charge Tracking Algorithm* (ASTRA) [67] offers such an implementation, where the macroparticles are allocated in a 2-D or 3-D grid whose cells are used for the calculation of Poisson's equation involving the Lorentz transformations. It is obvious that the bigger the number of macroparticles and grid cells, the more demanding the calculation becomes, especially for a 3-D mesh. ASTRA was used in this study typically with $5 \cdot 10^5$ macroparticles in a fine 3-D space-charge grid of $25\times25\times29$ cells for x, y and z respectively. The resolution of the grid was chosen such that the produced self fields are smooth functions along the beam dimensions and the average number of macroparticles per cell is sufficient.

Much faster implementations are available when the approximations described in Section 4.2 are acceptable. In this case, only the linear component of the self fields is calculated and its effect on the statistical moments of the beam is simulated. Such an implementation is offered by the V-Code software [68, 69], which calculates the evolution of the beam's moments by solving the Vlasov equation. It is important to notice that this approach foresees a constant emittance when no acceleration is applied to the beam. V-Code was used in this study for the linear space-charge tracking of the moments up to second order.

The range of applicability and accuracy of the second approach is of great interest, as it can provide incomparably faster results compared to the macroparticle-based solutions. Therefore, the performance of V-Code has been studied and compared to the reference non-linear space-charge tracking of ASTRA along the PST section.

4.4 Estimation of the space-charge effect in the tomographic reconstruction

As explained in Section 3.3, the quality of the tomographic trace-space reconstruction depends on the correct estimation of the beam dynamics along the PST lattice. When the self fields are not taken into account (*non-space-charge* or *zero-current* dynamics), the phase-space transformations are miscalculated, resulting in an incorrect reconstruction of the captured projections. In order to estimate this error, the PST measurement procedure was simulated with and without the consideration of space charge in the tomographic reconstruction. More specifically, the projections of an initially matched simulated beam along the four-screen PST lattice were reconstructed with the MENT algorithm, using the transfer matrices which correspond to different self fields: none, linear and non-linear.

4.4.1 Simulation walk-through

In order to generate a characteristic photo-injector trace-space distribution, ASTRA was used to provide a 22 ps FWHM long flat-top bunch of 1 nC charge, 24.7 MeV/c longitudinal momentum and emittance value equal to the result of a past slit-scan measurement at EMSY 1. This distribution

was further tracked up to PST.Scr 2, which is the entrance of the PST lattice and the point of reconstruction, using a focusing scheme that provides the design zero-current C-S parameters of the measurement for four projections given in Table 3.1. The resulting trace-space distribution is shown in Fig. 4.2a and 4.3a for the horizontal and vertical planes respectively. It is important for the interpretation of the simulation results to notice the emittance difference between the two phase planes: since $\varepsilon_x = 1.080\,\text{mm·mrad}$ and $\varepsilon_y = 3.321\,\text{mm·mrad}$, the requirement of $\beta_x = \beta_y = 0.999\,\text{m}$ yields from Eq. 2.31 that $\sigma_x = 0.150\,\text{mm}$ and $\sigma_y = 0.262\,\text{mm}$, indicating a higher charge density and thus enhanced self fields in the horizontal plane.

The strength of the PST quadrupoles was also set according to the matching solution of MAD for four projection screens, without any space-charge compensation (Table 3.1). Under this focusing, horizontal and vertical spatial projections of the generated bunch at each projection screen were acquired from the ASTRA tracking, while applying the binning of the PST cameras.

The reconstruction of the above projections under different space-charge treatments (no self fields, linear self fields, non-linear self fields) requires the respective transformation matrices for each case. Given the incoming beam and the PST quadrupole strengths, the beam transport can be simulated along the PST lattice and thus the evolution of the C-S parameters (α_q, β_q) and the phase advance ϕ_q for q=$\{x, y\}$ can be calculated from Eqs. 2.33, 2.31 and 2.10 for each tracking approach. Using Eq. 2.35, the transfer matrices at each projection screen can then be obtained for each space-charge treatment. For the description of the incoming beam, ASTRA requires the full particle distribution, while for V-Code just the second-order moments were provided with zero coupling terms.

The acquired projections from the ASTRA tracking can then be reconstructed for each space-charge case with the corresponding transfer matrices, allowing the comparison of each reconstructed distribution with the original input beam at PST.Scr 2. It is expected that the reconstruction of such complicated distributions from a small number of projections with limited binning will smear out the fine details observed in the original ones, therefore some quantitative properties are needed for the comparison. The normalized rms emittance (Eqs. 2.27 and 2.26) and the orientation angle (Eq. 2.13) of the reconstructed distribution will serve this purpose in order to judge on the area and the alignment of the trace space respectively.

The effect of space charge on the beam dynamics will be evaluated using the *phase-advance mismatch* $\Delta\phi$, defined as the difference between the

actual phase advance ϕ and the target phase advance ϕ^t. This value will be calculated at the location of each projection screen n after the entering one as:

$$\Delta\phi_n = \phi_n - \phi_n^t \,, \tag{4.12}$$

where $n = 2, 3, 4$ for PST.Scr3, PST.Scr4 and PST.Scr5 respectively and $\phi_n^t = (n-1) \cdot 45^\circ$ for both transverse planes. The phase-advance mismatch will be used to quantify the betatron phase shift which is induced by the space-charge defocusing and to indicate the projection angle mismatch at each screen when reconstructing in the normalized trace space. As a side effect, the influence of the quadrupole fringe fields will also be indicated in the absence of space charge, since their effect is simulated by the tracking codes and not by MAD.

4.4.2 Simulation results

Table 4.2 summarizes the phase-advance mismatch for each transverse plane and tracking approach for the n^{th} projection screen. The observed mismatches up to 5.9° when space charge is absent are due to the quadrupole fringe fields which are taken into account during the tracking but not in the matching procedure by MAD. For both space-charge treatments and transverse planes, the phase-advance mismatch is increasing along the PST lattice, as expected by the integrating defocusing force of the self fields. The increase rate of $\Delta\phi_n$ is higher for the x plane, which is consistent with the bigger space-charge density in this plane. The difference between the two space-charge approaches is less than 2°.

The main point from these results is that when space charge is neglected, an error is introduced to the trace-space transformation which is considered for the reconstruction of each projection. This error expressed in terms of phase advance reaches a maximum of $-5.9^\circ - (-30.9)^\circ = 25^\circ$ at the last projection screen. With the developed technique, the correct beam dynamics will be considered and thus the correct transfer matrices will be used for the reconstruction. Nevertheless, the available projections are still not optimized according to Subsection 3.3.1, i.e. they are not captured at the equidistant phase advance values ϕ_n^t. Therefore, a correct reconstruction of non-equally transformed projections is expected at this stage, offering an opportunity to judge the efficiency of the MENT algorithm under such mismatches. A fast method to diminish these mismatches is going to be presented in Chapter 5.

	$\Delta\phi$ **at screen:**		
	#2	**#3**	**#4**
***x* plane**			
No space charge	-0.7°	-3.2°	-5.9°
Linear space charge	-2.6°	-14.3°	-29.3°
Non-linear space charge	-1.9°	-14.8°	-30.9°
***y* plane**			
No space charge	-0.2°	-2.0°	-4.8°
Linear space charge	-2.0°	-9.9°	-19.2°
Non-linear space charge	-1.7°	-10.3°	-20.0°

Table 4.2: Evolution of the phase-advance mismatch along the projection screens for each plane and space-charge tracking approach.

Most of the observations from the evaluation of the phase-advance mismatch are reflected in the reconstructed distributions, presented in Fig. 4.2b, 4.2c and 4.2d for the horizontal plane and 4.3b, 4.3c and 4.3d for the vertical plane under each space-charge approach. The reconstructed normalized rms emittance for each case is summarized in Table 4.3 together with the relative error w.r.t. the original emittance for each phase plane.

	Normalized emittance [mm·mrad] **Relative error w.r.t. the original (%)**	
Original	1.080 (-)	3.321 (-)
Reconstruction without space charge	1.284 (+18.9%)	3.588 (+8.0%)
Reconstruction with linear space charge	1.068 (-1.1%)	3.229 (-2.8%)
Reconstruction with non-linear space charge	1.049 (-2.9%)	3.225 (-2.9%)
	***x* plane**	***y* plane**

Table 4.3: Normalized rms emittance values of the reconstructed distributions and relative error w.r.t. the original value.

A significant error of up to 18.9% is introduced when space charge is neglected. The deviation is considerably bigger for the horizontal plane com-

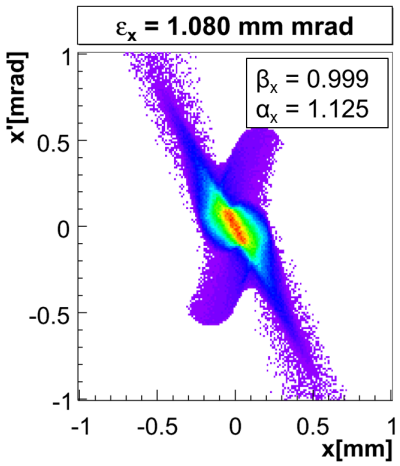

(a) Original distribution.

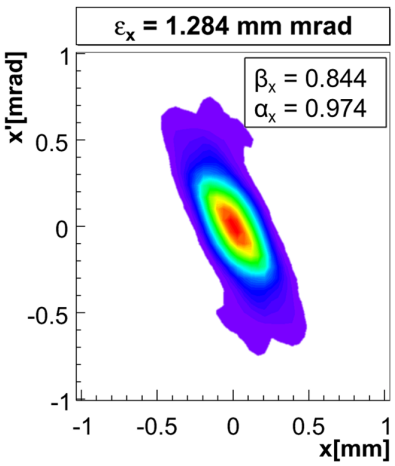

(b) Reconstructed distribution **without** space charge.

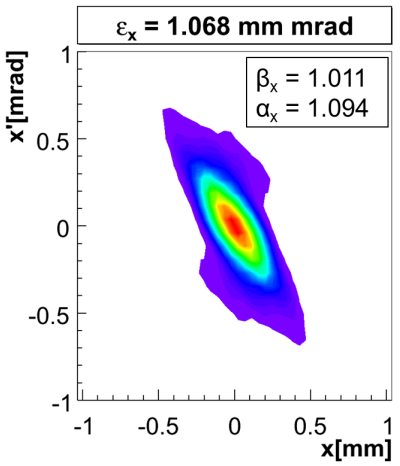

(c) Reconstructed distribution with **linear** space charge.

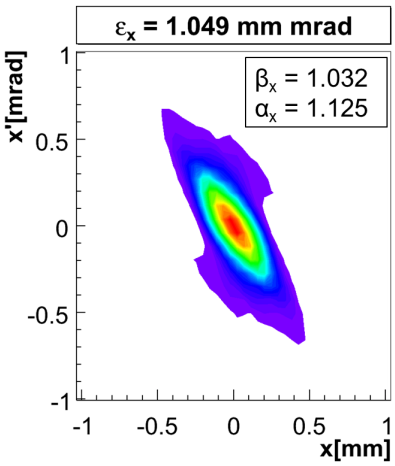

(d) Reconstructed distribution with **non-linear** space charge.

Figure 4.2: Horizontal trace space of the original beam (simulated with the ASTRA code) and its reconstruction under different space-charge treatments, with the corresponding normalized rms emittance and C-S parameters. The colour code represents normalized charge density for each plot (maximum is red, minimum is violet).

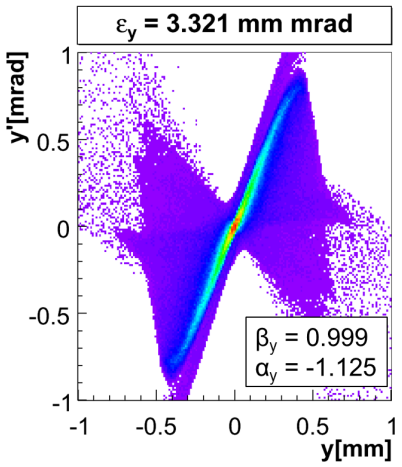

(a) Original distribution.

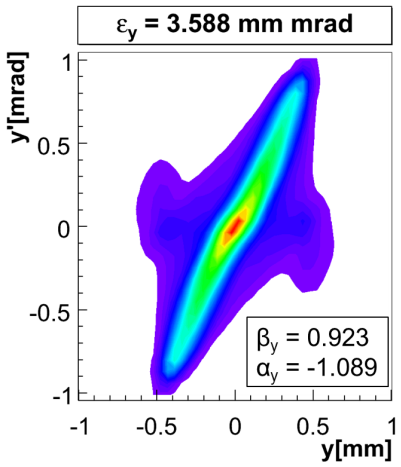

(b) Reconstructed distribution **without** space charge.

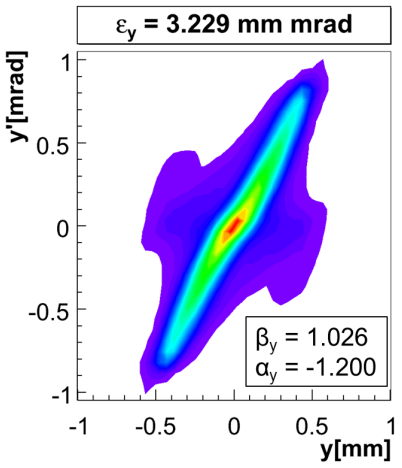

(c) Reconstructed distribution with **linear** space charge.

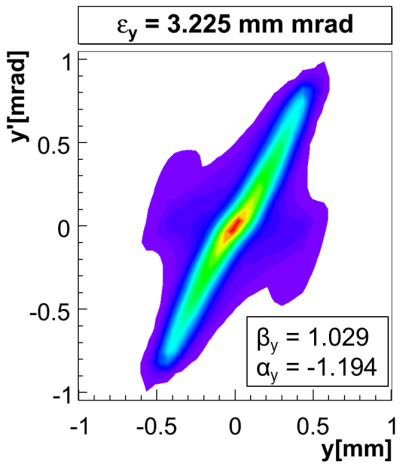

(d) Reconstructed distribution with **non-linear** space charge.

Figure 4.3: Vertical trace space of the original beam (simulated with the ASTRA code) and its reconstruction under different space-charge treatments, with the corresponding normalized rms emittance and C-S parameters. The colour code represents normalized charge density for each plot (maximum is red, minimum is violet).

pared to the vertical as expected from the bigger charge density. On the other side, any tracking which considers space charge matches the reconstructed emittance within 3%. The emittance difference between the two space-charge implementations is smaller than 2%.

The relative error of the orientation angle of the distributions is summarized in Table 4.4. The results follow a similar trend as the emittance values. The shearing which appears in the zero-current reconstruction gets suppressed with the space-charge analysis.

	Relative error in orientation (%)	
Reconstruction without space charge	-12.4%	-6.8%
Reconstruction with linear space charge	+2.4%	+0.0%
Reconstruction with non-linear space charge	+3.4%	+0.6%
	***x* plane**	***y* plane**

Table 4.4: Relative error of the orientation angle of the reconstructed distributions w.r.t. the original value.

Despite the extra assumptions considered by V-Code (linearity of the fields, constant emittance, zero coupling and higher-order terms, etc.), the results from the linear space-charge reconstruction counter-intuitively match better the original values than the ones from the general space-charge tracking. However, this observation does not prove that the linear space-charge tracking is more accurate; a closer look on the evolution of the emittance along the PST lattice as calculated by ASTRA (Fig. 4.4) indicates a deviation from the initial value up to 11% for the horizontal and 8% for the vertical plane [3]. This emittance variation is due to the longitudinal inhomogeneity of the bunch and is going to be explained in Chapter 6. The practical consequence is that the four projections are captured at different emittance values, therefore the emittance of the reconstructed distribution is expected to be closer to the average of the four contributions, which is 1.034 mm·mrad for the horizontal and 3.229 mm·mrad for the vertical plane.

[3] the observed peaks correspond to the known feature of the emittance calculation within quadrupoles by ASTRA [67] and therefore are not taken into account

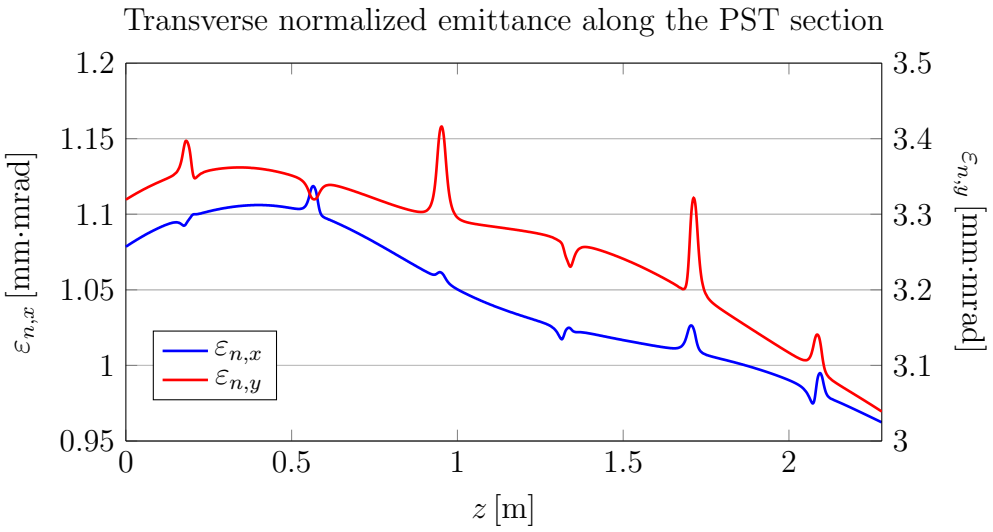

Figure 4.4: Evolution of the transverse normalized emittance along the PST section (starting from PST.Scr 2) for the horizontal (blue line, left axis) and the vertical plane (red line, right axis), as simulated by ASTRA.

Consequently, the comparison of the reconstructed emittance values to the average emittance of the captured projections, given in Table 4.5, reveals the performance of each tracking approach in a more representative way. The linear space-charge reconstruction now yields a bigger error than the non-linear one, as expected. Nonetheless, the two approaches are still very close to each other, with the linear method being able to correct the average reconstructed emittance by more than 20%. An additional conclusion from these results is the good performance of the MENT algorithm under the considerable phase-advance mismatches described in Table 4.2 (1.5% error in the average emittance of the horizontal plane for additive mismatches up to 30.9°).

According to the concept of equivalent beams described in Section 4.2, the evolution of the second-order moments is practically independent of the exact form of the particle distribution for beams of equal rms values. This statement is indeed verified when using a software-generated beam of uniform and gaussian transverse profile respectively with the same rms moments and zero coupling terms as input for ASTRA. The phase-advance mismatch for each case which is presented in Table 4.6 shows very good agreement between

	Normalized emittance [mm·mrad] **Relative error w.r.t. the average (%)**	
Average among the four projection screens	1.034 (-)	3.229 (-)
Reconstruction without space charge	1.284 (+24.2%)	3.588 (+11.1%)
Reconstruction with linear space charge	1.068 (+3.3%)	3.229 (+0.0%)
Reconstruction with non-linear space charge	1.049 (+1.5%)	3.225 (-0.1%)
	***x* plane**	***y* plane**

Table 4.5: Normalized rms emittance values of the reconstructed distributions and relative error w.r.t. the average emittance among the four projection screens.

the two profiles and only small differences (up to 2.5°) compared to the results from the original distribution (non-linear space charge tracking in Table 4.2). Overall the transport of the three different distributions in ASTRA is well represented by the linear transport of the equivalent beam in V-Code, with a maximum difference of $-19.2° - (-22.5)° = 3.3°$, which hardly influences the reconstruction result.

	$\Delta\phi$ at screen:		
	#2	**#3**	**#4**
***x* plane**			
Uniform profile	-2.9°	-14.5°	-29.9°
Gaussian profile	-2.8°	-14.0°	-29.2°
***y* plane**			
Uniform profile	-3.5°	-12.7°	-22.5°
Gaussian profile	-3.4°	-12.4°	-22.1°

Table 4.6: Evolution of the phase-advance mismatch along the projection screens for each plane for a beam of uniform and gaussian transverse profile.

The derived results underline the dominance of the linear forces in the beam dynamics along the PST lattice, suggesting that the transverse emittance stays fairly constant in this section. This statement might seem con-

tradicting to Fig. 4.4 and the already discussed variation of the emittance. However, this variation can be explained by a mechanism known as correlated emittance oscillations, which is going to be covered in Chapter 6, and does not interfere with the analysis made so far. These oscillations will be considerably smaller when the incoming beam is more homogeneous, as shown in Fig. 4.5 for the case of the software-generated beam of uniform transverse profile used in the calculations above.

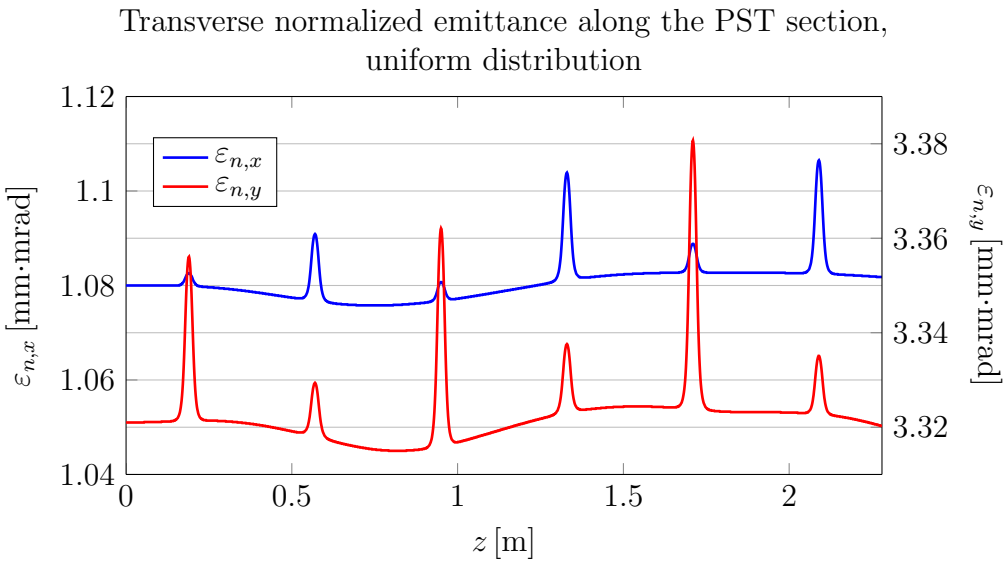

Figure 4.5: Evolution of the transverse normalized emittance of a longitudinally and transversely uniform distribution along the PST section (starting from PST.Scr 2) for the horizontal (blue line, left axis) and the vertical plane (red line, right axis).

The final outcome of these simulations is that along the PST section the linear space-charge tracking gives very similar results to the macroparticle tracking in terms of rms beam dynamics and final reconstruction results, but incomparably faster (seconds instead of hours). Consequently, the linear approach can be used to efficiently incorporate the effect of space charge in the tomographic reconstruction, reducing significantly the error from the neglect of the self fields. A side consequence is that the effect of potentially mismatched entering C-S parameters as well as the fringe fields are also taken into account. Despite these additive mismatches which lead to a significant

deviation from the design beam dynamics of the measurement, the reconstruction error introduced by the MENT algorithm proves to be fairly small. The application of this technique in measured data is demonstrated in the following section.

4.5 Including the effect of space charge in the tomographic reconstruction at PITZ

According to the developed analysis it is now possible to include the space-charge effect in the transformation of the beam's trace space along the PST lattice and thus to the tomographic reconstruction. In order to do so, a description of the incoming beam parameters is required in addition to the applied quadrupole strengths. Since these values are not known in advance —on the contrary, the ultimate purpose is to measure them— some realistic assumption has to be made.

At PITZ a rough estimation of the transverse second-order moments of the beam is offered by the tomographic reconstruction, when space charge is neglected. For better precision, a refinement of these input parameters can be applied after a space-charge reconstruction. The convergence to a final value, which usually happens after one iteration, justifies the validity of this assumption. In this way, the error from the assumption of a perfectly matched beam at the PST entrance is diminished. For the longitudinal plane, the values can be provided by a longitudinal phase-space measurement [5] or by just using the result from a bunch length estimation measurement [47], assuming zero divergence and covariance for beams of small energy spread.

This technique was applied to both early and recent measurements of the tomography module at PITZ. V-Code was used to extract the average space-charge dynamics of the moments up to second order.

4.5.1 Measurements with 1nC bunch charge

First measurement period (2011)

A four-projection measurement of a beam with the parameters used in Section 4.4 (1 nC charge, 24.7 MeV/c momentum and 22 ps FWHM flat-top length) from the measurement period of 2011 was re-analysed using the non-space-charge reconstruction result and the estimated longitudinal pa-

rameters from ASTRA for the description of the input beam. The reconstruction result is presented in Fig. 4.6, without and with the consideration of space charge. The beam projections were captured with the binned camera resolution, yielding a statistical error of the measured emittance equal to $\pm 0.15\,\mathrm{mm{\cdot}mrad}$ for the horizontal and $\pm 0.19\,\mathrm{mm{\cdot}mrad}$ for the vertical plane.

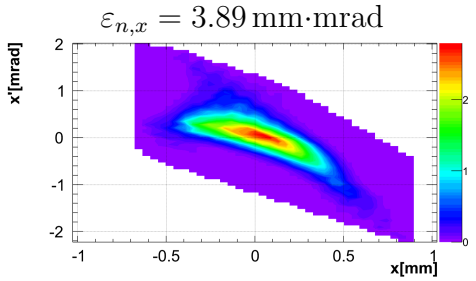

(a) Zero-current reconstruction of the horizontal plane.

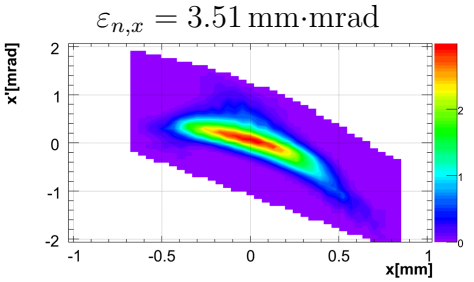

(b) Linear space-charge reconstruction of the horizontal plane.

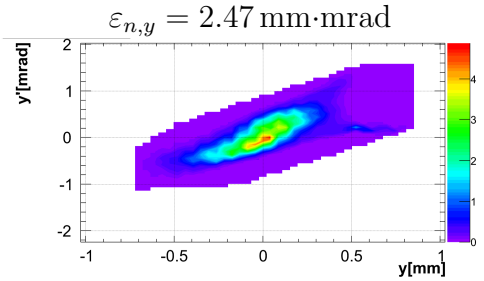

(c) Zero-current reconstruction of the vertical plane.

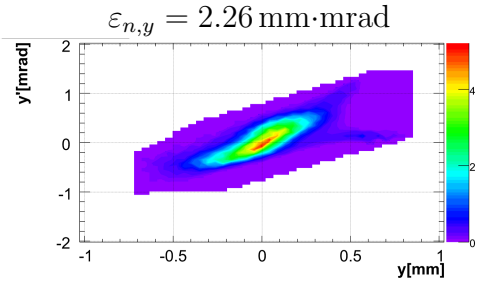

(d) Linear space-charge reconstruction of the vertical plane.

Figure 4.6: Reconstruction of an early 1 nC PST measurement without vs. with space-charge consideration.

A comparison of the reconstructed distributions shows smoother lines and less pronounced artefacts around the beam core when space charge is taken into consideration. The calculated normalized emittance drops by $\sim 10\,\%$ for both planes, in agreement with the simulation result for the vertical distribution in Subsection 4.4.2 which had similar rms beam size (reconstructed beam size for both transverse planes $\sim 0.250\,\mathrm{mm}$).

Latest measurement period (2014)

New PST measurements were taken in 2014 at PITZ with smaller accelerating gradients and not optimized machine parameters, due to lack of available operation time. The reconstruction of a beam with 1 nC charge and 22.0 MeV/c momentum is shown in Fig. 4.7, without and with the consideration of space charge.

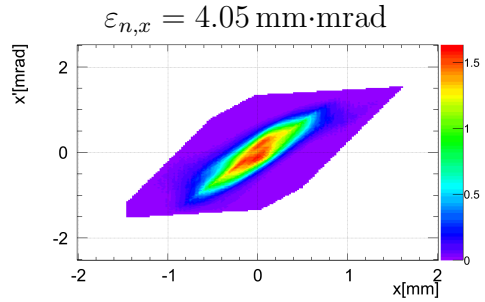

(a) Zero-current reconstruction of the horizontal plane.

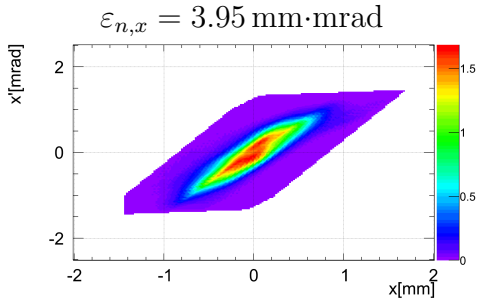

(b) Linear space-charge reconstruction of the horizontal plane.

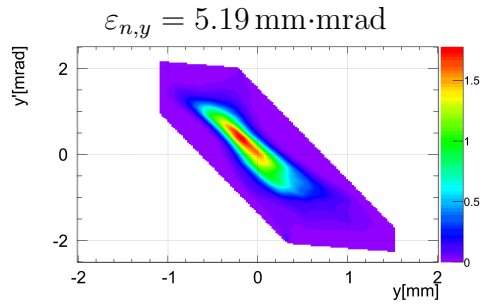

(c) Zero-current reconstruction of the vertical plane.

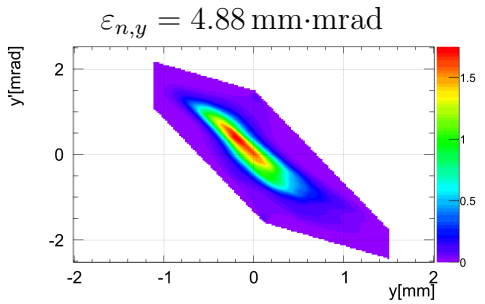

(d) Linear space-charge reconstruction of the vertical plane.

Figure 4.7: Reconstruction of a recent 1 nC PST measurement without vs. with space-charge consideration.

The projection data were acquired with the full camera resolution, reducing the statistical error of the measurement down to ±0.03 mm·mrad for the horizontal and ±0.02 mm·mrad for the vertical plane. For the space-charge calculations, the rms bunch length was estimated with the technique described in [47] to be 2.1 mm, in accordance with the ASTRA simulation. Despite the lower momentum, the big beam size (as a result of the big emittance) did not result in strong self fields. The normalized emittance reduces

by just 3% for the horizontal plane ($\sigma_x = 0.391\,\mathrm{mm}$) and by 6% for the vertical plane ($\sigma_y = 0.360\,\mathrm{mm}$) after the space-charge treatment.

4.5.2 Measurements with 100pC bunch charge

Measurements were also performed for a bunch charge of 100 pC at almost the same momentum (22.1 MeV/c). The reconstruction of such a measurement is shown in Fig. 4.8, without and with the consideration of the self fields. With a bunch length estimation measurement of 1.5 mm rms using [47], the emittance reduces by about 5% for both transverse planes ($\sigma_{x,y} \approx 0.220\,\mathrm{mm}$) after the space-charge treatment. The statistical error is $\pm 0.11\,\mathrm{mm{\cdot}mrad}$ for the horizontal and $\pm 0.13\,\mathrm{mm{\cdot}mrad}$ for the vertical plane.

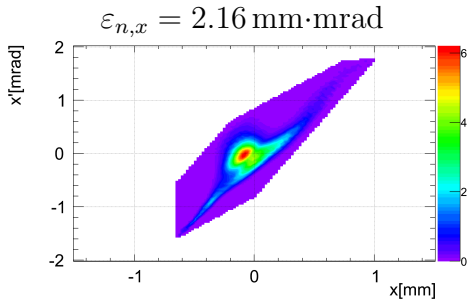

(a) Zero-current reconstruction of the horizontal plane.

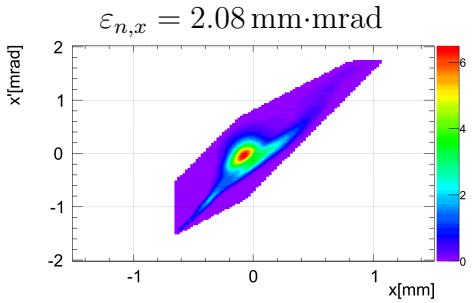

(b) Linear space-charge reconstruction of the horizontal plane.

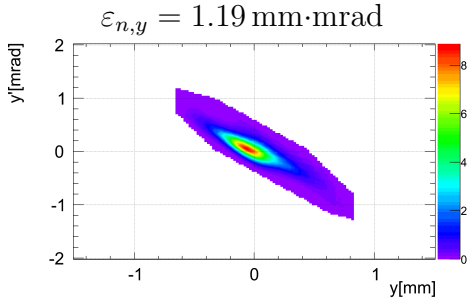

(c) Zero-current reconstruction of the vertical plane.

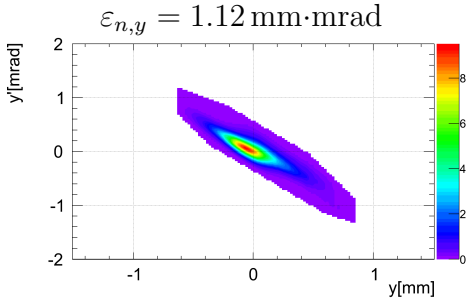

(d) Linear space-charge reconstruction of the vertical plane.

Figure 4.8: Reconstruction of a 100 pC PST measurement without vs. with space-charge consideration.

Judging on the results, it is fair to claim that the effect of the self fields

for such low space-charge densities becomes comparable with the statistical uncertainty. Nonetheless, this remark is not expected to be valid in the case of optimized measurement conditions and smaller beam emittance delivered at the PST section.

4.5.3 Measurements with 20pC bunch charge

The commissioning of the full camera resolution during the data acquisition allowed PST measurements of 20 pC charge bunches for the first time at PITZ. The reconstruction of the trace space of such a beam at 22.1 MeV/c is presented in Fig. 4.9.

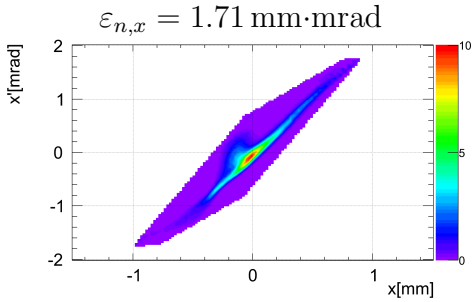

(a) Zero-current reconstruction of the horizontal plane.

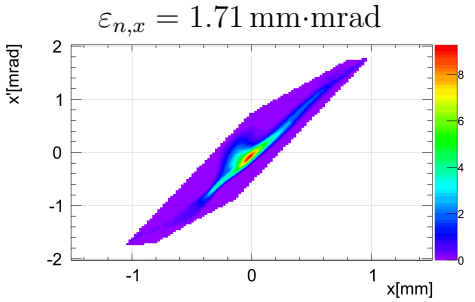

(b) Linear space-charge reconstruction of the horizontal plane.

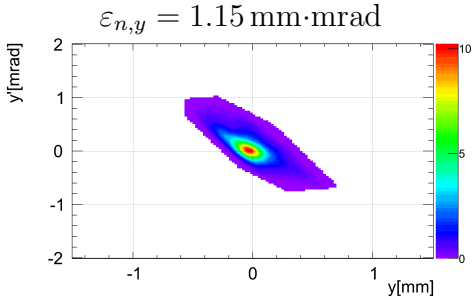

(c) Zero-current reconstruction of the vertical plane.

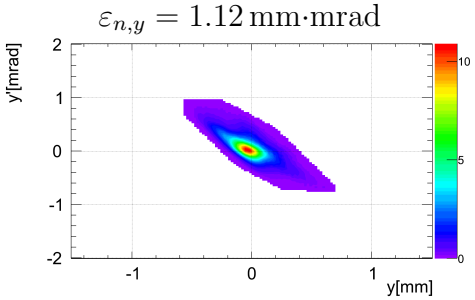

(d) Linear space-charge reconstruction of the vertical plane.

Figure 4.9: Reconstruction of a 20 pC PST measurement without vs. with space-charge consideration.

The beam size on the horizontal plane ($\sigma_x = 0.261$ mm) was too big to produce significant self fields, while on the vertical plane the smaller beam

size ($\sigma_x = 0.164\,\mathrm{mm}$) causes a reduction of 3% to the vertical emittance. The statistical error is $\pm 0.23\,\mathrm{mm{\cdot}mrad}$ for the horizontal and $\pm 0.15\,\mathrm{mm{\cdot}mrad}$ for the vertical plane. As in the case of 100 pC, the high emittance delivered by the matching section creates a very low space-charge density, which is less significant than the increased statistical uncertainty due to the machine conditions during the measurement.

4.5.4 Measurements using five projection screens

The analysis carried out in Subsection 4.4.2 can also be extended in a straightforward way to include an additional projection screen. Since a bigger entering β-function and thus bigger beam size is required for this case (consult Table 3.1), space charge is expected to have a weaker effect. Moreover, the additional projection is expected to improve the quality of the reconstruction.

During the last measurement period at PITZ, the five-projection PST measurement was commissioned for the first time and used for 1 nC bunch charges. As it is going to be explained in Chapter 6, the available focusing strength in the matching section was not sufficient to get a correctly matched beam with all the slices aligned for a constant emittance evolution along the PST lattice. Nevertheless, the addition of the 5$^{\mathrm{th}}$ screen was able to indicate this misalignment, as shown in Fig. 4.10. A double-beam structure is observed in the reconstruction of the horizontal trace space and a star-shaped halo structure in the vertical, with a statistical error of $\pm 0.06\,\mathrm{mm{\cdot}mrad}$ and $\pm 0.15\,\mathrm{mm{\cdot}mrad}$ respectively.

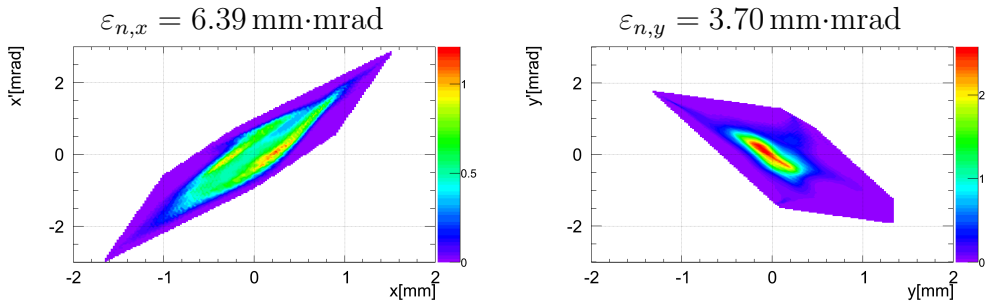

(a) Reconstruction of the horizontal trace space.

(b) Reconstruction of the vertical trace space.

Figure 4.10: Reconstruction of a 1 nC PST measurement with space-charge consideration using five projection screens.

4.6 Application to ALICE

The developed technique was also applied with success to the Accelerator and Lasers In Combined Experiments (ALICE) facility at the Daresbury Laboratory [56]. ALICE is an electron accelerator and facilitates a tomography section for the reconstruction of the transverse normalized trace space (schematic layout in Fig. 4.11). The tomographic measurement can be performed using either 3 projection screens and fixed optics in between (similarly to PITZ) or a single screen and a quadrupole with varying strength upstream, as in the quad-scan technique.

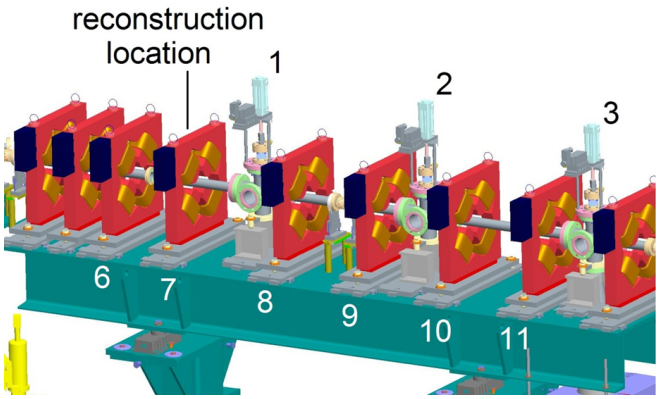

Figure 4.11: ALICE tomography section. The three projection screens are indicated by the numbers on top and the quadrupole magnets by the numbers on the bottom. Image courtesy: K.M. Hock.

The latter approach was used to reconstruct the horizontal normalized trace space of electron bunches with 12.5 MeV/c longitudinal momentum, 80 pC charge, 1.2 mm rms length and 0.265 mm rms transverse radius at the location of quadrupole #7. Two separate measurements with different drift lengths were performed, one using screen #1 for capturing the projections and quadrupole #7 for scanning the focusing strength, and another using screen #3 with quadrupole #10 instead. While zero-current dynamics and hard-edge optics would result in identical reconstructions from both measurements, a rotation of $\sim 22°$ was observed between the two distributions (Fig. 4.12).

In order to estimate the effect of space charge and fringe fields in these measurements, the technique developed for PITZ was applied to the involved

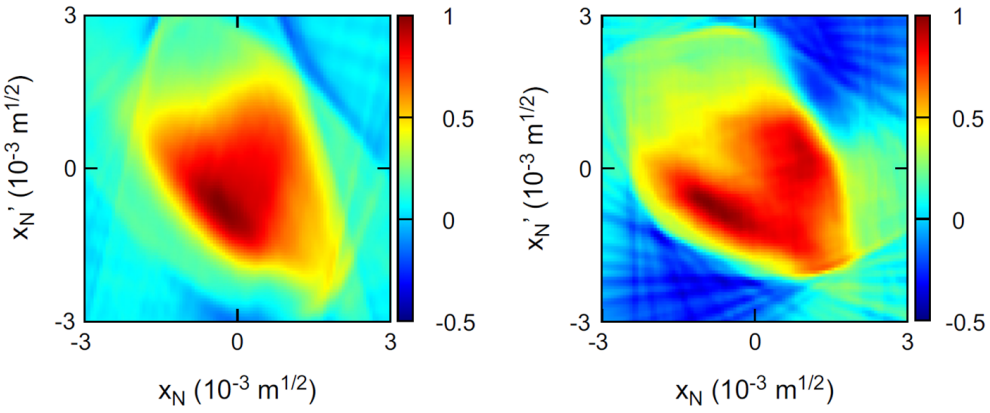

Figure 4.12: Reconstruction of the horizontal normalized trace space at the location of quadrupole #7 in the tomography section of ALICE using quadrupole #7 with screen #1 (left) and quadrupole #10 with screen #3 (right). Image courtesy: K.M. Hock.

beam dynamics. In terms of phase-advance mismatch, the effect of the self and fringe fields was calculated to be 2.3° and 1.8° respectively for the first dataset and 9.6° and 9.5° respectively for the second dataset. When combining the two effects, the phase-advance difference between the two datasets was able to justify $\sim$70% of the observed rotation. Known magnet issues (calibration, hysteresis, etc.) are considered responsible for the remaining difference. The complete results of these simulations can be found in [12].

The results from ALICE prove the applicability of the developed technique to other facilities that use different beam parameters (momentum, charge and dimensions). Additionally, it is an indication that this analysis is not restricted to the tomographic reconstruction, but can also be integrated in other measurement methods such as the quadrupole-scan and the multi-screen emittance measurement.

Chapter 5

Space-charge matching of the PST section

While in the previous chapter the effect of space charge has been included in the tomographic reconstruction, the beam optics involved in the data acquisition have not been adjusted to match the design beam dynamics, introducing small errors in the reconstructed distribution. In order to provide a homogeneously distributed sampling of the beam in the trace space and thus optimal input data to the tomographic measurement, a matching procedure which compensates the defocusing of the self fields is required. Towards this goal, this chapter presents a theory which, under certain conditions, correlates the beam parameters in the absence of self fields with their space-charge equivalents. Following this approach, a fast matching method for beams with space charge is suggested, using existing matching codes which neglect the self fields. The performance of this method is evaluated for beams of different space-charge density along the PST section at PITZ.

5.1 Smooth-approximation theory

The behaviour of a beam with uniform charge distribution in a uniform focusing channel has been studied extensively by M. Reiser [19] and is going to be summarized in the next paragraphs. For such a system, where a constant external focusing strength $\kappa_0 = k_0^2$ and no acceleration is being applied to a long round beam, the 1-D envelope equation (Eq. 2.28) takes the following

form:

$$R'' + k_0^2 R - \frac{K}{R} - \frac{\epsilon^2}{R^3} = 0\,, \tag{5.1}$$

where R is the (effective) beam radius, ϵ is the effective emittance (defined in Section 4.2) and K is the *generalized perveance*, defined (in the absence of neutralizing particles) as

$$K = 2\frac{I}{I_0 \beta_{rel}^3 \gamma_{rel}^3}\,, \tag{5.2}$$

where I is the peak current of the beam, I_0 the Alfven current and $\beta_{rel}\gamma_{rel}$ the relativistic factors. Eq. 5.1 is derived for continuous beams and thus applies to the major part of a relatively long bunch, except the tails. The peak current I can be approximated by the total charge over the laser pulse duration for photo-injectors like PITZ, while I_0 is a constant of the particle species and is approximately 17 kA for electrons. Compared to Eq. 2.28, Eq. 5.1 includes the space charge defocusing term $-K/R$ in addition to the external focusing and the emittance pressure terms.

A special solution of Eq. 5.1 can be found so that the beam radius stays constant. This solution is referred as the *matched beam* and is described by the following equation:

$$ka^2 = \epsilon\,, \tag{5.3}$$

where a is the matched beam radius and k is the *wave number* of the particle's oscillations when space charge is included [19]. The contribution of the external focusing k_0, which is also the wave number when space charge is negligible, is connected with k via

$$k = \sqrt{k_0^2 - \frac{K}{a^2}}\,. \tag{5.4}$$

In other words, a beam of generalized perveance K and emittance ϵ will conserve a constant radius $R = a$ when passing through a channel of constant focusing k_0. An additional requirement for this condition is a zero slope of the beam radius at the entrance of the channel, or $R' = 0$.

Instead of uniform focusing channels, periodic focusing lattices are used in practice. In that case, the radius of a matched beam does not stay constant, but undergoes periodic oscillations with the period of the lattice S:

$$R(z) = \overline{R}\,[1 + \delta(z)] = R(z + S)\,, \tag{5.5}$$

where $\overline{R}$ is the mean value of the radius over one lattice period and $\delta(z)$ the modulation around the mean value due to the non-uniformity of the focusing, with $\int_z^{z+S} \delta(z)\mathrm{d}z = 0$. When the amplitude of these oscillations is small compared to the mean value ($|\delta_0(z)| \ll 1$), then the analysis for the uniform channel can be applied to the respective mean values of the periodic system. This is referred as the *smooth-approximation theory* and is applied to solenoid lattices as well as quadrupole lattices when two planes of symmetry are considered.

Under this approximation, the matched beam radius a in Eq. 5.3 corresponds to $\overline{R}$, which is connected to the effective emittance by the mean beta-function $\overline{\beta}$ through [19]

$$\overline{R} = \sqrt{\epsilon\overline{\beta}}\,. \tag{5.6}$$

For the above quantities, a *non-space-charge* or *zero-current* component can be defined, which describes their behaviour in the absence of space charge ($K = 0$):

$$R_0(z) = \overline{R_0}\,[1 + \delta_0(z)]\ , \tag{5.7}$$

$$\overline{R_0} = \sqrt{\epsilon\overline{\beta_0}}\,, \tag{5.8}$$

where the subscript 0 indicates the respective zero-current equivalent and $\delta_0(z) = \delta(z)$ to a very good approximation under the described assumptions [19]. Likewise, the wave numbers k and k_0 are then calculated from Eqs. 5.3, 5.6 and 5.8 to be:

$$k = \frac{1}{\overline{\beta}}\,, \tag{5.9}$$

$$k_0 = \frac{1}{\overline{\beta_0}}\,. \tag{5.10}$$

with k_0 being approximated in terms of focusing strength by [19]:

$$k_0^2 = \overline{\kappa_0} + \frac{1}{S}\int_z^{z+S} \kappa_0(z)\delta_0(z)\mathrm{d}z\,. \tag{5.11}$$

The wave numbers are found to be closely connected to the phase advance per lattice period ψ. From Eqs. 2.10 and 5.9 one gets:

$$\psi = \int_z^{z+S} \frac{1}{\overline{\beta}}\,\mathrm{d}z = \frac{S}{\overline{\beta}} = Sk \tag{5.12}$$

and likewise

$$\psi_0 = Sk_0\,. \tag{5.13}$$

In order to associate the space-charge values with their zero-current equivalents, the dimensionless parameter u is introduced [19]:

$$u = \frac{K}{2k_0\epsilon}\,, \tag{5.14}$$

which from a combination of Eqs. 5.4, 5.6, 5.9 and 5.10 gives for round beams:

$$\overline{\beta} = \overline{\beta_0}\left(u + \sqrt{u^2+1}\right) \tag{5.15}$$

and with the help of Eqs. 5.12 and 5.13:

$$\psi = \psi_0\left(\sqrt{u^2+1} - u\right). \tag{5.16}$$

The factor u proves to be very useful: it can translate the mean β-function and phase advance per cell into the respective values when space charge would be absent. Using this feature, it is possible to predict the expected beam transport under the influence of linear self fields by performing a fast non-space-charge simulation of the corresponding zero-current parameters. Equivalently, a non-space-charge matching procedure which uses as constraints the zero-current beam parameters instead of the actual ones, can estimate the required focusing strength when linear self fields are present. The last point is going to be covered in more details in the next section.

It is also possible to extend this theory to focusing lattices with two planes of symmetry and non-round beams with elliptical symmetry. For such a beam with horizontal and vertical effective size of X and Y respectively, the beam envelope equation becomes [19]:

$$X'' + k_{0x}^2 X - \frac{2K}{X+Y} - \frac{\epsilon_x^2}{X^3} = 0 \tag{5.17}$$

$$Y'' + k_{0y}^2 Y - \frac{2K}{X+Y} - \frac{\epsilon_y^2}{Y^3} = 0\,. \tag{5.18}$$

For a FODO lattice even though $\overline{\kappa_{0q}} = 0$, the second term of k_{0q}^2 in Eq. 5.11 is not zero since $\delta_q(z)$ follows the sign of the focusing strength, i.e. $\delta_q(z) > 0$ where $\kappa_{0q} > 0$ (focusing magnet) and $\delta_q(z) < 0$ where $\kappa_{0q} < 0$ (defocusing magnet). Since $\delta_x(z) = -\delta_y(z)$ in quadrupole channels, $k_{0x}^2 = k_{0y}^2 = k_0^2$.

A comparison of Eqs. 5.17 and 5.18 with Eq. 5.1 shows that the only practical difference is that instead of R there is $(X+Y)/2$ on the third term. Unfortunately, this prevents a total decoupling of the two planes, as a matched solution of

$$k_q a_q^2 = \epsilon_q \,, \tag{5.19}$$

would lead to

$$k_q = \sqrt{k_0^2 - \frac{2K}{a_q(a_x+a_y)}} \,, \tag{5.20}$$

$$\overline{\beta_q} = \overline{\beta_0}\left(u\frac{2a_q}{a_x+a_y} + \sqrt{\left(u\frac{2a_q}{a_x+a_y}\right)^2+1}\right) \,, \tag{5.21}$$

$$\psi_q = \psi_0\left(\sqrt{\left(u\frac{2a_q}{a_x+a_y}\right)^2+1} - u\frac{2a_q}{a_x+a_y}\right) \,, \tag{5.22}$$

where

$$\psi_q = Sk_q \,, \tag{5.23}$$

as shown in Appendix B. A consequence of Eqs. 5.23 and 5.20 is that a direct way of achieving $\psi_x = \psi_y$ is by having $a_x = a_y$ and thus from Eq. 5.19 $\epsilon_x = \epsilon_y$. In other words, a round beam of symmetric transverse emittance is needed in order to achieve the same phase advance for both transverse planes along a FODO cell according to the smooth-approximation theory.

Except from the aforementioned requirements (matched round beam of constant slope and emittance), the validity of the theory requires a zero-current phase advance per cell less than 90° ($\psi_0 \leq \pi/2\,\mathrm{rad}$) in order to avoid big amplitude oscillations and a sufficiently low $\overline{R}/S$ ratio to avoid nonlinearities [19]. These conditions are met to a great extent along the PST section at PITZ:

- periodic FODO lattice with a period of $S = 0.76\,\mathrm{m}$
- the incoming beam is foreseen to be round (for a symmetric transverse emittance) and maintain a constant envelope along the lattice, according to the design dynamics (see Fig. 3.9)
- the emittance stays fairly constant and the linear fields dominate the beam dynamics, as shown in Chapter 4

- $\psi_0 < \pi/2\,\mathrm{rad}$ and $\overline{R} \ll S$ even for the most demanding beam parameters and tomography constraints.

For the calculations of the last point, Eqs. 5.16, 5.14, 5.13 and 5.12 can be combined to give the following equation (see Appendix B):

$$\psi_0 = S\sqrt{\frac{1}{\overline{\beta}^2} + \frac{K}{\epsilon\overline{\beta}}}\,, \tag{5.24}$$

which for $I = 50\,\mathrm{A}$ ($\sim 1\,\mathrm{nC}$), $I_0 = 17\,\mathrm{kA}$, $\beta_{rel}\gamma_{rel} = 43$ ($\sim 22\,\mathrm{MeV/c}$), $\epsilon_n = 4\,\mathrm{mm{\cdot}mrad}$ and $\overline{\beta} = 0.772\,\mathrm{m}$ for three projection screens gives $\psi_0 \approx 1.25\,\mathrm{rad}$ or $\sim 72^\circ$ and $\overline{R}/S \approx 0.5‰$ for the numbers listed above. Therefore, the smooth approximation theory can be used to interpret and control the space-charge dynamics at the PST section.

5.2 Space-charge compensated matching along the PST section

The smooth-approximation theory proves to be very helpful by offering a straightforward correlation between the zero-current and the linear space-charge beam dynamics, as long as the aforementioned conditions are met. This feature enables simulation codes that lack any space-charge consideration to indirectly include the linear self fields in their results, once an estimation of the space-charge density is available. The effectiveness of this approach is going to be tested on the matching functionality of MAD which, despite its superiority compared to other matching routines, neglects the space-charge defocusing. The ultimate goal of this approach is to eliminate the phase-advance mismatch which is delivered to the projection screens by the zero-current PST lattice (see Subsection 4.4.2) in order to achieve optimal reconstruction results.

5.2.1 Guidelines

According to the suggested approach, MAD should be operated with the corresponding zero-current beam parameters in order to get the correct matching result when the self fields are present. For the PST section, this means that the target value of the phase advance per FODO cell should not be ψ

(e.g. 45° for a 4-projection tomographic measurement), but the equivalent ψ_0 instead. Given the length of the FODO cell (S), this transformation is possible when an estimation of the generalized perveance (K) and transverse effective emittance (ϵ) of the beam is available, through the equation:

$$\psi_0 = \sqrt{\psi^2 + \frac{KS}{\epsilon}\psi}\,, \tag{5.25}$$

which is derived when combining Eqs. 5.24 and 5.12 (see Appendix B). While an estimation of the peak current and thus K is simple during an experimental measurement, the emittance value can be roughly estimated after a PST measurement[1] with zero-current matching, as presented in Section 4.5. Once ψ_0 is calculated, the factor u can also be derived through Eq. 5.16.

The outcome of the matching procedure is the required focusing strength k_0 together with the entering zero-current C-S parameters, β_0 and α_0. The actual beam parameters that apply to this transport are the corresponding β and α values. Eq. 5.15 can be used for the translation of β_0 to β, since they both represent the respective mean values of the periodic oscillation along the matched lattice. Likewise, the calculation of the entering α-function is given by:

$$\alpha = \alpha_0 \left(u + \sqrt{u^2+1}\right)\,, \tag{5.26}$$

as explained in Appendix B. A summary of the procedure that needs to be followed is schematically shown in Fig. 5.1.

5.2.2 Simulations

The efficiency of the smooth-approximation theory in compensating the self fields in the matching procedure can be estimated by the phase-advance mismatch (Eq. 4.12) it delivers at each projection screen. For this calculation, two cases with the beam parameters used in Section 4.4 (1 nC, 24.7 MeV/c, 22 ps) will be simulated, each one having a symmetric transverse normalized emittance of $\varepsilon_{n,x} = \varepsilon_{n,y} = 1.080$ and 3.321 mm·mrad respectively.

For each case, the zero-current phase advance per cell ψ_0 that corresponds to a ψ of 45° is given as a matching constraint to MAD. The matching result is used for the setting of the quadrupole strengths and the description input beam in V-Code. The transverse second-order moments of the input beam

[1] or alternatively a multi-screen or quadrupole scan measurement

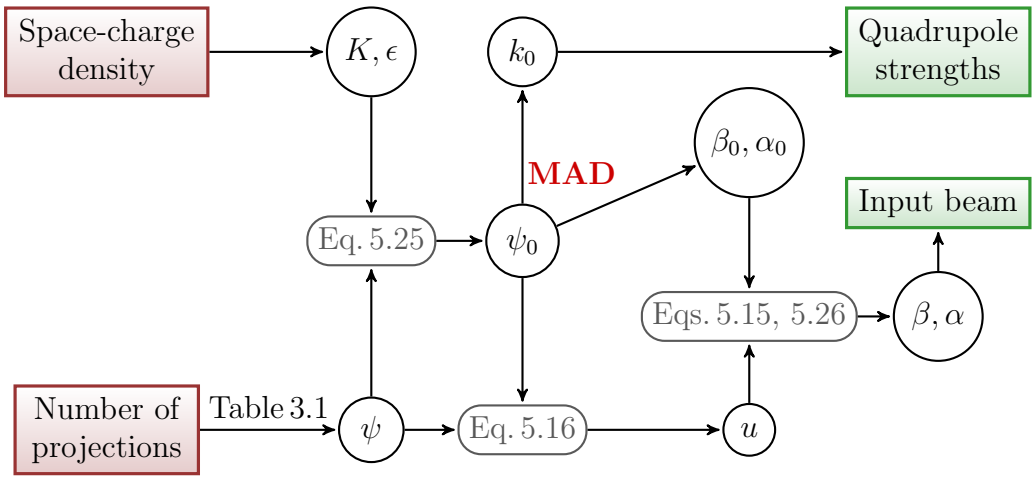

Figure 5.1: Schematic representation of the space-charge matching procedure for the PST section. Given the space-charge density and the number of projection screens, MAD is able to calculate the required quadrupole strengths and input beam parameters including the effect of space charge.

are calculated by the equivalent space-charge translated C-S parameters and the corresponding emittance values. Out of the V-Code tracking, the phase-advance mismatch $\Delta\phi_n$ is calculated at each projection screen n. In order to compare the results with the matching that neglects space charge, the same procedure is followed with $u = 0$. The results are summarized in Table 5.1 for the $\sim 1\,\text{mm·mrad}$ case and in Table 5.2 for the $\sim 3\,\text{mm·mrad}$ beam case. These results were also verified by tracking with ASTRA instead of V-Code and only tiny deviations were observed.

For both emittance cases, the space-charge compensating matching practically eliminates the phase-advance mismatch, reducing it to a level of less than 5° which is the expected mismatch due to the fringe fields. An improvement of more than 30° is achieved with respect to the zero-current matching for the small emittance case. As expected, the correction is larger for the small emittance case as a result of the stronger self fields.

Table 5.3 summarizes the important parameters for each space-charge density case. As the space-charge density increases, a smaller zero-current β-function and a bigger zero-current α-function is required. According to the simulation results in this section, the u factor and thus the scaling of the zero-current parameters proves to be consistent for both charge densities.

	$\Delta\phi$ **at screen:**		
	#2	**#3**	**#4**
***x* plane**			
Matching without space charge	-3.1°	-16.9°	-34.5°
Matching with space charge	0.9°	0.9°	-1.2°
***y* plane**			
Matching without space charge	-4.7°	-20.2°	-37.8°
Matching with space charge	-1.9°	-4.5°	-3.6°

Table 5.1: Evolution of the phase-advance mismatch along the projection screens for each phase plane when matching without and with the consideration of space charge; case of $\varepsilon_n \approx 1\,\text{mm·mrad}$.

	$\Delta\phi$ **at screen:**		
	#2	**#3**	**#4**
***x* plane**			
Matching without space charge	-1.4°	-7.9°	-15.9°
Matching with space charge	-0.1°	-1.4°	-3.4°
***y* plane**			
Matching without space charge	-2.2°	-9.8°	-17.4°
Matching with space charge	-1.1°	-3.7°	-4.9°

Table 5.2: Evolution of the phase-advance mismatch along the projection screens for each phase plane when matching without and with the consideration of space charge; case of $\varepsilon_n \approx 3\,\text{mm·mrad}$.

This implies that, while the target β-function remains practically unchanged regardless the space-charge conditions (as expected by Eq. 5.12), a slightly bigger α-function is needed as the space-charge density increases.

This method can directly be applied to the three- or five-projection tomographic measurement as well. The smaller the number of projections, the bigger the expected correction of the involved parameters is, due to the stronger self fields created by the smaller beam size requirement (see Table 3.1).

	u	$k_0\,[\mathrm{m}^{-2}]$	$\beta_{0x,y}\,[\mathrm{m}]$	$\beta_{x,y}\,[\mathrm{m}]$	$\alpha_{0x,y}$	$\alpha_{x,y}$
Zero-current beam	0.00	48.8	1.00	1.00	± 1.13	± 1.13
3.321 mm·mrad beam	0.08	52.5	0.93	1.00	± 1.14	± 1.23
1.080 mm·mrad beam	0.21	59.2	0.83	1.02	± 1.17	± 1.44

Table 5.3: Important parameters of the space-charge compensated matching using four projection screens for the studied space-charge densities.

5.3 Experimental procedure for a space-charge PST measurement

Combining all the elements of the analysis carried out in the preceding and the current chapter, it is now possible to define the experimental procedure for a space-charge PST measurement. This procedure incorporates the self fields not only in the beam dynamics which is considered for the tomographic reconstruction, but also in the matching of the PST quadrupoles, for an optimal sampling of the beam. The later is needed in order to eliminate the small systematic error which is introduced by the reconstruction algorithm when the projection data are not equally distributed around the trace space. The steps to be followed are listed below:

1. The PST quadrupoles are initially set to the default strength for a zero-current beam and the projection data are captured.

2. A non-space-charge tomographic reconstruction and a bunch length estimation measurement provide an initial guess of the entering C-S parameters.

3. The reconstruction result is corrected after extracting the space-charge transfer matrices using V-Code with the estimated rms moments.

4. The zero-current parameters of the measured beam, calculated using the smooth-approximation theory, are then given to MAD for the space-charge compensated matching of the PST lattice.

5. The space-charge compensated focusing strengths are applied to the PST quadrupoles and new projection data are captured.

6. The tomographic reconstruction is repeated with the new space-charge transfer matrices.

The functionality of the above steps is optimized when certain beam parameters are delivered by the matching section: a symmetric transverse emittance, as a precondition for the space-charge compensated matching of the PST lattice, and the required entering C-S parameters for the design beam dynamics along it. In order to achieve this, the beam matching along the non-periodic and long lattice of the matching section has to follow a different approach, which is going to be covered in the following chapter.

Chapter 6

Space charge along the matching section

This chapter focuses on the influence of space charge along more general lattice designs, such as the aperiodic and long matching section at PITZ, employing a more complex analysis for the asymmetric beam transport. In the beginning, the correlated growth of the projected emittance is explained theoretically and experimental measurements at PITZ are presented. A known technique to compensate this emittance growth with external fields is introduced, together with a software tool which incorporates this principle on elliptical beams using quadrupole magnets. Following this approach, matching simulations are performed and evaluated for typical beam parameters at PITZ, together with corresponding measurements along the PITZ beamline.

6.1 Correlated growth of the projected emittance

For the space-charge analysis so far, a constant beam emittance along the lattice has been assumed. While this assumption has been evaluated in Chapter 4 to be acceptable along the Phase Space Tomography (PST) section of PITZ, it is not the same for the matching section, where the beam propagates along much longer drift spaces under a less dense and aperiodic focusing. The origin of this phenomenon was firstly described by B. Carlsten [70] and a thorough mathematical description has been derived by L. Serafini and J. Rosenzweig [71] and S. Miginsky [72]. According to this analysis, the electron

bunch can no longer be treated as a whole, but its non-uniformities have to be taken into account. The most prominent one has been found to be the inhomogeneity along the longitudinal beam axis [73]. Therefore, from now on the transverse properties of the particles will be treated as a function of their longitudinal coordinate along the bunch.

As shown for a bunch of initially uniform charge distribution in Eq. 4.5, the transverse self field depends on the position along the bunch (ζ): stronger fields are created towards the center of the bunch and weaker at the tails. The forces from these fields will eventually lead to a longitudinal modulation of the transverse size (Fig. 6.1). The consequent change in the current density will directly affect the space-charge dynamics and thus the overall transverse dynamics along the bunch.

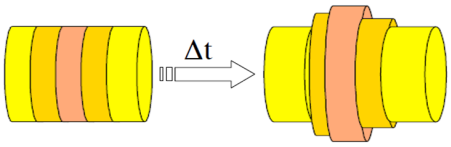

Figure 6.1: Modulation of a beam with uniform longitudinal profile after propagating under the influence of space-charge forces. Image courtesy: M. Ferrario.

When the variation of the beam radius shows small gradients along ζ, the bunch can be divided into longitudinal slices of small, compared to the total bunch size, length ($\delta\zeta$) of constant radius and current. In a longitudinally (quasi-) laminar beam the position of the particles along the bunch is practically frozen and the slices are then considered to be mostly uncorrelated, i.e. they are not mutually interacting. In this case each slice behaves as an independent beam would, with its transverse motion being governed by the beam envelope equation given in Eq. 5.1. Moreover, when transverse quasi-laminarity is also present, each of these slices have a relatively small emittance value, close to the intrinsic component of the beam's emittance. This so-called *slice emittance* is in general different from the *projected emittance*, which represents the overall emittance from all the slices, overlapped in each transverse trace plane.

As already discussed in Chapter 4, the emittance of each slice is expected to remain constant when linear external and space-charge forces act on the beam. On the other hand, despite the initial longitudinal uniformity of a bunch created by a flat-top laser pulse, the eventual longitudinal modulation

caused by the self fields will result in different dynamics along the bunch. Consequently, different slices will propagate under different beam envelope equations, obtaining different C-S parameters and thus different orientation in the trace space, as Eq. 2.13 suggests. In other words, even though all of the slices can be created equal and aligned close to the cathode, their trace-space orientation will not evolve in the same manner along the beamline, leading to a dilution of the beam distribution in the trace space, where the different slices will spread into a fan-like structure, as schematically shown in Fig. 6.2. The result is that even when the emittance of the individual slices remains unchanged, the overall projected emittance in each transverse trace plane, will be seen as significantly increased.

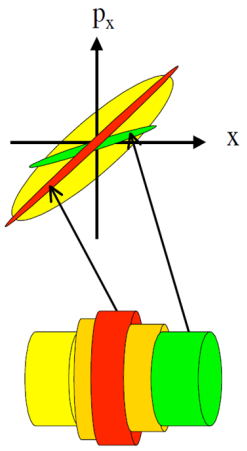

Figure 6.2: Dilution of the longitudinal slices in the trace space. Image courtesy: M. Ferrario.

This phenomenon is described as the *correlated growth of the projected emittance* and originates from the coupling between the longitudinal and the transverse properties of the particles through the linear component of space charge, which has been found to be the prevailing mechanism [70, 73]. While this observation is very common in photo-injectors, it is usually considered only at the low-energy region, i.e. when the electrons leave the cathode and obtain their first acceleration, because of the stronger influence of space charge. Nevertheless, its importance shall not be neglected even at moderate energies, especially when beam matching is required, due to the dependence of the C-S parameters on the evolution of the emittance.

Except from the self fields, the dynamics of each slice is still influenced

by the external fields. As a result, the arrangement of the slices with respect to each other and thus the projected emittance value will be affected by the applied focusing. In order to evaluate this phenomenon at PITZ, the projected emittance has been measured for different transport schemes at different positions along the beamline.

6.2 Experimental observation of the projected emittance growth at PITZ

6.2.1 Measurement guidelines

PITZ is equipped with four transverse emittance measurement stations, three of which are currently operable: the Emittance Measurement SYstem (EMSY) 1 and 2, which are employing the slit-scan technique (see Subsection 3.2.1), and the Phase Space Tomography (PST) module. The location of these stations together with the seven quadrupole magnets comprising the matching section for a 4-projection tomography measurement are shown in Fig. 6.3.

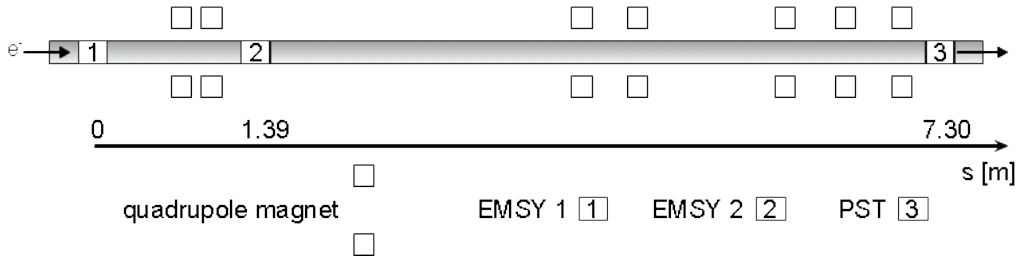

Figure 6.3: Rough schematic layout of the experimental setup. Seven matching quadrupoles are located between the transverse emittance measurement stations, the position of which is indicated on the coordinate axis with respect to the position of EMSY 1.

For the PST measurement, specific entering beam parameters are required (see Table 3.1). Given the number of available focusing elements in the matching section and the number of constraints along it (initial and final beam parameters), the system is usually underdetermined and more than one matching solutions can be obtained. In other words, more than one combinations of quadrupole strengths can deliver the same target parameters in front of the PST lattice for a given beam at EMSY 1. However, different

quadrupole strengths, or k_0 in the beam envelope equation, will lead to a different transport of the slices and thus to a different transverse overlapping and projected emittance value. As a result, a certain beam will show a different evolution of its projected emittance along the beamline, depending on the applied focusing scheme.

In order to observe and quantify this effect, the projected emittance of a beam with 1 nC charge, 21 ps FWHM flat-top temporal length and 22.0 MeV/c momentum was measured at EMSY 2 and PST for different focusing schemes along the matching section. These schemes consisted of four zero-current matching solutions for the design parameters at PST.Scr 2, after the beam was measured at EMSY 1.

6.2.2 Measurement results

Measurement at the EMSY 1 station and matching

The result of the EMSY 1 measurement is presented in Table 6.1. It should be mentioned that the machine parameters and measurement conditions were not optimized due to lack of available operation time. For the interpretation of the upcoming results, it is important to point out the asymmetry of the emittance between the two transverse planes. This asymmetry was present through the whole measurement period at PITZ and is believed to be caused by wake fields and RF field asymmetries in the low-energy region [39, 74].

Table 6.1: EMSY 1 measurement result with statistical errors.

	***x* plane**	***y* plane**
Normalized emittance [mm·mrad]	2.32 ± 0.02	2.07 ± 0.03
β-value [m]	3.31 ± 0.02	3.66 ± 0.10
α-value	0.11 ± 0.07	0.67 ± 0.07

Four matching solutions, referred as m1, m2, m3 and m4, were created for the measured beam using the MAD software without any space-charge compensation. The β-function (β) and the phase advance as plotted by MAD[1] (μ) along the matching section are shown in Fig. 6.4 for each case. The evolution of μ serves as an indication for the strength of the external

[1] neglecting the self fields

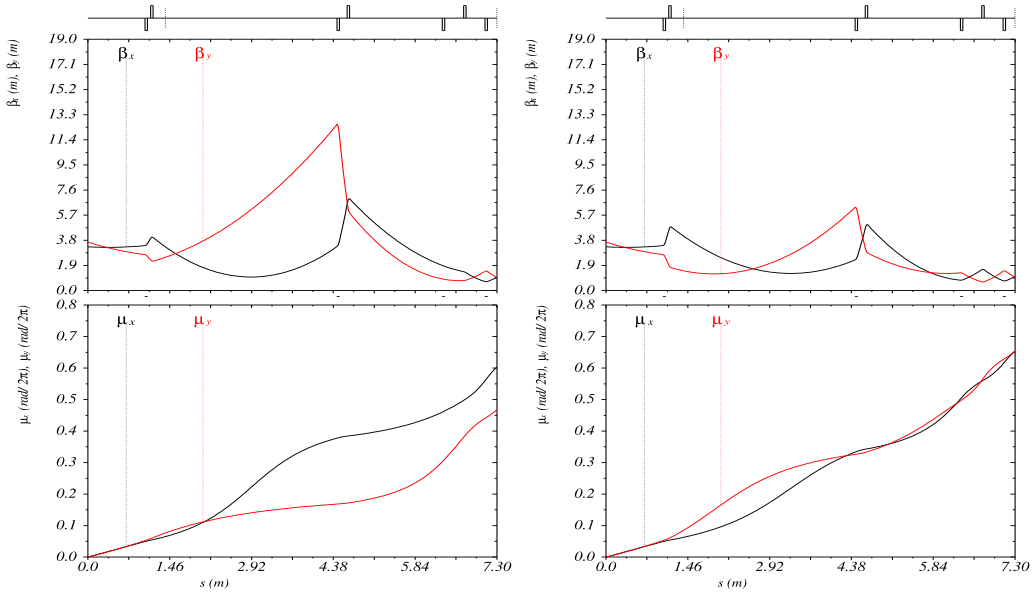

(a) m1 matching scheme.

(b) m2 matching scheme.

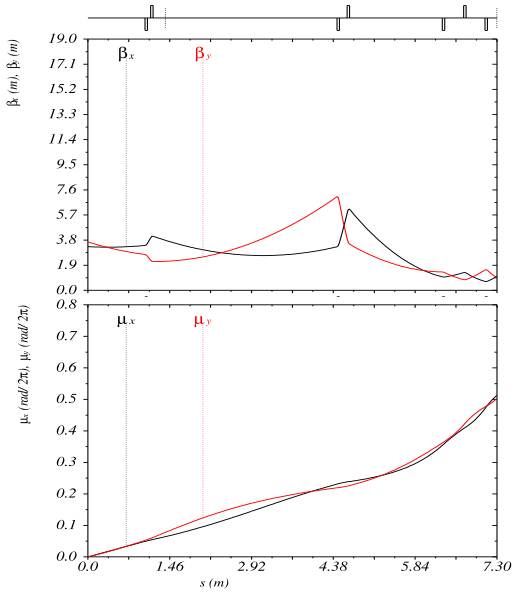

(c) m3 matching scheme.

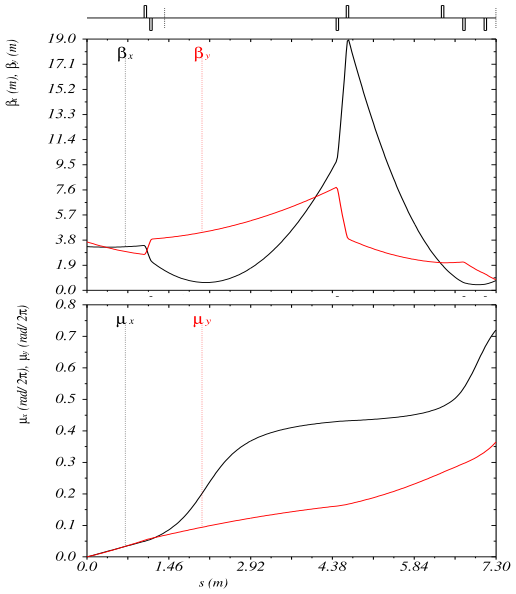

(d) m4 matching scheme.

Figure 6.4: Evolution of the β-function (top) and the phase advance (bottom) from EMSY 1 to PST.Scr 2 for each obtained matching scheme in the absence of space charge. The matching quadrupoles are indicated on top as rectangles and EMSY 2 as a dotted black line right after the second quadrupole.

focusing k_0; the stronger the applied focusing, the faster μ increases. Despite the irregularity of the lattice, the zero-current phase advance and focusing strength are expected to have a rough proportional relationship, corresponding to Eq. 5.13. Therefore, the value of μ at the measurement stations will be used to indicate the integrated applied focusing experienced by the beam up to that location.

Measurements at the EMSY 2 station

Each of the obtained matching schemes was applied to the machine and the transverse emittance was measured at EMSY 2. The gradients of the two quadrupoles upstream the measurement station (High.Q3 and High.Q4) are plotted in Fig. 6.5 and the measurement results are summarized in Fig. 6.6.

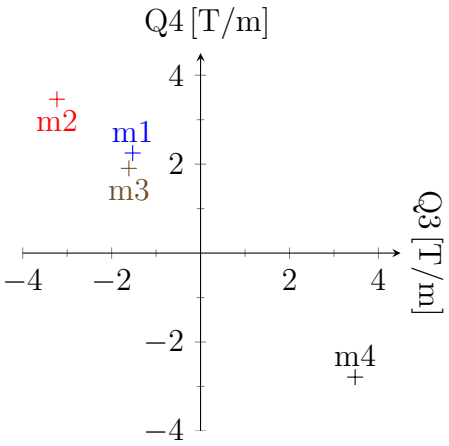

Figure 6.5: Gradients of High.Q3 and High.Q4 for each focusing scheme during the EMSY 2 measurements.

The effect of the different focusing, represented by the MAD-expected phase advance and the measured beam size at this location (Fig. 6.7), is reflected in the emittance value of each transverse plane. By increasing the focusing in one plane, its emittance growth gets reduced and vice versa. Due to the nature of the quadrupole fields, which focus in one plane while defocusing in the other, the result is an emittance exchange between the two transverse planes. For the case of m4, for which a very strong horizontal focusing was achieved, the vertical emittance overtakes the horizontal. The geometrical mean of the emittance of both planes, indicated as ε_{xy}, does

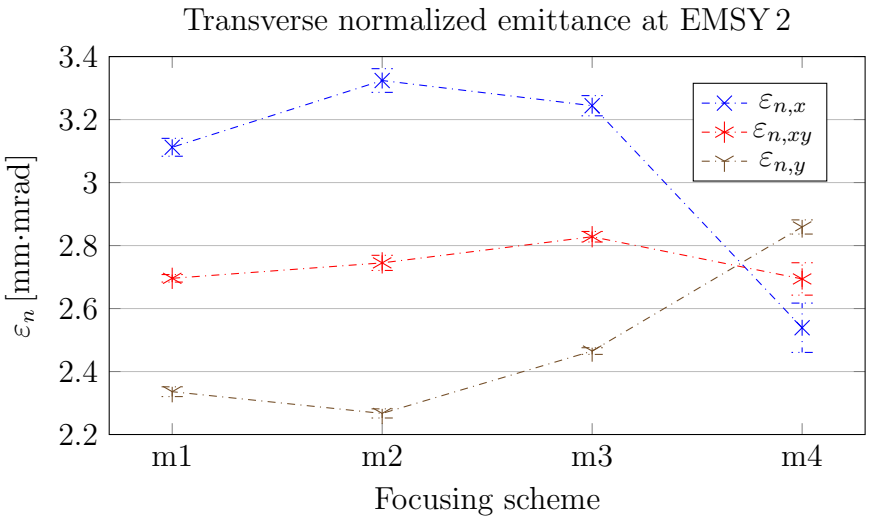

Figure 6.6: Measured emittance at EMSY 2 for each focusing scheme.

not vary significantly among the different matching schemes and shows an increase of $\sim 25\%$ with respect to EMSY 1.

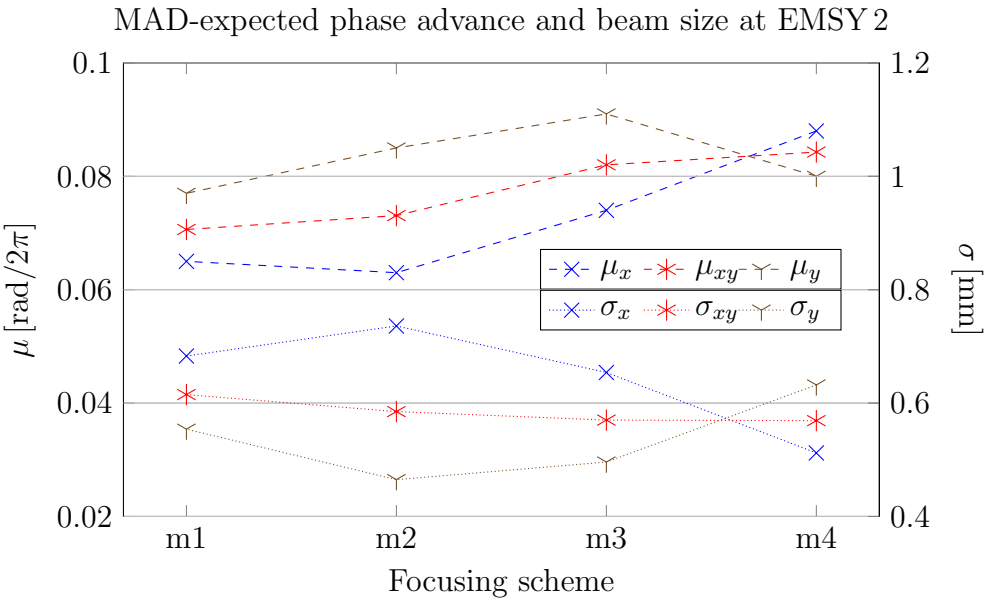

Figure 6.7: MAD-expected phase advance (μ) and measured beam size (σ) at EMSY 2 for each focusing scheme.

Measurements at the PST station

Likewise, the emittance is also measured at PST.Scr 2 after applying each focusing scheme to the matching section. The tomographic reconstruction was done using the space-charge analysis described in Section 4.5, taking into account the measured incoming transverse C-S parameters and bunch length. The results are plotted in Fig. 6.8 together with the results from EMSY 1 and 2.

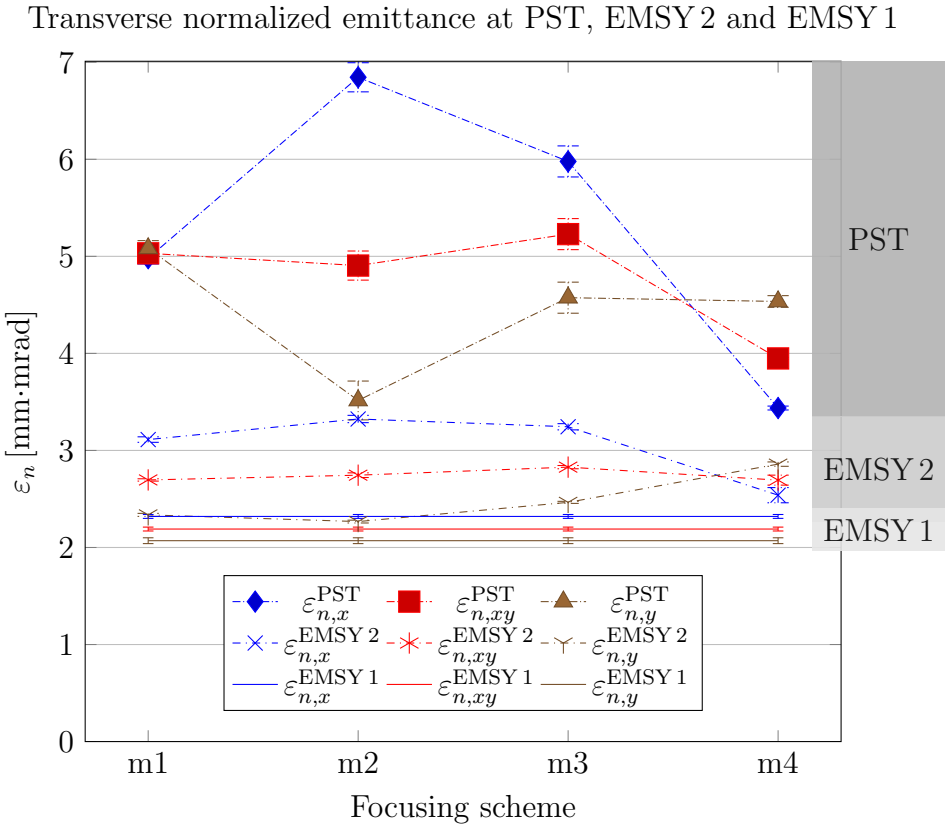

Figure 6.8: Measured emittance at PST.Scr 2, EMSY 2 and EMSY 1 for each focusing scheme.

The observed trend is similar to the one at EMSY 2: the emittance of each transverse plane follows inversely the MAD-expected phase advance of each applied matching scheme, as plotted in Fig. 6.9, taking into account the initial asymmetry between the two planes. The excessive horizontal emit-

tance, already present since the beginning, evolves downstream and has to be corrected by a stronger x-focusing; a symmetric focusing just propagates it further. Like before, m4 manages to reverse the relation between horizontal and vertical emittance, achieving to deliver a smaller average emittance as well.

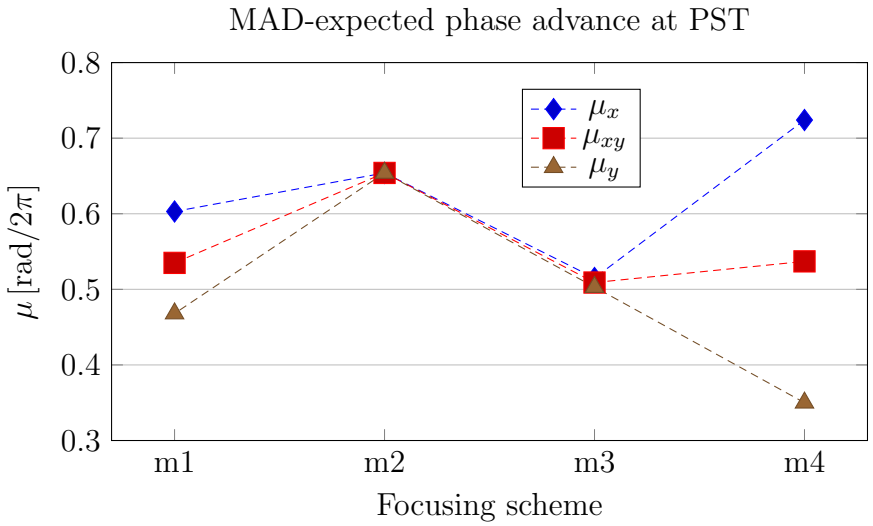

Figure 6.9: MAD-expected phase advance (μ) at PST.Scr 2 for each focusing scheme.

While this study does not intend to focus on the quantitative increase of the emittance, the reason for the $\sim 100\%$ growth observed from EMSY 1 to PST.Scr 2 lies on the machine and measurement conditions, apart from the already described physics mechanism — primarily on the beam halo, which grows as the beam propagates downstream and is better captured by the tomographic measurement than the slit-scan technique, due to the increased signal-to-noise ratio of the first. More information on this topic, as well as a quantitative evaluation of the measured emittance increase with respect to simulation results is going to be presented at the end of this chapter.

In conclusion, these measurements have qualitatively demonstrated the dependence of the transverse projected emittance and its relation between the two phase space planes on the applied focusing strength. A deeper understanding of this correlation can assist the correction of the beam transport and the delivery of a better matching with smaller emittance degradation.

Towards this direction, more details of the slice beam dynamics are going to be described in the following section.

6.3 Emittance compensation

When taking the longitudinal inhomogeneity of the bunch into account, all beam parameters in the envelope equation are dependent on the longitudinal position inside the bunch (ζ). The beam will be modelled in independent longitudinal slices of constant beam parameters and emittance equal to the thermal contribution, which is small compared to the projected emittance (cold beam). A matched-beam solution of effective radius $a(\zeta)$ will correspond to each slice propagating along a non-accelerating lattice of uniform focusing k_0, according to the analysis in Section 5.1. However, due to the temporal modulation induced by the self fields, only a part of the beam can satisfy the matched-beam criteria and all other slices will be mismatched.

Assuming a slightly mismatched effective beam radius (R_0) and zero slope ($R' = 0$) for all the slices, the evolution of the slice effective radius along z is found in [71] to be:

$$R(z,\zeta) = a(\zeta) + [R_0 - a(\zeta)] \cos\left(\sqrt{2}k_0 z\right) . \tag{6.1}$$

The evolution of the correlated projected emittance can then be approximated by [71]:

$$\epsilon(z) \cong \frac{1}{2} k_0 R_0 a(\zeta_I) \frac{\sigma_I}{I} \left|\sin\left(\sqrt{2}k_0 z\right)\right| , \tag{6.2}$$

where ζ_I represents the position of the peak current I inside the bunch and σ_I the rms value of the deviation of the slice currents from the peak value. These two equations indicate a very important property of the bunched beam dynamics in the presence of space charge and external focusing: the radius of the slices oscillate around the matched value with varying amplitudes but equal frequency. This frequency, also referred as the *plasma frequency*, is determined exclusively by the applied focusing force and characterizes the oscillations of the projected emittance as well.

More qualitatively, the above formulas imply that as the different slices propagate along the beamline, they obtain different C-S parameters and phase-space orientation, which nevertheless oscillate with the same frequency. Since all the slices are generated aligned at the cathode, there will be locations downstream where the slices will overlap again in the transverse phase

space, as schematically presented in Fig. 6.10. The correlated emittance growth will then be suppressed and the projected emittance will be minimal at these points, the position of which can be controlled by the applied fields. This procedure, commonly applied in photo-injectors using solenoid fields, is known as *emittance compensation* [70, 71].

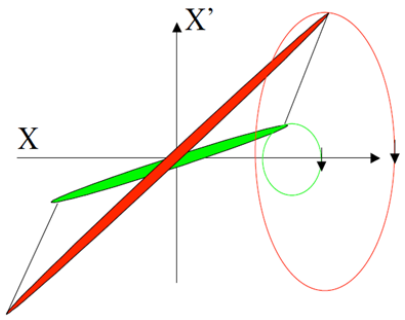

Figure 6.10: Two misaligned longitudinal slices which rotate with the same frequency and are about to overlap on top of the horizontal axis. Image courtesy: M. Ferrario.

As the deviation from the matched solution increases, the linearisation used to derive Eqs. 6.1 and 6.2 becomes less valid and higher order terms should additionally be accounted for. In practice this leads to a differentiation of the oscillation frequency for the different slices, which prevents the projected emittance to drop exactly down to the thermal emittance. Nonetheless, the projected emittance can still be minimized at the oscillation phase of $\sqrt{2}k_0 z = 2\pi n$, where n is an integer, with the optimal result yielded for $n = 1$ [73].

The aforementioned analysis has been extended to discrete (non-uniform) focusing channels and to beams with elliptical symmetry, which is necessary when the focusing elements are quadrupoles [72]. In the latter case, additional modes of oscillations appear [19] and analytical expressions for the emittance compensation are hard or impossible to be derived, therefore simulation packages are required.

6.4 Matching with emittance compensation at PITZ

The emittance fluctuations have been evaluated to be acceptable along the PST section for a correctly matched beam. On the contrary, the emittance has been measured to increase by more than 100% along the matching section. This difference arises from the length as well as the density and transverse symmetricity of the applied focusing of the two lattices. The lattice of the matching section has:

- much longer length compared to the PST lattice, which allows the evolution of the correlated emittance growth to develop in a greater extent,
- sparse focusing elements, which pose limitations in the available integrated focusing and produce big excursions of the beam size and thus a transport far from the controlled case of a matched beam solution,
- an aperiodic structure that together with the matching requirements oppose a (potentially) transversely asymmetric transport which excites different modes of oscillation for each transverse plane and thus asymmetries between them.

The growth of the correlated emittance in the matching section poses difficulties to the delivery of the target C-S parameters in front of the PST lattice, since they are significantly affected by the emittance value. For this reason, the MAD software cannot be used for the beam matching, even with the space-charge compensation method described in Section 5.2, as it assumes a constant beam emittance. The same is true for V-Code which, despite the inclusion of linear self fields, considers the beam ensemble as a single slice and thus cannot predict the correlated emittance growth. It is exactly this problem that is overcome in the SC software, allowing it to perform fast beam matching with linear space charge, as explained below.

6.4.1 The SC software

The *SC* software [75] was developed by A. N. Matveenko and A. V. Bondarenko in order to provide a 2D-emittance compensation scheme for the injector of the Berlin Energy Recovery Linac Project, bERLinPro, at Helmholtz-

Zentrum Berlin. It has also been used for the injector design of the future Femto-Science-Factory [76] in the same institute.

SC resembles in its operation most of the common tracking and matching codes, in the sense that it requires an input beam, a beamline description and a definition of the matching requirements. Its major advantage though is that the input beam is not treated as a whole, as in V-Code for example, but is divided into a user-defined number of longitudinal slices. For each of these slices, the beam envelope equations (Eqs. 5.17 and 5.18) are solved numerically for the two transverse planes. In this way, the resulting projected emittance is calculated from the contribution of each slice and varies accordingly along the simulated lattice. For the input beam, either a distribution file in the format of ASTRA is required or alternatively a description of the second-order rms moments of each slice. The latter option was added for PITZ and allows the software to be used as an on-line matching tool for a measured beam with aligned slices, which is in a good approximation the case for the minimum emittance point measured at EMSY 1.

Once the targets, the weights and the boundaries of the matching process have been defined, an iterative algorithm tries to minimize the user-defined cost function after tracking each intermediate result along the lattice. The form of the cost function has been adjusted to the needs of PITZ and includes the following parameters:

- a target value for the horizontal and vertical (projected) emittance at the end of the lattice $(\varepsilon_x^t, \varepsilon_y^t)$ together with their respective weight (G_ε),
- a target value for the horizontal and vertical α-function at the end of the lattice (α_x^t, α_y^t) together with their respective weight (G_α),
- a target value for the horizontal and vertical β-function at the end of the lattice (β_x^t, β_y^t) together with their respective weight (G_β) and
- a maximum transverse rms size along the lattice $(R_{\max})$ together with its respective weight $(G_{\max})$.

After each tracking iteration, the resulting parameters are subtracted by their respective target values as shown by the following formula:

$$\Big[G_\varepsilon\left(\left(\varepsilon_x-\varepsilon_x^t\right)^2+\left(\varepsilon_y-\varepsilon_y^t\right)^2\right)+G_\alpha\left(\left(\alpha_x-\alpha_x^t\right)^2+\left(\alpha_y-\alpha_y^t\right)^2\right)+ G_\beta\left(\left(\beta_x-\beta_x^t\right)^2+\left(\beta_y-\beta_y^t\right)^2\right)+G_{\max}\left(R_{\max}-\max(X,Y)\right)^2\Big]^{1/2}. \quad (6.3)$$

More optimization options are available in order to vary the accuracy of the result, in the expense of computational complexity.

6.4.2 Simulations for the matching section of PITZ

The performance of SC has been tested in the matching section of the PITZ beamline for the matching requirements of the PST measurement for four and five projection screens, taking into account the maximum focusing gradient (7 T/m) of the quadrupoles. The input beams were generated by ASTRA using a 22 ps flat-top FWHM laser pulse and machine settings which provide 24.7 MeV/c beam momentum and the minimum emittance point at EMSY 1 for beams of 1 nC and 100 pC charge. The target value for the emittance at the end of the lattice was set to be equal to the initial value at EMSY 1, in an attempt to suppress the correlated emittance growth and re-align the longitudinal slices so that the majority of the bunch acquires the aimed C-S parameters. Ten longitudinal slices were considered for the input beam, which was comprised of $5 \cdot 10^5$ macroparticles, and the computational time for the selected optimization settings was in the order of 20 minutes using a standard contemporary computer. Once the matching outcome was obtained, the resulting lattice was tracked by ASTRA using a 3-D space charge grid of 25×25×11 cells, in a time-scale of about 3.5 hours using a powerful computer farm. The results are presented below.

1 nC charge, four projection screens

The minimum emittance point at EMSY 1 for 1 nC bunches was found to be at 0.82 mm·mrad with a β-value of 18.01 m and an α-value of -4.55 for both transverse planes. The matching result in which SC concluded yields the parameters summarized in Table 6.2, together with the respective target values and the values from the ASTRA tracking.

Table 6.2: Matching results for a four-projection PST measurement of a 1 nC beam.

	β_x[m]	β_y[m]	α_x	α_y	$\varepsilon_{n,x}$[mm·mrad]	$\varepsilon_{n,y}$[mm·mrad]
target	1.00	1.00	1.13	-1.13	0.82	0.82
SC	1.07	0.82	1.14	-1.13	1.05	0.95
ASTRA	1.22	1.01	0.96	-0.80	1.03	0.85

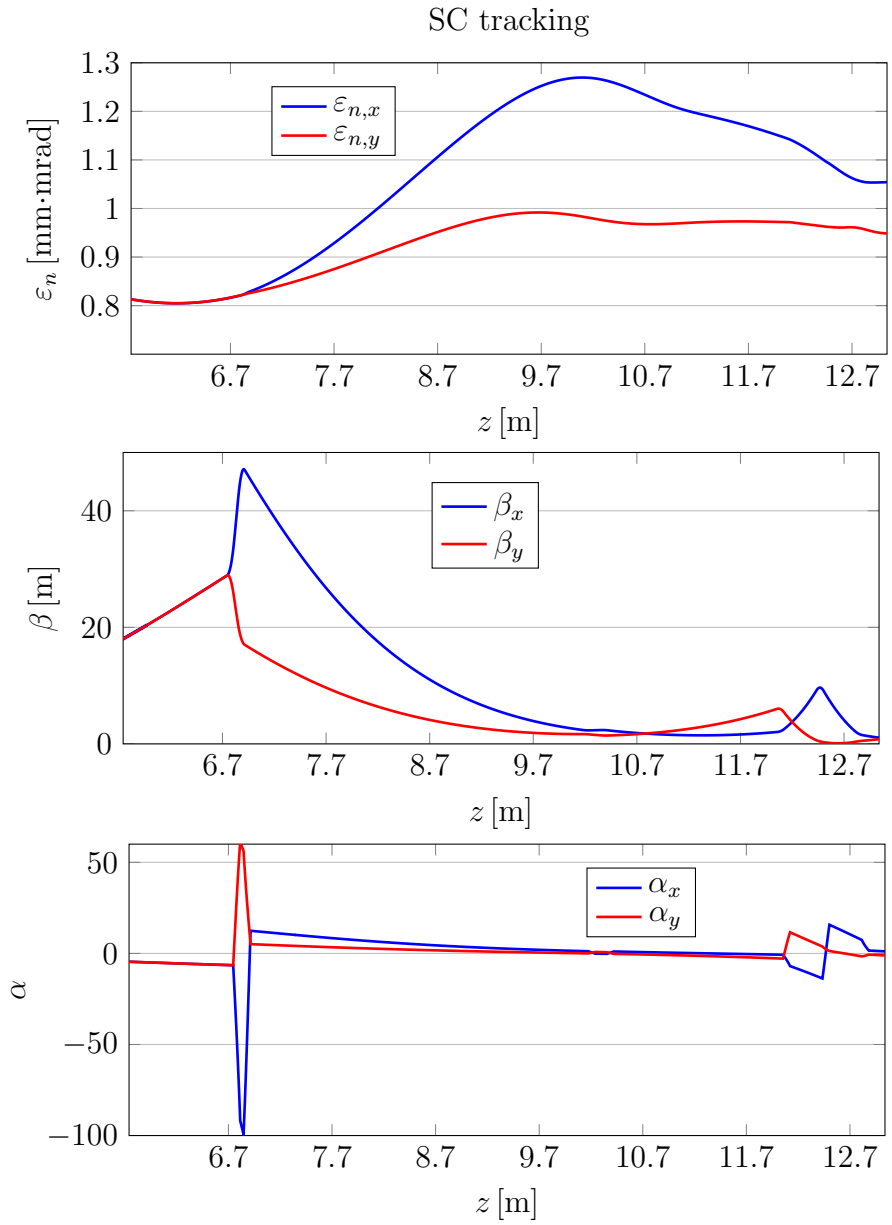

Figure 6.11: Evolution of the normalized emittance (top), β-function (middle) and α-function (bottom) along the matching section of the four-projection PST measurement for the horizontal (blue line) and the vertical plane (red line) according to SC.

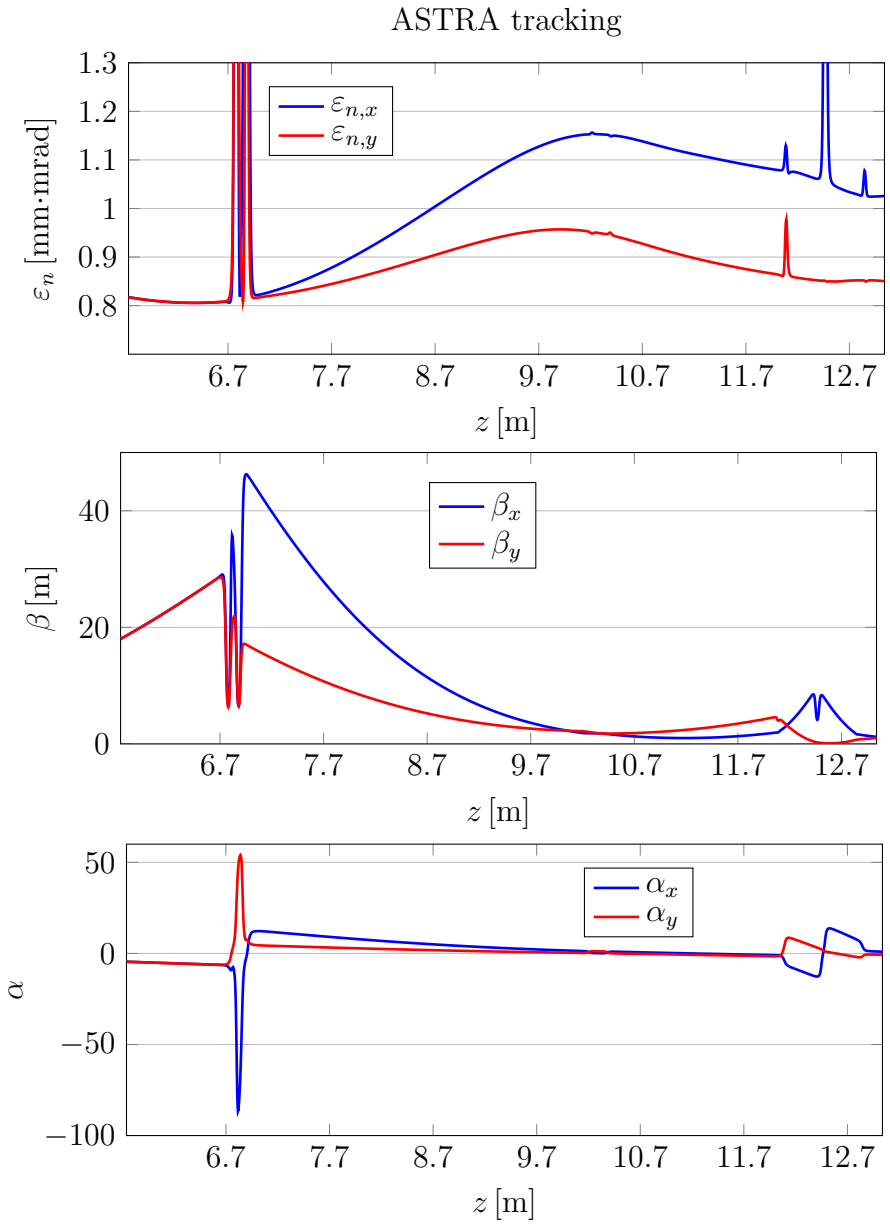

Figure 6.12: Evolution of the normalized emittance (top), β-function (middle) and α-function (bottom) along the matching section of the four-projection PST measurement for the horizontal (blue line) and the vertical plane (red line) according to ASTRA.

For the given optimization settings, SC reached the target C-S values within 18% or better, according to its tracking approach. According to ASTRA, the matching goals are met within 29% or better. The derived mismatches are by an order of magnitude smaller compared with other matching methods that assume a constant emittance, according to past studies. This, relative small, mismatch is going to be taken into account by the new space-charge tomographic reconstruction described in Section 4.5.

The evolution of the C-S parameters and the normalized emittance of both transverse planes along the simulated lattice are presented in Fig. 6.11 for the SC tracking and in Fig. 6.12 for the ASTRA tracking. By comparing the results from the two tracking methods, surprisingly enough the difference is relatively small for the already non-flat-top beam at EMSY 1, 5.7 m downstream the cathode. This observation indicates that the non-linear space-charge forces have a minor effect in the overall beam dynamics. An estimation of the expected emittance growth due to the non-uniformity of the transverse beam profile can be found in [19, 72].

1 nC charge, five projection screens

The same input beam at EMSY 1 was tried to be matched to the conditions of the PST measurement using five projection screens. The results, which are summarized in Table 6.3, show bigger mismatches than previously: up to 25% for SC and up to 41% for the case of ASTRA. These results indicate that, despite the more relaxed matching goals of this setup, the available focusing force from the remaining quadrupoles is not sufficient to provide a better alignment of the longitudinal slices of the bunch. This observation agrees with experimental measurements described in Subsection 4.5.4 and has pointed out the need of extending the PITZ beamline with additional quadrupole magnets, not only for the PST measurements but for other applications as well.

Table 6.3: Matching results for a five-projection PST measurement of a 1 nC beam.

	β_x[m]	β_y[m]	α_x	α_y	$\varepsilon_{n,x}$[mm·mrad]	$\varepsilon_{n,y}$[mm·mrad]
target	1.23	1.23	1.09	-1.09	0.82	0.82
SC	1.54	1.06	1.11	-1.13	1.20	1.04
ASTRA	1.72	0.72	1.12	-0.80	1.10	1.09

100 pC charge, four projection screens

For a beam of 100 pC, the minimum emittance point at EMSY 1 was found to be at 0.25 mm·mrad with a β-value of 9.51 m and an α-value of -7.69 for both transverse planes. The matching solution of SC for a four-projection PST measurement yields the results summarized in Table 6.4. The performance of the matching is similar or even better than for the 1 nC case: SC manages to reach the target C-S values within 6% or better and ASTRA within 26% or better. Despite the lower bunch charge, a much greater improvement was not expected, due to the smaller transverse beam dimensions which are equally important for the space-charge term in the beam envelope equations (Eqs. 5.17 and 5.18).

Table 6.4: Matching results for a four-projection PST measurement of a 100 pC beam.

	β_x[m]	β_y[m]	α_x	α_y	$\varepsilon_{n,x}$[mm·mrad]	$\varepsilon_{n,y}$[mm·mrad]
target	1.00	1.00	1.13	-1.13	0.25	0.25
SC	1.06	1.01	1.11	-1.14	0.26	0.23
ASTRA	1.05	0.82	1.18	-1.42	0.29	0.27

Outcome

The simulations presented above indicate that SC is a time-efficient tool which provides adequate accuracy for the specifications of the matching section at PITZ. Even better results are expected after the upgrade of the matching section at PITZ —the design of which was aided by this study— with four additional quadrupoles. The new setup provides additional focusing strength and shorter drift lengths, allowing smoother matching solutions[2] which are foreseen to satisfy the demanding constraints of the PST measurement using three and five projection screens. As soon as the first two additional quadrupoles were installed, the matching performance of SC was measured and evaluated with ASTRA simulations, with the results being presented below.

[2]with smaller asymmetries, beam size excursions and emittance fluctuations

6.4.3 Measurements along the upgraded matching section of PITZ

During the upgrade phase of the PITZ beamline in 2015 it was possible to apply the studied space-charge matching approach on beam measurements and evaluate its performance at the locations of EMSY 2 and PST.Scr 2. At the time of the measurements, the modifications of the beamline included the repositioning of the booster cavity and the EMSY 1 station upstream by 400 mm and 436 mm respectively and the installation of two additional quadrupole magnets between EMSY 1 and EMSY 2.

Electron bunches of 500 pC charge were generated with laser pulses of 12 ps FWHM long gaussian profile, accelerated to a final momentum of 21.0 MeV/c and focused with the solenoid strength which provides emittance compensation at EMSY 1. Table 6.5 summarizes the measured transverse parameters at that location, as derived from the trace-space plots shown in Fig. 6.15b for the horizontal and Fig. 6.16b for the vertical plane.

Table 6.5: EMSY 1 measurement result with statistical errors.

	***x* plane**	***y* plane**
Normalized emittance [mm·mrad]	0.93 ± 0.04	0.99 ± 0.06
Non-scaled normalized emittance [mm·mrad]	0.81 ± 0.03	0.88 ± 0.02
β-value [m]	6.67 ± 0.35	8.54 ± 0.95
α-value	-0.90 ± 0.15	-0.60 ± 0.39

The measured beam moments were used to create an equivalent ASTRA distribution of $5 \cdot 10^5$ macroparticles with gaussian profile, plotted in Fig. 6.15a in the horizontal trace space and in Fig. 6.16a in the vertical one. It is important to point out that the used parameters correspond to the non-scaled emittance in order to avoid the artificial shearing of the beam in the trace space, as mentioned in Subsection 3.2.1 and explained in Appendix A. For the longitudinal moments, a longitudinal tomographic measurement [5] was performed and the resulting distribution was given as input to SC for the matching of the beam to the requirements of the four-projection PST measurement (Table 3.1). The matched transport according to SC, with a consideration of 10 longitudinal beam slices and optimization parameters

for a relatively quick matching result ($< 20\,\text{min}$), is plotted in Fig. 6.13. The simulation was repeated in ASTRA using a 3-D space-charge grid of $25\times25\times29$, yielding the transport plotted in Fig. 6.14 after $\sim 3.5\,\text{h}$.

The comparison of the tracking results from SC and ASTRA shows only small differences, confirming the efficiency of SC which was demonstrated again earlier in this chapter. In addition to the simulation results, this study offers measurement data from EMSY 2 and PST.Scr 2. The simulated and measured transverse beam parameters at these locations are summarized in Table 6.6. As already justified, the slit-scan measurement result refers to the non-scaled values, neglecting thus the low-intensity halo particles. In order to have a fair comparison with the high signal-to-noise ratio of the PST measurement, which on the contrary enhances the contribution of the halo particles due to the small number or tomographic projections and the strong focusing involved, an intensity cut should be applied to the reconstructed distribution. Empirical and simulation data have shown that a 10% cut provides a reasonable reduction of the beam tails while maintaining the beam core in the same time [10, 35].

	EMSY 2			**PST.Scr 2**		
	SC	ASTRA	Measured	SC	ASTRA	Measured
β_x [m]	2.08	1.99	2.83 ± 0.11	0.91	1.01	0.78 ± 0.02
α_x	1.09	1.16	1.42 ± 0.10	1.13	0.96	0.70 ± 0.02
$\varepsilon_{n,x}$ [μm·rad]	0.86	0.85	0.94 ± 0.04	0.83	0.85	1.96 ± 0.03
β_y [m]	4.83	4.80	5.51 ± 0.37	1.03	1.10	1.07 ± 0.01
α_y	2.29	2.39	3.13 ± 0.14	-1.12	-1.15	-1.09 ± 0.02
$\varepsilon_{n,y}$ [μm·rad]	0.92	0.91	1.25 ± 0.07	0.89	0.90	1.44 ± 0.02

Table 6.6: Transverse beam parameters at EMSY 2 and PST.Scr 2 according to SC, ASTRA and the measurement results including the statistical errors.

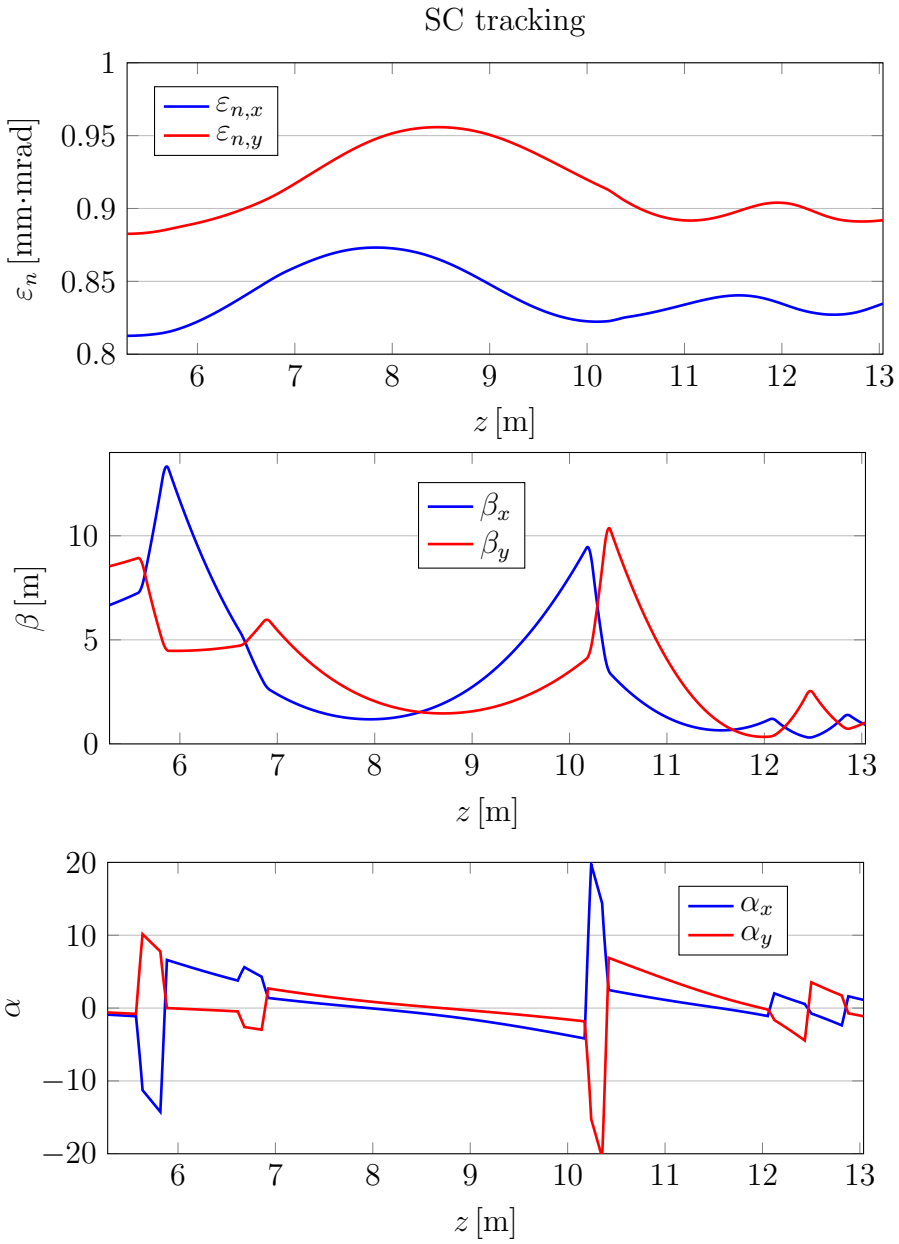

Figure 6.13: Evolution of the normalized emittance (top), β-function (middle) and α-function (bottom) along the upgraded matching section of the four-projection PST measurement for the horizontal (blue line) and the vertical plane (red line) according to SC.

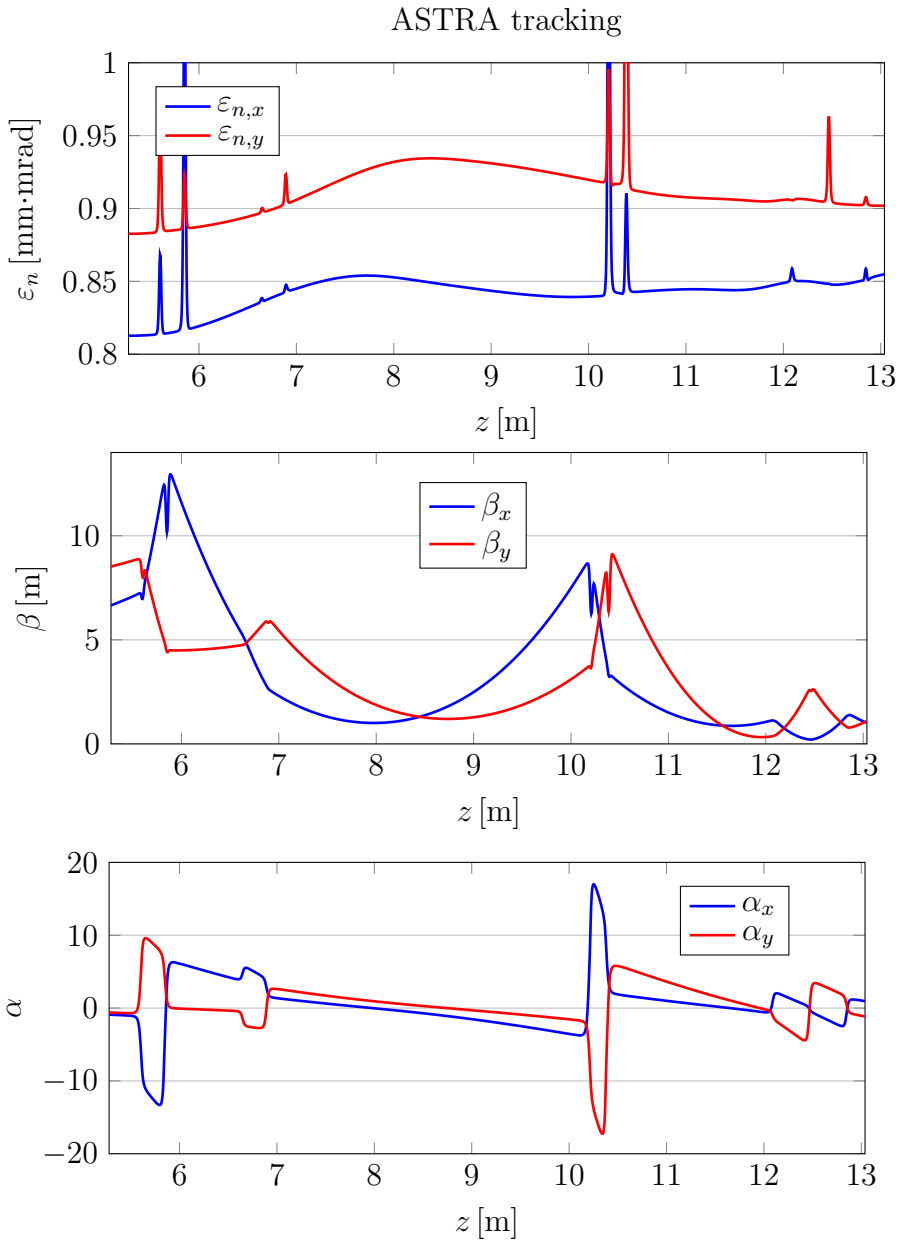

Figure 6.14: Evolution of the normalized emittance (top), β-function (middle) and α-function (bottom) along the upgraded matching section of the four-projection PST measurement for the horizontal (blue line) and the vertical plane (red line) according to ASTRA.

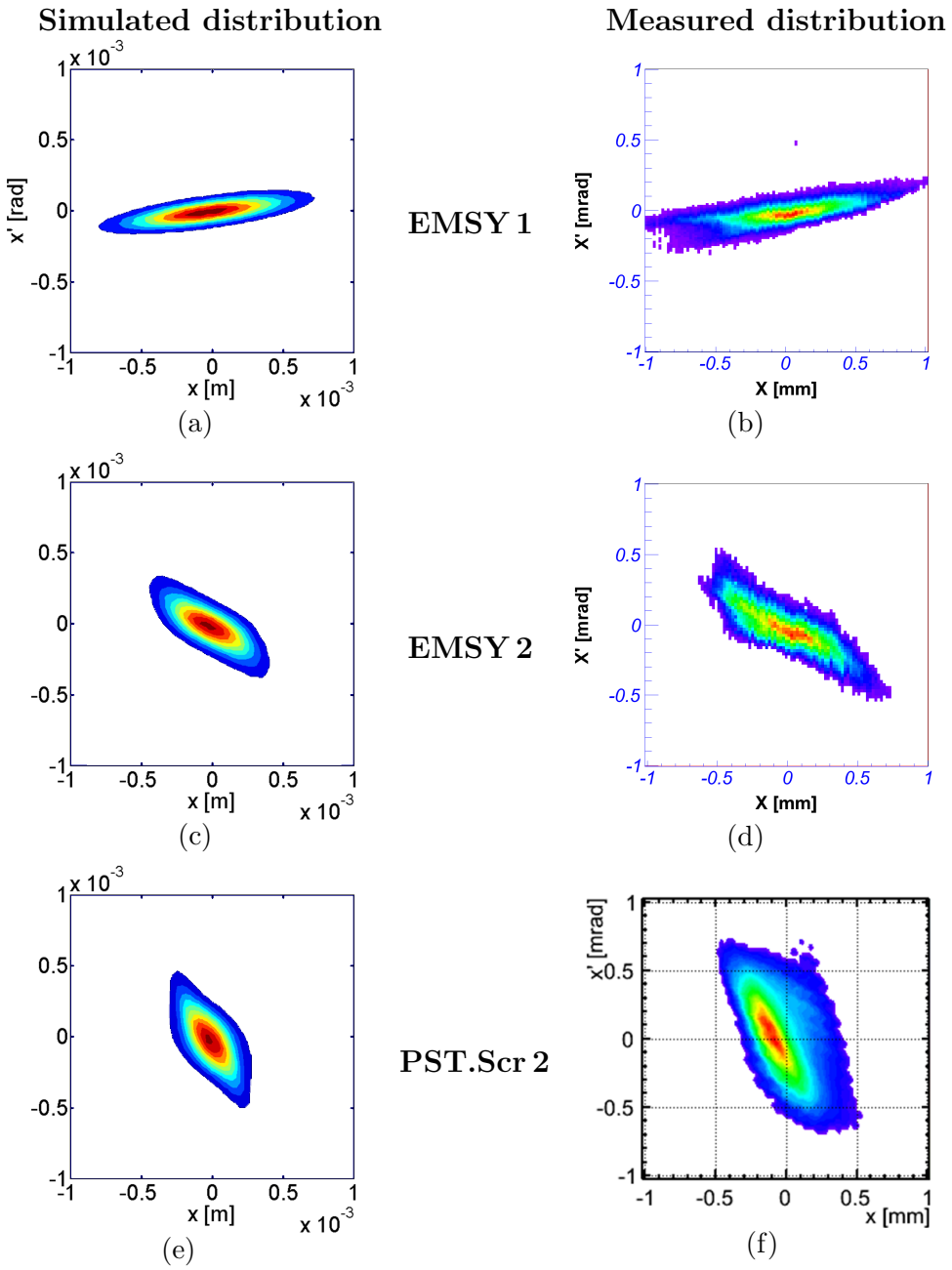

Figure 6.15: Horizontal trace space at EMSY 1 (top row), EMSY 2 (center row) and PST.Scr 2 (bottom row) according to the ASTRA simulation (left column) and the measurement (right column). The colour code represents normalized charge density for each plot (maximum is red, minimum is violet).

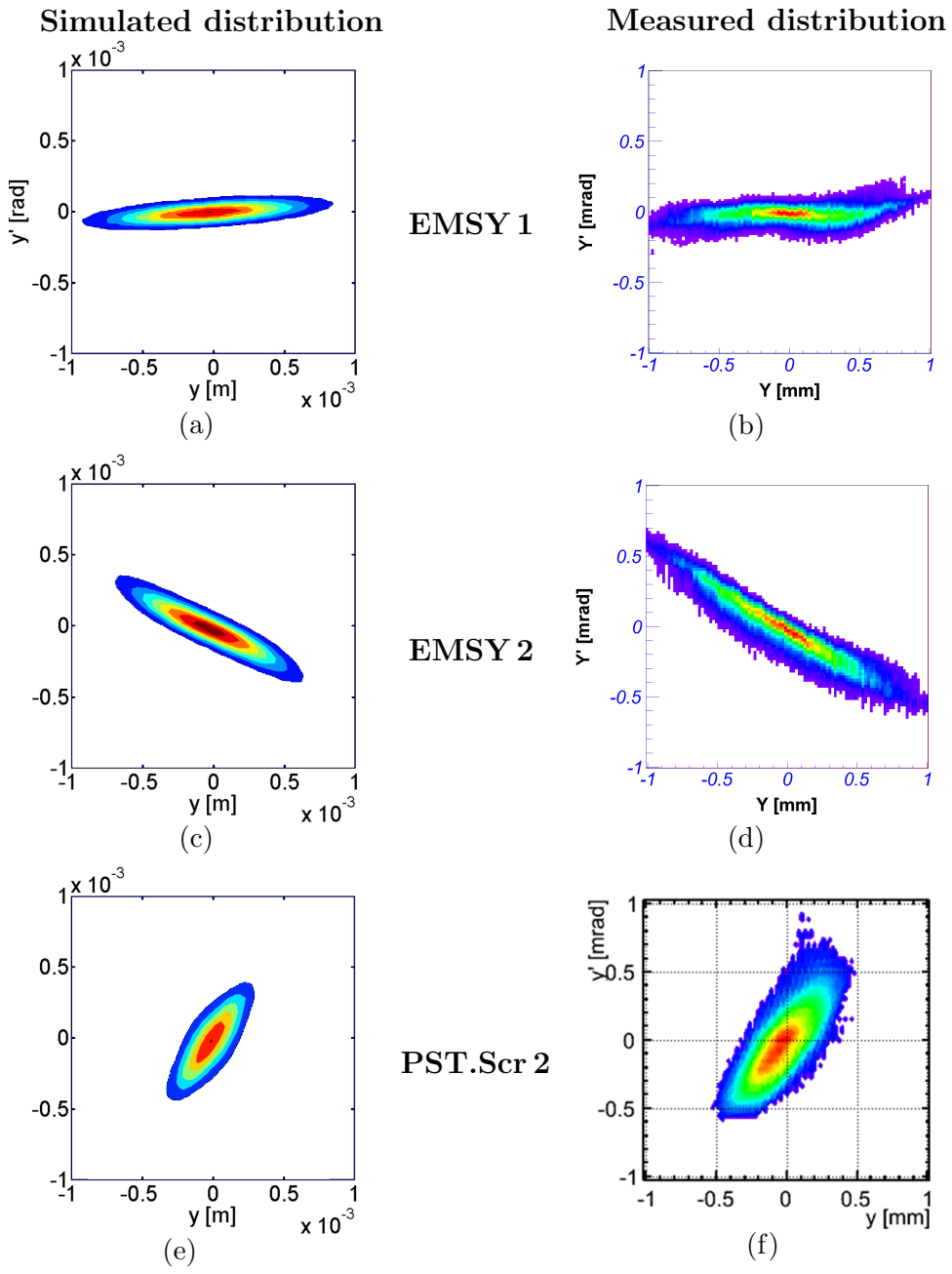

Figure 6.16: Vertical trace space at EMSY 1 (top row), EMSY 2 (center row) and PST.Scr 2 (bottom row) according to the ASTRA simulation (left column) and the measurement (right column). The colour code represents normalized charge density for each plot (maximum is red, minimum is violet).

The evolution of the horizontal trace space according to the ASTRA simulation and the measurement results is shown in Fig. 6.15 at the beginning of matching (EMSY 1), the first measurement station (EMSY 2, 1.848 m and four quadrupole magnets downstream EMSY 1) and the second one (PST.Scr 2, 7.761 m and nine quadrupole magnets downstream EMSY 1). The corresponding plots for the vertical plane are shown in Fig. 6.16. The PST measurement includes the space-charge treatment developed in the previous chapters and has undergone a 10% intensity cut, as explained in the previous paragraph.

A fairly good accordance is observed between the simulated and the measured Twiss parameters at both locations and transverse planes. The delivered mismatches are considered well acceptable and by far better than in the case of no space-charge consideration, when they climb up to several hundreds per cent. This result becomes even more important when taking into account the relatively short time of the matching optimization and the machine imperfections during the measurement (instability of the cooling system, apparent inhomogeneity of the transverse laser profile, not optimized beam trajectory).

When focusing on the value of the normalized emittance, the agreement between simulation and measurement is not as good as for the other two parameters, especially at PST.Scr 2. A reason for the increased measured emittance lies on the generated beam distribution which is used as input for the matching: the irregularities observed in the measured trace space are not represented in the perfect gaussian distribution of the simulation, suppressing potential effects such as transverse coupling, non-linear fields, etc., which can contribute to an emittance growth. For the case of PST.Scr 2, the most probable reason for the big measured emittance is the halo particles, which are not included in the simulated distribution. As indicated by the increasing scaling factor (see Subsection 3.2.1) of the two slit-scan measurements —from 1.1 at EMSY 1 to 1.3 at EMSY 2— the beam halo grows downstream and gets better captured by the sensitive PST measurement.

The overall conclusion is that the studied matching approach is proven to combine time efficiency and reliable performance in conditions of intense space-charge fields. Besides photo-injectors, it can be useful for other machines and applications which require beam matching and 2-D emittance compensation under high intensities and condensed beam dimensions, such as the compressor regions and the undulator entrance of FELs.

Chapter 7

Summary and outlook

The aim of this thesis is to address the effect of space charge in the transverse beam matching and phase space tomography (PST). The main achievements are summarized in the methods which were employed to include the major part of the space-charge dynamics in:

1. the tomographic reconstruction of the transverse phase space
2. the matching of the beam along periodic and dense lattices, as the one used for the data acquisition of the PST measurement
3. the matching of the beam along aperiodic and long lattices, as the one used to deliver the necessary entering parameters for the PST measurement.

Regarding the first point, it was shown that the neglect of space charge when obtaining the beam projections and calculating their phase-space transformations introduces an error of 20% in the reconstructed emittance (among other phase-space quantities) for the nominal beam parameters at PITZ. The exact value of this error depends on the transverse size, energy and peak current of the particle bunch. In order to correct the calculation of the phase space transformations, the inclusion of just the linear part of the beam's self fields was proven to be sufficient. This approach was implemented using the V-Code software, providing a solution quick enough for on-line application during measurements. Except from the space-charge forces, the developed method takes into account the fringe fields of the magnets and the (potentially mismatched) entering C-S parameters of the beam, reducing the

reconstruction error down to 3%. The application of this method requires an initial approximation of the entering C-S parameters, which can either be derived from a tomographic measurement without space-charge consideration, or else rely on the applied matching upstream. What the method is incapable of accounting for, is the variation of the emittance along the PST lattice, an effect which can be diminished by an effective matching upstream. Except from PITZ, this method was successfully applied to measurements from the ALICE facility and could also be applied to the diagnostics of the high-energy compressed beams at FLASH and the European XFEL.

The second point refers to the optimization of the data acquisition, rather than the correct implementation of the reconstruction procedure, in the presence of significant self fields. In order to eliminate the small systematic error which arises when the beam projections are not homogeneously distributed around the trace space, a space-charge matching procedure is required along the PST lattice so that equal phase-advance values are delivered between the projection screens. The structure of the lattice and the foreseen beam parameters along it allow the application of the smooth-approximation theory, which enables matching codes with no space-charge consideration, like MAD, to compensate the defocusing effect of the self fields with an appropriate scaling of the used parameters. This very fast approach has been found to reduce the error in the delivered phase advance from 30° to the negligible value of 5° for beams which have been correctly matched at the entrance of the lattice.

The third point, refers exactly to this issue of delivering certain transverse parameters to a location 13 m downstream the cathode or 7 m downstream the last acceleration stage under strong space-charge influence. The irregularity of this part of the lattice at PITZ makes the previous approach ineffective due to the correlated fluctuations of the emittance along it, which were measured to be strong. For this reason, fast space-charge codes like V-Code, which are unable to simulate the emittance oscillations, cannot be used for this application. On the other side, precise tracking codes like ASTRA are too slow to provide results during machine operation. The solution comes from the SC software, developed at HZB, which combines the simulation of the linear self fields with the consideration of a longitudinally sliced bunch, managing to provide a quick and reasonable estimation of the emittance evolution. Simulations showed that it is able to produce acceptable matching results within 20 minutes, reducing the mismatch at the entrance of the PST lattice below 30%, in contrast to the incomparably worse performance

of the constant-emittance approaches. Tests with experimental data were also conducted for the first time, yielding very encouraging results. Similar performance is expected also in other machines and applications which require fast matching solutions and emittance minimization under significant self fields — two major issues for the operation of FELs.

Besides the main points mentioned above, other tasks that have been carried out include the commissioning of the tomographic measurement using five projection screens and double camera resolution, which allowed the first measurements of 20 pC beams and 1 nC measurements with reduced statistical errors. Moreover, the fast method for estimating the bunch length, proposed by D. Malyutin [47], has also been applied for the first time and its results were used for the space-charge calculations during the measurements. Finally, the investigations on the space-charge effect along different lattices have provided an input for the modification of the PITZ beamline in order to facilitate the plasma wakefield acceleration (PWA) experiment and a potential infra-red/Terahertz radiation source.

The available operation time was not sufficient for further measurements of the space-charge matching procedures with different beam and machine parameters. This task should be performed after the recent beamline upgrade, together with ASTRA simulations which include halo particles, for a deeper understanding of the measurement results. Moreover, it would be useful to extend the simulations and measurements for the cases of three and five PST projection screens, in order to conclude on the optimum number. Even though a bigger number of projections requires more relaxed entering beam parameters (which are easier to match and yield weaker self fields) and improves the image reconstruction, it nevertheless increases the length of the tomography lattice and the effect of the emittance fluctuations along it. An idea worth investigating is the use of more projection screens for beams of smaller charges, which have smaller beam size and require thus increased reconstruction resolution, and less projection screens for beams of bigger charges, which undergo intense emittance oscillations.

Additionally, the method of including the effect of space charge in the calculation of the transfer matrices could also be applied to quadrupole-scan and multi-screen measurements at PITZ and FLASH. In this case, the magnitude of the induced emittance fluctuations would have to be evaluated and taken into account, if necessary. Further simulations and measurements worth performing are with beams of gaussian instead of flat-top longitudinal profile. Moreover, measurements with the anticipated fast kicker magnets

would prove the functionality of the PST module as a quasi non-destructive, permanent monitoring tool for the transverse phase space.

What has been excluded from the analysis in this thesis is the coupling among the transverse planes, which should be minor for optimized operating conditions at PITZ. A future goal would be to extend the PST measurement to the full 4-D transverse phase space, without the assumption of zero transverse coupling, as currently investigated at the Daresbury Laboratory [77].

Appendix A

Scaling factor and C-S parameters at EMSY

The scaling factor S_q, which is used to scale the emittance measured at the EMSY stations at PITZ, is defined for each transverse plane $q = \{x, y\}$ as:

$$S_q = \frac{\sigma_{q,slits}}{\sqrt{\langle q^2 \rangle}} \,,$$

where $\sigma_{q,slits}$ is the rms beam size measured at the location of the slits and $\sqrt{\langle q^2 \rangle}$ the rms beam size from the slit-scan measurement. The scaled emittance ε_S is then defined as:

$$\varepsilon_{qS} = S_q \varepsilon_q = S_q \sqrt{\langle q^2 \rangle \langle q'^2 \rangle - \langle q q' \rangle^2} \,. \tag{A.1}$$

In order to calculate the C-S parameters of the measured trace-space plot at an EMSY station, Eqs. 2.33, 2.31 and 2.32 should be used. The beam size and emittance terms in these equations should be the measured values from the slit scan without any applied scaling. When using the scaled emittance with the beam size as measured at the location of the slits then Eq. A.1 will be interpreted as:

$$\varepsilon_{qS} = \sqrt{S_q^2 \langle q^2 \rangle \langle q'^2 \rangle - S_q^2 \langle q q' \rangle^2} = \sqrt{\langle (S_q q)^2 \rangle \langle q'^2 \rangle - \langle S_q q q' \rangle^2} \,,$$

which introduces an artificial shearing in the trace space as shown in Fig. A.1a, spoiling thus the calculation of the C-S parameters. This is due to the fact that only the beam size is scaled and not the divergence.

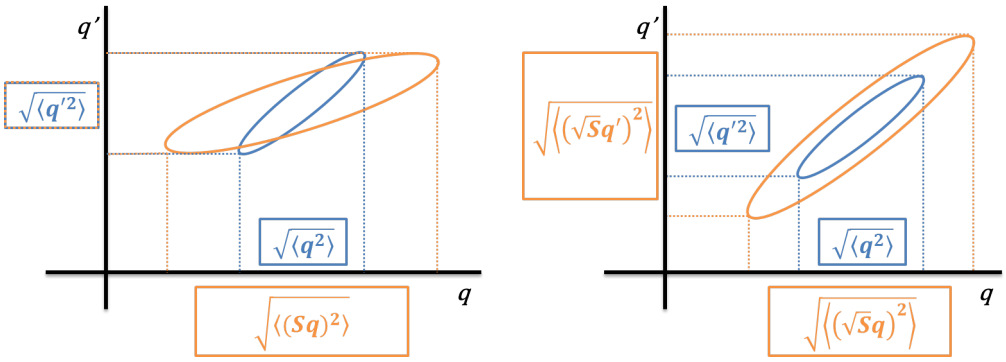

(a) Scaling of the beam size by S_q.

(b) Scaling of the beam size and divergence by $\sqrt{S_q}$.

Figure A.1: Scaled (orange ellipse) and original trace-space plot (blue ellipse) under different considerations of the scaling factor S (q=$\{x, y\}$). A shearing is introduced when the scaling factor is applied only to the beam size and not the divergence (left plot).

Otherwise, if the scaled emittance is used for the calculation of the C-S parameters, then the beam size and the divergence will be scaled as the following formula suggests:

$$\varepsilon_{qS} = S_q\sqrt{\langle q^2\rangle\langle q'^2\rangle - \langle qq'\rangle^2} = \sqrt{S_q\langle q^2\rangle S_q\langle q'^2\rangle - S_q^2\langle qq'\rangle^2} \Leftrightarrow$$

$$\varepsilon_{qS} = \sqrt{\langle\left(\sqrt{S_q}q\right)^2\rangle\langle\left(\sqrt{S_q}q'\right)^2\rangle - \langle\left(\sqrt{S_q}q\right)\left(\sqrt{S_q}q'\right)\rangle^2}$$

Using this consideration, the rms moments are scaled to $\sqrt{S_q}$, the orientation of the trace-space ellipse is preserved, as shown in Fig. A.1b, and the calculation of the C-S parameters is consistent, yielding the same values as without the scaling. It is worth noticing that, in this case, the rms beam size of the trace-space is not scaled to the measured size at the location of the slits ($\sigma_{q,slits}$), which would instead happen with a scaling factor of S_q^2.

Appendix B

Calculations related to the smooth-approximation theory

Eqs. 5.20 – 5.26 in Section 5.1 are derived in this Appendix.

The first set of equations (Eqs. 5.20 – 5.23) are going to be derived only for one transverse plane, for example x, and the results can easily be extended to the other plane in a straightforward way. In order to get to Eq. 5.20, Eq. 5.17 can be written in the following way under the assumption of $X'' = 0$ from the smooth-approximation theory:

$$k_0^2 X - \frac{2K}{X+Y} - \frac{\epsilon_x^2}{X^3} = 0\,.$$

For a matched beam of the form of Eq. 5.19 for both transverse planes, the last formula becomes:

$$k_0^2 a_x - \frac{2K}{a_x + a_y} - k_x^2 a_x = 0 \Leftrightarrow k_x = \sqrt{k_0^2 - \frac{2K}{a_x\,(a_x + a_y)}}\,,$$

which is already Eq. 5.20.

Eqs. 5.6 – 5.14 can be extended in two transverse dimensions, yielding $k_q = \dfrac{1}{\overline{\beta_q}} = \dfrac{\psi_q}{S}$ and $u_q = \dfrac{K}{2k_0\epsilon_q}$, for q=$\{x, y\}$. Using their horizontal compo-

nent together with Eq. 5.10 inside Eq. 5.20, the following equation is derived:

$$\frac{1}{\overline{\beta_x}} = \sqrt{\frac{1}{\overline{\beta_0}^2} - \frac{2u_x k_0 \epsilon_x}{a_x\left(\frac{a_x + a_y}{2}\right)}}\,.$$

Defining $\frac{a_x + a_y}{2} = a$ and substituting $\epsilon_x = \frac{a_x^2}{\beta_x} \Leftrightarrow \frac{\epsilon_x}{a_x} = \frac{a_x}{\overline{\beta_x}}$, the last equation evolves to:

$$\frac{1}{\overline{\beta_x}^2} = \frac{1}{\overline{\beta_0}^2} - \frac{2u_x a_x}{\overline{\beta_x}\overline{\beta_0}a} \Leftrightarrow \overline{\beta_x}^2 = \frac{\overline{\beta_0}^2\overline{\beta_x}a}{\overline{\beta_x}a - \overline{\beta_0}2u_x a_x} \Leftrightarrow \overline{\beta_x}^2 a - \overline{\beta_x}\overline{\beta_0}2u_x a_x - \overline{\beta_0}^2 a = 0\,.$$

This polynomial of β_x has the following positive root:

$$\overline{\beta_x} = \frac{2\overline{\beta_0}u_x a_x + \sqrt{4\overline{\beta_0}^2 u_x^2 a_x^2 + 4a^2\overline{\beta_0}^2}}{2a} = \frac{\overline{\beta_0}u_x a_x + \sqrt{\overline{\beta_0}^2\left(u_x^2 a_x^2 + a^2\right)}}{a} \Leftrightarrow$$

$$\overline{\beta_x} = \overline{\beta_0}\left(\frac{u_x a_x}{a} + \sqrt{\frac{u_x^2 a_x^2}{a^2} + 1}\right)\,,$$

which is equal to Eq. 5.21.

With the help of the x component of Eq. 5.9 and Eq. 5.10, Eq. 5.21 becomes then:

$$\frac{1}{k_x} = \frac{1}{k_0}\left(\frac{u_x a_x}{a} + \sqrt{\frac{u_x^2 a_x^2}{a^2} + 1}\right)\,,$$

which together with Eq. 5.23 for $q = x$ and Eq. 5.13 yield:

$$\psi_x = \psi_0 \frac{\left(\frac{u_x a_x}{a} - \sqrt{\frac{u_x^2 a_x^2}{a^2} + 1}\right)}{\left(\frac{u_x^2 a_x^2}{a^2} - \frac{u_x^2 a_x^2}{a^2} - 1\right)} = \psi_0\left(\sqrt{\frac{u_x^2 a_x^2}{a^2} + 1} - \frac{u_x a_x}{a}\right)\,,$$

which is equal to Eq. 5.22.

In order to get to Eq. 5.24 and 5.25, Eq. 5.16 can be written as:

$$\frac{\psi}{\psi_0} = \sqrt{1+u^2} - u \Leftrightarrow 1 + u^2 = \left(\frac{\psi}{\psi_0} + u\right)^2 = \frac{\psi^2}{\psi_0^2} + 2u\frac{\psi}{\psi_0} + u^2 \Leftrightarrow$$

$$\psi_0^2 = \psi^2 + 2u\psi\psi_0 \,.$$

At that point u can be substituted by its definition given in Eq. 5.14 to get:

$$\psi_0^2 = \psi^2 + 2\frac{K}{2k_0\epsilon}\psi\psi_0 \,,$$

which with the help of Eq. 5.13 becomes:

$$\psi_0^2 = \psi^2 + \frac{KS}{\epsilon}\psi \Leftrightarrow \psi_0 = \sqrt{\psi^2 + \frac{KS}{\epsilon}\psi} \,,$$

which is Eq. 5.25. Finally Eqs. 5.12 and then 5.9 are used to get to Eq. 5.24:

$$\psi_0 = \sqrt{S^2k^2 + \frac{KS^2k}{\epsilon}} = S\sqrt{\frac{1}{\overline{\beta}^2} + \frac{K}{\epsilon\overline{\beta}}} \,.$$

In order to relate α and α_0 when the beam enters the PST lattice, Eqs. 5.5 and 5.7 are calculated for $z = 0$:

$$R(0) = \overline{R}\left[1 + \delta(0)\right] \,,$$
$$R_0(0) = \overline{R_0}\left[1 + \delta_0(0)\right] \,.$$

By deriving both equations with respect to z, the slope of both values becomes:

$$R'(0) = \overline{R}\delta'(0) \,,$$
$$R_0'(0) = \overline{R_0}\delta_0'(0) \,,$$

since $\overline{R}$ and $\overline{R_0}$ are constant, being the matched beam radii. Taking into account that $\delta(z) = \delta_0(z)$ and using Eqs. 2.31, 4.11, 5.6 and 5.8, the ratio of the two equations takes the form:

$$\frac{R'(0)}{R_0'(0)} = \frac{\overline{R}}{\overline{R_0}} \Leftrightarrow \frac{\left(\sqrt{\beta\epsilon}\right)'}{\left(\sqrt{\beta_0\epsilon}\right)'} = \frac{\sqrt{\overline{\beta}\epsilon}}{\sqrt{\overline{\beta_0}\epsilon}} \Leftrightarrow \frac{\frac{1}{2}\left(\sqrt{\beta_0\epsilon}\right)\beta'\epsilon}{\frac{1}{2}\left(\sqrt{\beta\epsilon}\right)\beta_0'\epsilon} = \frac{\sqrt{\overline{\beta}}}{\sqrt{\overline{\beta_0}}} \,,$$

with β and β_0 referring to the entrance of the PST lattice, being thus equal to $\overline{\beta}$ and $\overline{\beta_0}$ respectively. Using Eq. 2.11 and extending it to the zero-current equivalent values, the last equation becomes:

$$\frac{\alpha\sqrt{\overline{\beta_0}}}{\alpha_0\sqrt{\overline{\beta}}} = \sqrt{\frac{\overline{\beta}}{\overline{\beta_0}}} \Leftrightarrow \frac{\alpha}{\alpha_0} = \frac{\overline{\beta}}{\overline{\beta_0}}\,,$$

which, with the help of Eq. 5.15, finally leads to Eq. 5.26.

Bibliography

[1] W. Ackermann *et al.*, "Operation of a free-electron laser from the extreme ultraviolet to the water window," *Nature Photonics*, vol. 1, no. 6, pp. 336–342, 2007.

[2] P. Emma *et al.*, "First lasing and operation of an Ångstrom-wavelength free-electron laser," *Nature Photonics*, vol. 4, no. 9, pp. 641–647, 2010.

[3] R. Abela *et al.*, *XFEL: The European X-Ray Free-Electron Laser - Technical Design Report*. Hamburg: DESY, 2006.

[4] G. Feng, I. Zagorodnov, T. Limberg, H. Jin, Y. Kot, M. Dohlus, and W. Decking, "Beam Dynamics Simulations for European XFEL," TESLA-FEL 2013-04, DESY, Hamburg, Germany, 2013.

[5] D. Malyutin, *Time resolved transverse and longitudinal phase space measurements at the high brightness photo injector PITZ*. PhD thesis, Universität Hamburg, 2014.

[6] M. Gross, R. Brinkmann, J. Good, F. Grüner, M. Khojoyan, A. M. de la Ossa, J. Osterhoff, G. Pathak, C. Schroeder, and F. Stephan, "Preparations for a plasma wakefield acceleration (PWA) experiment at PITZ," *Nuclear Instruments and Methods in Physics Research Section A: Accelerators, Spectrometers, Detectors and Associated Equipment*, vol. 740, no. 0, pp. 74 – 80, 2014.

[7] M. V. Yurkov, E. Schneidmiller, M. Izquierdo, M. Krasilnikov, and F. Stephan, "Integration of Accelerator Based IR/THz Source for Pump Probe Experiments in the Infrastructure of the European XFEL," 35th International Free-Electron Laser Conference, New York, USA, 2013.

[8] E. Saldin, E. Schneidmiller, and V. Yurkov, *The Physics of Free Electron Lasers*. Advanced Texts in Physics, Springer, 2000.

[9] P. Schmüser, M. Dohlus, and J. Rossbach, *Ultraviolet and Soft X-Ray Free-Electron Lasers: Introduction to Physical Principles, Experimental Results, Technological Challenges*. Springer Tracts in Modern Physics, Springer, 1st ed., 2008.

[10] G. Asova, *Tomography of the electron beam transverse phase space at PITZ*. PhD thesis, INRNE, Bulgarian Academy of Sciences, Sofia, 2011.

[11] K. Honkavaara, F. Löhl, D. Nölle, S. Schreiber, E. Sombrowski, M. Sachwitz, M. Castellano, G. di Pirro, L. Catani, and A. Cianchi, "Transverse Electron Beam Diagnostics at the VUV-FEL at DESY," in *Proceedings of the 27th Free Electron Laser International Conference, FEL 2005, Palo Alto, USA, 2005*, pp. 122–125, 2005.

[12] K. Hock, M. Ibison, D. Holder, B. Muratori, A. Wolski, G. Kourkafas, and B. Shepherd, "Beam tomography research at Daresbury Laboratory," *Nuclear Instruments and Methods in Physics Research Section A: Accelerators, Spectrometers, Detectors and Associated Equipment*, vol. 753, no. 0, pp. 38 – 55, 2014.

[13] C. Tennant and Y. Roblin, "First Results of Transverse Phase Space Tomography in the Jefferson Laboratory FEL Upgrade Driver," tech. rep., JLab, 2009.

[14] D. Stratakis, *Tomographic measurement of the phase space distribution of a space-charge-dominated beam*. PhD thesis, University of Maryland, College Park, 2008.

[15] F. Hannon, I. Bazarov, B. Dunham, Y. Li, and X. Liu, "Phase space tomography using the Cornell ERL DC Gun," in *11th biennial European Particle Accelerator Conference, EPAC*, vol. 8, 2008.

[16] R. Baartman and Y. Rao, "Transverse Phase Space Tomography in TRIUMF Injection Beamline," in *Proceedings of IPAC2011, San Sebastian, Spain*, pp. 1144–1146, 2011.

[17] D. Reggiani, M. Seidel, and C. Allen, "Transverse Phase-space Beam Tomography at PSI and SNS Proton Accelerators," in *Proceedings of IPAC2010, Kyoto, Japan*, pp. 1128–1130, 2010.

[18] V. Yakimenko, M. Babzien, I. Ben-Zvi, R. Malone, and X.-J. Wang, "Electron beam phase-space measurement using a high-precision tomography technique," *Phys. Rev. ST Accel. Beams*, vol. 6, p. 122801, Dec 2003.

[19] M. Reiser, *Theory and design of charged particle beams*. Wiley series in beam physics and accelerator technology, Wiley, 1994.

[20] E. Courant and H. Snyder, "Theory of the alternating-gradient synchrotron," *Annals of Physics*, vol. 3, no. 1, pp. 1 – 48, 1958.

[21] S. Humphries, *Principles of Charged Particle Acceleration*. Dover Books on Physics Series, Dover Publications, Incorporated, 2012.

[22] C. K. Allen and N. Pattengale, "Theory and technique of beam envelope simulation," *Los Alamos National Laboratory Internal Report LA-UR-02-4979*, 2002.

[23] M. Ferrario, "Accelerator physics: basic principles on beam focusing and transport," in *International School of Physics 'Enrico Fermi', Course CLXXIX - 'Laser-Plasma Acceleration' - Varenna - 20-25 June 2011*, 2012.

[24] M. G. Minty and F. Zimmermann, "Beam techniques: Beam control and manipulation." USPAS lectures, June, 1999.

[25] A. Chao and M. Tigner, *Handbook of accelerator physics and engineering*. World Scientific, 1999.

[26] M. Reiser, "Periodic Focusing of Intense Beams," *Part.Accel.*, vol. 8, pp. 167–182, 1978.

[27] K. Wille, *The Physics of Particle Accelerators: An Introduction*. Oxford University Press, 2000.

[28] F. Thiel, A. Schnabel, S. Knappe-Grüneberg, D. Stollfuß, and M. Burghoff, "Demagnetization of magnetically shielded rooms," *Review of Scientific Instruments*, vol. 78, no. 3, 2007.

[29] J. Radon, "On the determination of functions from their integral values along certain manifolds," *Medical Imaging, IEEE Transactions on*, vol. 5, pp. 170–176, Dec 1986.

[30] B. Jahne, *Digital Image Processing, 1st ed.* Springer Verlag, New York (ISBN 3-540-53782-1), 1991.

[31] J. J. Scheins, "Tomographic reconstruction of transverse and longitudinal phase space distributions using the maximum entropy algorithm," TESLA 2004-08, DESY, Hamburg, Germany, 2004.

[32] D. W. Townsend and M. Defrise, *Image reconstruction methods in positron tomography.* CERN Geneva, 1993.

[33] F. Natterer, *The Mathematics of Computerized Tomography.* John Wiley, 1986.

[34] G. Minerbo, "MENT: A Maximum Entropy Algorithm for Reconstructing a Source from Projection Data," *Computer Graphics and Image Processing*, vol. 10, no. 1, pp. 48 – 68, 1979.

[35] F. Löhl, "Measurements of the Transverse Emittance at the VUV-FEL," Master's thesis, Department of Physics of the University of Hamburg, 2005. DESY-THESIS 2005-014, TESLA-FEL 2005-03.

[36] C. Mottershead, "Maximum entropy beam diagnostic tomography," *IEEE Trans.Nucl.Sci.*, vol. 32, p. 1970, 1985.

[37] C. McKee, P. O'Shea, and J. Madey, "Phase space tomography of relativistic electron beams," *Nuclear Instruments and Methods in Physics Research Section A: Accelerators, Spectrometers, Detectors and Associated Equipment*, vol. 358, no. 13, pp. 264 – 267, 1995.

[38] M. Hänel, *Experimental investigations on the influence of the photocathode laser pulse parameters on the electron bunch quality in an RF - photoelectron source.* PhD thesis, Universität Hamburg, 2010.

[39] M. Krasilnikov *et al.*, "Experimentally minimized beam emittance from an L-band photoinjector," *Phys. Rev. ST Accel. Beams*, vol. 15, p. 100701, Oct 2012.

[40] I. Will, H. I. Templin, S. Schreiber, and W. Sandner, "Photoinjector drive laser of the FLASH FEL," *Opt. Express*, vol. 19, pp. 23770–23781, Nov 2011.

[41] I. Will and G. Klemz, "Generation of flat-top picosecond pulses by coherent pulse stacking in a multicrystal birefringent filter," *Optics Express*, vol. 16, pp. 14922–14937, Sep 2008.

[42] F. Stephan *et al.*, "Detailed characterization of electron sources yielding first demonstration of European X-ray Free-Electron Laser beam quality," *Phys. Rev. ST Accel. Beams*, vol. 13, p. 020704, Feb 2010.

[43] F. Stephan *et al.*, "New experimental results from PITZ," in *Proceedings of Linear Accelerator Conference LINAC08, Victoria, Canada*, pp. 474–476, 2008.

[44] V. Paramonov, A. Naboka, A. Donat, L. Jachmann, W. Koehler, M. Krasilnikov, J. Meissner, D. Melkumyan, M. Otevrel, B. Petrosyan, J. Schultze, F. Stephan, G. Trowitzsch, R. Wenndorf, K. Floettmann, and D. Richter, "The PITZ CDS booster cavity RF tuning and start of conditioning," in *Proceedings of Linear Accelerator Conference LINAC2010, Tsukuba, Japan*, pp. 241–243, 2010.

[45] R. Spesyvtsev, "Transverse Beam Size Measurement Systems at Photo Injector Test Facility in Zeuthen," Master's thesis, Karazin Kharkiv National University, Ukraine, 2007.

[46] S. Weisse, P. Duval, G. Trowitzsch, and M. Lomperski, "Status of a versatile Video System at PITZ, DESY-2 and EMBL Hamburg," in *Proceedings of ICALEPCS 2007, Knoxville, USA*, 2007.

[47] D. Malyutin, M. Krasilnikov, and F. Stephan, "Longitudinal phase space tomography using a booster cavity at the Photo Injector Test Facility at DESY, Zeuthen site (PITZ)," in *Proceedings of IBIC2014, Monterey, USA*, pp. 442 – 444, 2014.

[48] G. Vashchenko, *Transverse phase space studies with the new CDS booster at PITZ*. PhD thesis, Universität Hamburg, 2013.

[49] L. Staykov, *Characterization of the transverse phase space at the photo-injector test facility in DESY, Zeuthen site*. PhD thesis, Universität Hamburg, 2012.

[50] S. Rimjaem *et al.*, "Optimizations of transverse projected emittance at the photo-injector test facility at DESY, location Zeuthen," *Nuclear Instruments and Methods in Physics Research Section A: Accelerators, Spectrometers, Detectors and Associated Equipment*, vol. 671, no. 0, pp. 62 – 75, 2012.

[51] G. Kourkafas, G. Asova, J. Bähr, S. Khodyachykh, M. Krasilnikov, J. Meissner, A. Oppelt, and F. Stephan, "Tomography module for transverse phase-space measurements at PITZ," DITANET2011, Seville, Spain, 2011.

[52] P. Castro, "Monte Carlo simulations of emittance measurements at TTF2," Technical Note 03-03, DESY, Hamburg, Germany, 2003.

[53] "Methodical Accelerator Design (MAD)." http://mad.web.cern.ch/mad.

[54] J. Rönsch, *Investigations on the electron bunch distribution in the longitudinal phase space at a laser driven RF electron source for the European X-FEL*. PhD thesis, Universität Hamburg, 2009.

[55] Hexagon Metrology, "ROMER Tube Inspection factsheet, 7 AXES ARM, 7530." http://www.hexagonmetrology.com, 2014.

[56] Y. Saveliev, "ALICE: Status, Developments and Scientific Programme," in *Proceedings of IPAC2012, New Orleans, USA*, pp. 613–615, 2012.

[57] M. Ferrario, "Space charge effects," in *CAS lectures*, CERN Accelerator School, Chios, Greece, 2011.

[58] P. Bryant and K. Johnsen, *The Principles of Circular Accelerators and Storage Rings*. Cambridge University Press, 2005.

[59] L. J. Laslett, "On intensity limitations imposed by transverse space-charge effects in circular particle accelerators," *Summer Study on Storage Rings, BNL Report*, vol. 7534, pp. 325–367, 1963.

[60] M. Dohlus, I. Zagorodnov, M. Krasilnikov, E. Gjonaj, and S. Schnepp, "Transverse Effects due to Vacuum Mirror of RF Gun," in *Proceedings of EPAC08, Genoa, Italy*, 2008.

[61] A. Grill, *Cold Plasma Materials Fabrication: From Fundamentals to Applications*. Wiley, 1994.

[62] F. J. Sacherer, "RMS Envelope Equations with Space Charge," *IEEE Transactions on Nuclear Science*, vol. 18, no. 3, pp. 1105–1107, 1971.

[63] "FEL Beam Dynamics Group Home Page." http://www.desy.de/fel-beam.

[64] A. Vlasov, "On the Kinetic Theory of an Assembly of Particles with Collective Interaction," *J. Phys. USSR*, no. 9, 1945.

[65] I. M. Kapchinsky and V. V. Vladimirsky in *Proceedings of the 9th international conference on high energy accelerators*, (CERN, Geneva), pp. 274–288, 1959.

[66] P. Lapostolle, "Possible Emittance Increase through Filamentation Due to Space Charge in Continuous Beams," *IEEE Transactions on Nuclear Science*, vol. 18, no. 3, pp. 1101–1104, 1971.

[67] "A Space charge TRacking Algorithm (ASTRA)." http://www.desy.de/∼mpyflo.

[68] M. Krassilnikov, A. Novokhatski, B. Schillinger, S. Setzer, T. Weiland, and W. Koch, "V-code beam dynamics simulation," ICAP 2000: International Computational Accelerator Physics Conference, Darmstadt, Germany: Online Proceedings, 2000.

[69] S. Franke, W. Ackermann, and T. Weiland, "A Fast and Universal Vlasov Solver for Beam Dynamics Simulations in 3D," in *Proceedings of ICAP09, San Francisco, USA*, pp. 208–211, 2009.

[70] B. Carlsten, "New photoelectric injector design for the Los Alamos National Laboratory XUV FEL accelerator," *Nuclear Instruments and Methods in Physics Research Section A: Accelerators, Spectrometers, Detectors and Associated Equipment*, vol. 285, no. 12, pp. 313 – 319, 1989.

[71] L. Serafini and J. B. Rosenzweig, "Envelope analysis of intense relativistic quasilaminar beams in rf photoinjectors: A theory of emittance compensation," *Phys. Rev. E*, vol. 55, pp. 7565–7590, Jun 1997.

[72] S. Miginsky, "Preprint no. 2007-11." Institute of Nuclear Physics, Siberian Branch, Russian Academy of Sciences, 2007.

[73] S. Miginsky, "Space charge effect, coherence of charge oscillations, and emittance," *Technical Physics*, vol. 53, no. 9, pp. 1197–1208, 2008.

[74] I. Isaev, "RF field asymmetry simulations for the PITZ RF Photo Gun," in *Proceedings of DPG Spring Metting 2015, Wuppertal, Germany*, 2015.

[75] A. V. Bondarenko and A. N. Matveenko, "Implementation of 2D-emittance Compensation Scheme in the BERLinPro Injector," in *Proceedings of FEL2011, Shanghai, China*, pp. 564 – 567, 2011.

[76] A. N. Matveenko, T. Atkinson, A. V. Bondarenko, and Y. Petenev, "Emittance Compensation Scheme for the BERLinPro Injector," in *Proceedings of IPAC2014, Dresden, Germany*, pp. 343 – 345, 2014.

[77] B. Militsyn, D. Scott, S. Barrett, C. Topping, and A. Wolski, "Emittance and Optics Measurements on the Versatile Electron Linear Accelerator at Daresbury Laboratory," in *Proceedings of IPAC2015, Richmond, USA*, 2015.

Acknowledgements

This thesis could have never been written without the scientific, technical and moral support from a big group of different people to whom I wish to express my sincere gratitude.

Starting from Prof. Dr. Jörg Roßbach and Dr. Frank Stephan, I would like to thank them for giving me the opportunity to work for the PITZ facility and perform this study for the University of Hamburg. Moreover, I would like to thank Dr. Winfried Decking and Dr. Torsten Limberg for agreeing to become referees for my dissertation and disputation respectively.

I could never fully acknowledge the help that Dr. Barbara Marchetti has provided to me in every possible way, in good and difficult times. She has been a great supervisor, an exceptional colleague and, above all, a good friend.

Most of the knowledge and skills I acquired during this study was generously offered to me by the members of the PITZ group. Apart from their invaluable contribution during official meetings and private discussions, their experience and persistence during machine operation were indispensable for the experimental results presented in this thesis. I owe special credit to Dr. Grygorii Vashchenko, Dr. Dmitriy Malyutin, Dr. Mikhail Krasilnikov, Dr. Matthias Groß and Prach Boonpornprasert for their unlimited availability to help me at any moment.

Many among the research community choose to cooperate — rather than compete — in seek for scientific progress. I'm grateful to Dr. Kai M. Hock, Prof. Dr. Alexander N. Matveenko and Dr. Alexey Bondarenko not only for their vast aid in providing measurement data, know-how and technical assistance, but mostly for practising an unconditionally open scientific culture and promoting the virtue of sharing.

My educational, professional and everyday reality would not have been as easy and interesting without Christoph Wasicki, Tobias Tydecks and Georgios Thodos; they should also be accredited for this work. Of course I cannot forget all of my dear friends, comrades and band members; I am very lucky to have shared all these experiences with you. A special thanks to Antigoni for her patience, understanding, support and companionship in Berlin and all the places we visited together!

Finally, I wish to thank my family, who has supported me strongly all of these years.